

DTIC FILE COPY

4

MEAN-FLOW MEASUREMENTS IN THE BOUNDARY  
LAYER AND  
WAKE OF A SERIES 60  $C_B = .6$  MODEL SHIP WITH  
AND WITHOUT PROPELLER

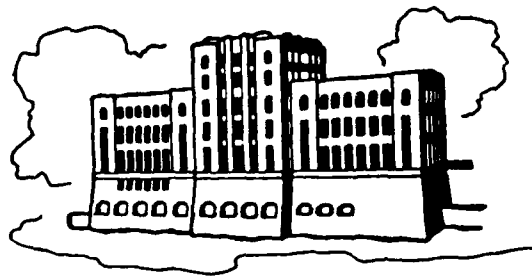
by

Y. Toda, F. Stern, I. Tanaka, and V. C. Patel

Sponsored by

Office of Naval Research  
Accelerated Research Initiative (Special Focus) Program  
in Propulsor-Body Hydrodynamic Interactions  
Contract No. N00014-85-K-0347

AD-A204 046



IIHR Report No. 326

Iowa Institute of Hydraulic Research  
The University of Iowa  
Iowa City, Iowa 52242

November 1988

Approved for Public Release: Distribution Unlimited

DTIC  
ELECTE  
JAN 30 1989  
S H D

89 1 30 038

Block Coefficient  
MEAN-FLOW MEASUREMENTS IN THE BOUNDARY LAYER AND  
WAKE OF A SERIES 60  $C_B = .6$  MODEL SHIP WITH  
AND WITHOUT PROPELLER

by

Y. Toda, F. Stern, I. Tanaka, and V.C. Patel

Sponsored by

Office of Naval Research  
Accelerated Research Initiative (Special Focus) Program  
in Propulsor-Body Hydrodynamic Interactions  
Contract No. N00014-85-K-0347

IIHR Report No. 326

Iowa Institute of Hydraulic Research  
The University of Iowa  
Iowa City, Iowa 52242

November 1988

Approved for Public Release: Distribution Unlimited

# TABLE OF CONTENTS

	<u>Page</u>
ABSTRACT.....	ii
ACKNOWLEDGEMENTS.....	ii
LIST OF SYMBOLS.....	iii
I. INTRODUCTION.....	1
II. EXPERIMENTAL EQUIPMENT AND PROCEDURES.....	4
A. Ship Models and Propeller.....	4
B. Instrumentation.....	5
C. Calibration.....	6
D. Data-Acquisition System.....	7
E. Experimental Procedures.....	9
F. Experimental Uncertainty.....	11
III. RESULTS.....	11
A. Resistance and Propulsion Tests.....	12
B. Wave Profiles.....	14
C. Surface-Pressure Distributions.....	14
D. Mean-Velocity and Pressure Fields.....	15
IV. PROPELLER-HULL INTERACTION.....	19
V. CONCLUDING REMARKS.....	27
REFERENCES.....	29
TABLES.....	32
FIGURES.....	36
APPENDIX I. English Translation of Toda et al. (1987).....	83

For	<input checked="" type="checkbox"/>
	<input type="checkbox"/>
	<input type="checkbox"/>



By		
Distribution/		
Availability Codes		
Dist	Avail and/or	Special
A-1		

## ABSTRACT

Results are presented from a towing-tank experiment of propeller-hull interaction conducted in order to provide detailed documentation of the complete flow field appropriate both for explicating the flow physics and validating computational methods. Mean-velocity and pressure field measurements were made for the with- and without-propeller conditions for the Series 60  $C_B = .6$  hull form at numerous stations both upstream and downstream of the propeller and in the near wake region. Surface-pressure distributions and wave profiles were measured for both conditions. Resistance and self-propulsion tests were also conducted. The experimental equipment and procedures are described, and the results are discussed to point out the essential differences between the flows with and without propeller. The results are analyzed to assess the nature of the interaction between the propeller and the hull boundary layer and wake. To this end, use is made of a propeller-performance program with both nominal and effective inflows. It is shown that most features of the interaction can be explained as a direct consequence of the propeller loading resulting from its operation with a three-dimensional nonuniform inflow.

## ACKNOWLEDGEMENTS

This research was sponsored by the Office of Naval Research, Accelerated Research Initiative (Special Focus) Program in Propulsor-Body Hydrodynamic Interactions, under Contract N00014-85-K-0347. The assistance provided by students of the Osaka University Department of Naval Architecture, especially Mr. T. Takahashi is very much appreciated.

# LIST OF SYMBOLS

## Alphabetical Symbols

$C_B$	block coefficient
$C_m$	midship coefficient
$C_p$	pressure coefficient ( $= 2(p - p_o)/\rho U^2$ )
$C_R$	residuary-resistance coefficient ( $= 2R_R/\rho U^2 S$ )
$C_T$	thrust-loading coefficient ( $= 2T/\rho U^2 \pi(R_p^2 - r_h^2)$ )
	total-resistance coefficient ( $= 2R_o/\rho U^2 S$ )
$C, T, B, P, S$	probe holes
$D_P$	propeller diameter
$e_x, e_r, e_\theta$	unit vectors in the $(x, r, \theta)$ directions
$Fr$	Froude number ( $= U/\sqrt{gL}$ )
$f_x$	axial pressure jump
$\overline{f}_x$	time-averaged angular and radially varying thrust
$f_\theta$	tangential pressure jump
$\overline{f}_\theta$	time-averaged angular and radially varying torque
$g$	gravitational acceleration
$H_C, H_T, H_B, H_P, H_S$	probe-hole pressures
$J$	advance coefficient ( $= U_A/nD_P$ )
$K_Q$	torque coefficient ( $= Q/\rho n^2 D_P^5$ )
$K_Q(\theta_P)$	unsteady blade torque coefficient
$\overline{K}_Q(\theta)$	time-averaged angular varying torque coefficient
$K_T$	thrust coefficient ( $= T/\rho n^2 D_P^4$ )
$K_T(\theta_P)$	unsteady blade thrust coefficient
$K_{Tc}$	unsteady blade thrust due to circulation
$K_{Ta}$	unsteady blade thrust due to added mass
$\overline{K}_T(\theta)$	time-averaged angular varying thrust coefficient
$K, L, M, P$	pitot-probe calibration coefficients
$L$	length between perpendiculars
$n$	propeller revolutions per second
$\mathbf{n}$	normal to blade camber surface
$N$	number of propeller blades
$p$	pressure
$p_o$	uniform-stream pressure

$\Delta p$	pressure jump
$Q$	torque
$Q_o$	torque in open water
$r_h$	hub radius
$R$	resistance, towing force
$R_o$	without-propeller resistance
$R_p$	propeller radius
$R_R$	residuary resistance
$Re$	Reynolds number ( $=UL/\nu$ )
$S$	wetted-surface area
$t$	time
$1-t$	thrust deduction factor
$T$	thrust
$U$	carriage speed, uniform-stream velocity
$U_A$	speed of advance
$U_R$	section velocity
$u, v, w$	velocities in $(x, y, z)$ directions
$V_x, V_r, V_\theta$	velocities in $(x, r, \theta)$ directions
$V_{Px}, V_{Pr}, V_{P\theta}$	propeller-induced velocities in the $(x, r, \theta)$ directions
$V$	calibration velocity vector
$V_h, V_v$	projection of $V$ onto X-Y and Y-Z planes, respectively
$1-w$	effective wake factor
$x, y, z$	global Cartesian coordinates
$x, r, \theta$	cylindrical coordinates for propeller
$X, Y, Z$	local Cartesian coordinates for pitot-probe measurements
$z_o$	shaft center

### Greek Symbols

$\alpha$	section angle of attack
$\beta_n, \beta_v$	angles between $V_h$ and $V_v$ and the X-axis, respectively
$\beta_I$	hydrodynamic-pitch angle
$\Gamma$	spanwise circulation distribution
$\Gamma_{max}$	maximum value of $\Gamma$
$\zeta$	wave elevation

$\eta$	propeller efficiency
$\eta_R$	relative rotative efficiency
$\theta_p$	propeller angular position measured from top dead center ( $\theta = 0$ ), positive clockwise looking upstream
$\theta_h$	angle between $V$ and $V_h$
$\nu$	kinematic viscosity
$\xi$	propeller angular coordinate measured relative to the generator line, positive clockwise looking upstream
$\rho$	density
$\phi$	geometric-pitch angle
$\omega_x$	axial vorticity

### Superscripts

'	local values for pitot-probe measurements
---	---

### Subscripts

LE	value at leading edge
TE	value at trailing edge

## I. INTRODUCTION

Detailed experimental information concerning the interaction between a propeller and the flow over a ship hull is very limited, especially for practical hull forms. The most extensive data available are those concerned with simple propeller-shaft configurations. These include steady (circumferentially-averaged) mean-velocity profiles in the immediate vicinity of the propeller, and in the near and intermediate wake regions, and some limited unsteady (phase-averaged) mean-velocity profiles, and steady and unsteady turbulence profiles (see Stern et al. (1988b) for references). The situation for axisymmetric bodies is similar, although the data are considerably more limited. Hucho (1968) and Huang et al. (1976, 1980) report wind-tunnel measurements, and Nagamatsu et al. (1978) and Toda et al. (1982) describe towing-tank measurements, of steady mean-velocity profiles upstream of the propeller. All these cases, except Huang et al. (1976, 1980), precluded realistic wake measurements because the propeller was driven from downstream. Schetz and associates (1975, 1981, 1983) and Neu et al. (1988) report wind-tunnel measurements of steady mean-velocity and turbulence profiles in the near and intermediate wake, including, in some cases, the effects of appendages and angle of attack. Rood and Anthony (1988) investigate propeller-appendage interaction through detailed steady (i.e., averaged over a sufficient number of propeller revolutions) and unsteady mean-velocity measurements in a plane just upstream of the propeller. Experiments have also been performed for a vertical flat plate with a propeller operating near the trailing edge driven from downstream in which steady mean-velocity profiles were measured upstream of the propeller both in wind tunnels (Hucho, 1968) and in towing tanks (Toda, 1984; Nagamatsu, 1985). The latter reference includes results for T sections. Similar experiments have also been performed for the Wigley parabolic hull at low Froude number by Toda et al. (1984) and Sato et al. (1986).

Although numerous experiments have been performed in towing tanks for various practical hull forms, none is sufficiently detailed to document the entire flow field. All are focused on some particular aspects of the general problem of propeller-hull interaction. The most notable recent experiments have been those performed in Japan in support of the development of ultra-large energy-efficient merchant ships, i.e., low-speed, large-block-



coefficient tankers and ore carriers, and high-speed container ships (see, e.g., Tasaki et al., 1987). Typical studies, citing example references, are as follows. Steady mean-velocity profiles have been measured at one or two stations upstream of the propeller for the with- and without-propeller conditions to study scale effects (Dyne, 1974; Kux and Laudan, 1984), unstable phenomena encountered during self-propulsion tests (Taniguchi and Watarabe, 1969), and the characteristics of effective wakes (Laudan, 1981; Kasahara, 1985, 1986). Similar measurements have been made in the near and intermediate wake to study recovery of the rotational energy (Ishida, 1986) and propeller-rudder interaction (Baba and Ikeda, 1980). Also, steady surface-pressure distributions have been measured to study thrust deduction (Cox and Hansen, 1977; Fujii and Fukuda, 1984). Lastly, only two studies report limited steady turbulence measurements (Chen, 1964; Kux and Laudan, 1984).

It is apparent from the foregoing that experimental studies of propeller-hull interaction are required to provide detailed documentation of the complete flow field appropriate both for explicating the flow physics and for validating computational methods. The present cooperative study between The University of Iowa and Osaka University was undertaken for this purpose. In particular, steady mean-velocity and pressure field measurements were performed for the with- and without-propeller conditions for the Series 60  $C_B = .6$  hull form at numerous stations both upstream of the propeller and in the near wake region. Surface-pressure distributions and wave profiles were measured for both conditions. Also, resistance and self-propulsion tests were conducted. The experiments were performed in the Osaka University towing tank at low Froude number,  $Fr = .16$ , to minimize free-surface effects. The test conditions and results are documented in sufficient detail to be useful as a test case for validating computational methods.

Two 4m long models were constructed for the experiments: a wooden model used for the mean-velocity and pressure field measurements (figure 1a); and a fiber-reinforced plexiglass model with pressure taps used for the surface-pressure measurements (figure 1b). A 145.64mm diameter, 5 bladed propeller with MAU sections was used. The with-propeller measurements were performed for the model self-propulsion condition. The princi-

pal dimensions of the models and propeller are given in Table 1 and the locations for the detailed measurements are summarized in Table 2.

In the presentation of the results and the discussions to follow, a Cartesian coordinate system is adopted in which the x-, y-, and z-axes are in the direction of the uniform flow, port side of the hull, and increasing depth, respectively. The origin is at the intersection of the waterplane and the forward perpendicular of the hull. The mean-velocity components in the directions of the coordinate axes are denoted by  $(u,v,w)$  and the carriage velocity by  $U$ . Unless otherwise indicated, all variables are nondimensionalized using the model length between perpendiculars  $L$ , carriage velocity  $U$ , and fluid density  $\rho$ .

The Series 60  $C_B = .6$  hull form was selected for the experiments as a representative fine hull form and to complement the many previous and ongoing studies with this geometry. The Series 60 geometry was conceived to provide systematic information on the design of lines for single-screw merchant ships ca. 1950. The parent form,  $C_B = .6$ , was designed based on considerations of then successful ship designs. A full account of the original methodical series is provided by Todd (1963). The many experiments with the Series 60 hull form since then are far too numerous to review; however, of particular interest is the fact that it is one of the four hull forms selected for the Cooperative Experimental Program (CEP) of the Resistance and Flow Committee of the International Towing Tank Conference (ITTC, 1987). The experiments under this program are, however, restricted to hulls without propellers.

An outline of this report is as follows. The experimental equipment and procedures are described in Chapter II. In Chapter III, the results are presented and discussed to point out the essential features of the flow for both the with- and without-propeller conditions. Next, in Chapter IV, the results are analyzed to assess the nature of the interaction between the propeller and the hull boundary layer and wake. Lastly, in Chapter V, some concluding remarks are made.

## II. EXPERIMENTAL EQUIPMENT AND PROCEDURES

The experiments were performed in the Osaka University, Department of Naval Architecture, towing tank (figure 2). The towing tank is 100m long, 7.8m wide, and 4.35m deep. The towing carriage is driven by four 15kw DC motors which are controlled by a static Leonard system with analog-digital hybrid control. The carriage can be driven at speeds up to 3.5m/s with an accuracy of  $\pm 1\text{mm/s}$ .

### A. Ship Models and Propeller

The lines of the Series 60  $C_B = .6$  ship models used in the experiments are shown in figure 3. These conform to the standard offsets; however, a small modification was made to the stern geometry ( $.955 \leq x \leq .995$ ) in order to attach the propeller. The broken lines in figure 3 show the original bare hull and the solid lines the modified one. The details of the stern arrangement, including the modification to attach the propeller and the location of the propeller plane, were based on the original methodical series (Todd, 1963). The principal dimensions of the models are given in Table 1 and the offsets are provided in Table 3. Two 4m long models were constructed for the experiments: a wooden model was used for the mean-velocity and pressure field measurements (figure 1a); and a fiber-reinforced-plexiglass model with pressure taps was used for the surface-pressure measurements (figure 1b). In order to induce turbulent flow, a row of trapezoidal studs with 1.5mm height, 1.5mm length, 2mm front width and 1mm back width, were fitted at 10mm spacing on both models at  $x = .05$ .

The lines of the propeller used in the experiments are shown in figure 4a. The principal dimensions are given in Table 1 and the offsets are provided in Table 4. This is a conventional stock propeller designed based on the MAU methodical series (Tsuchida et al., 1958) with 145.64mm diameter, constant pitch, zero skew, 6 degree rake, 5 blades, and MAU  $n = 25$  sections. Although there are some minor differences, here again, the dimensions were selected based on the original methodical series (Todd, 1963).

## B. Instrumentation

Single- and duplex-balance rod-deflection type dynamometers were used for the resistance and propeller open-water tests, respectively. These same dynamometers were also used for the self-propulsion tests.

The surface-pressure distribution was measured with 359 1mm-diameter pressure taps located in the stern region ( $x \geq .8$ ) where the influence of the propeller was expected to be large (figure 5a). The holes were spaced sufficiently close in both the girthwise (for 9 stations) and axial (for 3 waterlines) directions to allow for evaluation of pressure gradients. In order to ascertain the effects of hole interference, the starboard spacing was made somewhat coarser than the port. Two 48-position scanivalves and two differential pressure transducers (Scanivalve PDCR23D with a zero volume adapter) were used. A static-pressure probe was used to measure the ambient pressure (excluding the effects of gravity). It was located at  $x = -.1$ ,  $y = .85$ , and  $z = 0.25$ . This position was selected so that the probe was in undisturbed flow and its wake and wavemaking did not disturb the flow in the measurement region. All of the pressure taps were joined by vinyl tubing to eight male 48-port pneumatic connectors. Since this arrangement allows for the measurement of 376 pressures, some locations (17) were measured twice through the use of a branch to insure repeatability. Consecutively, two of the connectors at a time were joined to female connectors which were connected to the scanivalves. Pressure tubes from the scanivalves were connected to the plus side of the transducers. Tubes from the static-pressure probe (divided at a branch) were connected to the negative side of the transducers. The tubes from the branch were also connected to one channel of each connector to check the zero point of the transducers during the running of the carriage. The scanivalves were driven by solenoid controllers which were controlled by a microcomputer on the carriage. By the control of the scanivalve and the choice of connectors, any one of the pressure taps on the hull could be connected to the transducer. Figure 5b provides a block diagram of the system used for the measurement of the surface-pressure distribution.

Two five-hole pitot probes (modified NPL type), one for the port and one for the starboard side of the hull, were used to measure the direction

and magnitude of the velocity in the hull boundary layer and wake. The starboard-side probe is shown in figure 6. The port-side probe is similar, but a mirror image. Figure 7 is a photograph of the automated traverse used to position the probes. The probes could be moved in three directions of a Cartesian coordinate system. The port and starboard crossplane positioning (y-z planes) was driven by three stepper motors which were controlled by a microcomputer on the carriage. This enabled multiple measurements per carriage run. The axial (x-direction) positioning was achieved by moving the entire traverse along the measurement rails of the carriage. The same static-pressure probe as described above was also used. The leads from the pitot probes were connected by vinyl tubing to one side of ten differential pressure transducers (Kyowa PD100CA). The tube from the static-pressure probe was connected by vinyl tubing to a branch. Ten pressure tubes were divided at the branch and connected to the other side of the transducers. A block diagram of this arrangement is shown in figure 8a.

For each experiment, the voltage output from the transducers was sampled, digitized, recorded, and analyzed by a microcomputer on the carriage. The measurements were monitored with a multi-pen recorder during each carriage run.

### C. Calibration

The differential pressure transducers were calibrated using two water tanks. One was moved up and down by a one-dimensional traverse while the other was at a fixed elevation, i.e., the pressure was measured by water head.

Both five-hole pitot probes were calibrated in the towing tank using the calibration device shown in figure 9. Since the effect of Reynolds number on calibration is known to be insignificant for carriage speeds in excess of .4m/s, the calibration was done at a carriage speed of 1m/s. The data were analysed using a method similar to Fujita (1979) which is described below.

The probe-based Cartesian coordinate system (X,Y,Z) and other basic quantities used for the data analysis are defined in figure 10. Referring to figure 10, the X-axis is in the direction O-C and the Y- and Z-axes are

in the T-C-B and P-C-S planes, respectively. The origin is at the center of curvature of the tip face. The probe holes are designated C, T, B, P, and S and the corresponding sensed pressures are  $H_C$ ,  $H_T$ ,  $H_B$ ,  $H_P$ , and  $H_S$ , respectively. The calibration velocity vector is  $\mathbf{V}$  and its projections in the X-Y and Y-Z planes are  $V_h$  and  $V_v$ , respectively. The angles between  $V_h$  and  $V_v$  and the X-axis are  $\beta_h$  and  $\beta_v$ , respectively. The angle between  $\mathbf{V}$  and  $V_v$  is  $\theta_h$ . As described above,  $H_C$  etc., were measured as the differential pressures relative to the static-pressure tube. The probes were calibrated in the range  $-45^\circ \leq \theta_h \leq 45^\circ$  and  $-45^\circ \leq \beta_v \leq 45^\circ$  with five-degree steps in  $\theta_h$  and  $\beta_v$ . The following calibration coefficients were then calculated:

$$M(\theta_h, \beta_v) = (4H_C - H_T - H_B - H_P - H_S) / (V^2/2g) \quad (\text{II-1})$$

$$K(\theta_h, \beta_v) = (H_T - H_B) / (4H_C - H_T - H_B - H_P - H_S) \quad (\text{II-2})$$

$$L(\theta_h, \beta_v) = (H_S - H_P) / (4H_C - H_T - H_B - H_P - H_S) \quad (\text{II-3})$$

$$P(\theta_h, \beta_v) = H_C / (V^2/2g) \quad (\text{II-4})$$

where  $g$  is the gravitational acceleration,  $V^2 = \mathbf{V} \cdot \mathbf{V}$ , and  $\tan \theta_h = \cos \beta_v \tan \beta_h$ . These coefficients are shown in figure 11.

The procedure for evaluating the mean-velocity components ( $u, v, w$ ) and pressure  $p$  from the local probe measurements and the above calibration coefficients is as follows. The probe is positioned such that local probe coordinates ( $X, Y, Z$ ) are parallel to the global hull coordinates ( $x, y, z$ ). Designating local measured values with a prime, the following quantities are determined:

$$M' = 4H'_C - H'_T - H'_B - H'_P - H'_S \quad (\text{II-5})$$

$$K' = (H'_T - H'_B) / (4H'_C - H'_T - H'_B - H'_P - H'_S) \quad (\text{II-6})$$

$$L' = (H'_S - H'_P) / (4H'_C - H'_T - H'_B - H'_P - H'_S) \quad (\text{II-7})$$

$\theta'_h$  and  $\beta'_v$  are determined from  $K'$  and  $L'$  using the calibration coefficients shown in figures 11a and 11b. These are then used to determine  $M$  and  $P$ , respectively, from figures 11c and 11e, or 11d and 11f. As a result, the following are obtained:

$$\beta'_h = \tan^{-1}(\tan\theta'_h/\cos\beta'_v) \quad (\text{II-8})$$

$$V' = \sqrt{2gM'/M} \quad (\text{II-9})$$

$$V'_h = V' \cos\beta'_v / \sqrt{1 - \sin^2\beta'_v \sin^2\beta'_h} \quad (\text{II-10})$$

$$V'_v = V' \cos\beta'_h / \sqrt{1 - \sin^2\beta'_v \sin^2\beta'_h} \quad (\text{II-11})$$

$$C_p = 2(p - p_o)/\rho U^2 = (H'_C - PV'^2/2g)/(U^2/2g) \quad (\text{III-12})$$

where  $p_o$  and  $U$  are the pressure and velocity in the undisturbed uniform stream. Finally, the velocity components are determined as:

$$u = V'_h \cos\beta'_h \quad (\text{II-13})$$

$$v = V'_h \sin\beta'_h \quad (\text{II-14})$$

$$w = V'_v \sin\beta'_v \quad (\text{II-15})$$

Figure 8b provides a block diagram of the overall data analysis procedure. A computer program was used for data analysis in which values at desired points are obtained by Lagrange interpolation.

#### D. Data-Acquisition System

The data-acquisition system is a microcomputer PC9801 VM2 with two 8 channel A-D converter boards and a digital IO board which controlled the stepper motors and scanivalves. The pressures sensed from either the probes or pressure taps were converted to voltage by the transducers and then filtered by a low-pass filter and sampled through the A-D converter. A sampling frequency of 8Hz was used in all the experiments.

## E. Experimental Procedures

Six types of measurements were made: resistance, propeller open-water, self-propulsion, wave-profiles, surface-pressure distribution, and mean-velocity and pressure field. In all cases, a time interval of about 15 minutes between carriage runs (i.e., maximum of four runs per hour) was necessary in order for the fluid motion induced by the previous run to be sufficiently damped. All measurements are for the full-load condition. First, resistance and self-propulsion tests as well as wave-profile measurements were made. Based on these, the conditions for the subsequent detailed measurements were selected.

The resistance and propulsion tests were carried out following standard towing-tank procedures. Both tests were for the model-free condition (i.e., model was free to sink and trim). The dynamometers were calibrated before and after the measurements in all experiments. Force measurements were made for about 20 seconds after the carriage attained steady speed. An automated clamp was used to secure the hull while the carriage was accelerating or decelerating. Measurements were performed for the following conditions: carriage speed,  $.5 \leq U \leq 1.7\text{m/s}$ ; Froude number,  $.08 \leq Fr \leq .27$ ; and Reynolds number,  $1.6 \times 10^6 \leq Re \leq 5.4 \times 10^6$ .

The propeller open-water test was performed with the number of propeller revolutions constant, i.e.,  $n = 10\text{rps}$  ( $nD_p^2/\nu = 1.7 \times 10^5$ ). The carriage speed range was  $0 \leq U \leq 1.55\text{m/s}$  ( $0 \leq J \leq 1.1$ ). Self-propulsion tests were performed for six speeds  $U = (.7, .8, .9, 1, 1.1, 1.2\text{m/s})$ . The corresponding Froude numbers are  $Fr = (.112, .128, .144, .16, .176, .192)$ . For each speed, thrust, torque, and resistance were measured with the load varying from zero to the model self-propulsion point.

The wave profiles were recorded only for the model-fixed condition (i.e., model was fixed at the design draft). This was done photographically using both 35mm and video cameras, and normal processing.

For the detailed measurements, the speed was selected as  $U = 1\text{m/s}$  in order to minimize free-surface effects and to aid in maintaining measurement accuracy. The number of propeller revolutions for the with-propeller condition was  $7.8\text{rps}$ , and the corresponding thrust and torque were  $.0667\text{N}$



and .0017Nm, respectively. These are all close to the model self-propulsion point for this model speed. Under these conditions, the propeller influence is large. All the measurements were made for the model-fixed condition. The important nondimensional parameters have the following values (see List of Symbols for definitions):

$$Fr = U/\sqrt{gL} = .16$$

$$Re = UL/\nu \sim 3.94 \times 10^6$$

$$C_T = 2T/\rho U^2 \pi (R_p^2 - r_h^2) = .803$$

(II-16)

$$K_T = T/\rho n^2 D_p^4 = .234$$

$$K_Q = Q/\rho n^2 D_p^5 = .0411$$

$$J = U_A/nD_p = .654$$

For the surface-pressure distribution, three measurements were made per carriage run. The first measurement was used to check the zero point and the following two to measure pressures at four points by using the two transducers. The change was carried out every 20m (i.e., 20s) with a photo-switch system. Measurements were made at nine axial stations and along three waterlines for both the with- and without-propeller conditions, on both the port and starboard sides of the hull.

For the mean-velocity and pressure fields, four measurements were carried out per carriage run (i.e., eight points were measured by use of the port and starboard probes). For the 1m/s condition, the carriage ran steadily for about 65 seconds. It took about one second to traverse the probe from one point to the next, and the probe response time was about two seconds. Therefore, ten seconds were used to make measurements at each point, with the last six seconds used to obtain averages. The traverse was carried out every 15m by a photo-switch on the carriage and shutter plates on the cat walk. The probes usually had small setting angles (1 to 2°), and in some cases fairly large preset angles (around 10°) so that measure-

ments could be performed close to the hull. The flow angles were corrected based on measurements in uniform flow. The mean-velocity and pressure field measurements were also performed under both conditions, i.e., with and without propeller, and on both sides of the hull, for up to thirteen axial stations ( $0.5 \leq x \leq 1.1$ ). For stations far upstream of the propeller and, of course, the propeller plane itself, the measurements were made for the without-propeller condition only. Measurements at about 400 - 700 points were made at each transverse ( $x = \text{constant}$ ) section. The locations for both the surface-pressure distribution and mean-velocity and pressure field measurements are summarized in Table 2.

#### **F. Experimental Uncertainty**

The accuracy of the mean-velocity measurements is estimated to be within 1.5% for the magnitude and 1 degree for the direction. The accuracy of the measurement of the pressure coefficient  $C_p$  is estimated to be within  $\pm .01$  and  $\pm .05$  for the surface and field values, respectively.

### **III. RESULTS**

In the following, the detailed experimental results are presented and discussed to point out the essential features of the flow for both the with- and without-propeller conditions. In most cases, the results for the without-propeller condition are discussed first, followed by those for the with-propeller condition. Although not discussed in the Introduction, in comparison to the situation for propeller-hull interaction, a considerable amount of detailed experimental information is available for the mean-flow over the stern and in the near wake for bare ship hulls either for double bodies or at low Fr. Most of the experiments are for merchant ships, fairly similar to the Series 60  $C_B = .6$ , but with larger block coefficients ( $C_B \sim .8$ ). Several interpretations have been given to the vortical flow patterns (and attendant complicated velocity contours) associated with the afterbody flow (i.e., the flow over the stern and in the near wake) for these hull forms. This is exemplified by the range of terminology used to describe them, e.g., bilge vortices, three-dimensional separation, and longitudinal vorticity. For a recent review of this topic, see Patel (1988). Below, we shall simply point out these features with the primary emphasis on their modification due to the action of the propeller.

## A. Resistance and Propulsion Tests

Resistance tests were performed to provide data for evaluating the thrust-deduction factor. Also, as will now be discussed, it was of interest to compare the present results with those of the CEP (see Chapter I).

Figure 12 shows a comparison of the present results for the total-resistance coefficient  $C_T$  with one of those obtained in the CEP, namely, Akishima Laboratories, MITSUI ZOSEN (ALM). Although the trends are very similar, the present values are slightly smaller. However, of the four sets of results of the CEP for 4m models, the ALM results indicated the largest values.

The residuary-resistance coefficient  $C_R$  is shown in figure 13 along with the three mean  $C_R$  curves for the different model-size groups of the CEP. Although the present results are in agreement with those for the larger model-size group, they show somewhat larger humps and hollows than the mean curves. This is due to the averaging technique used to define the mean curves since similar humps and hollows at nearly the same  $Fr$  are evident in the individual curves, e.g., the 10m (NKK) and 2.5m (UT) model results in the original reference (ITTC, 1987).

Based on the above comparisons, it is concluded that the present results are in close agreement with those obtained in the CEP, in spite of the small modification made to the stern geometry to attach the propeller (see Section II.A and figure 3).

The propeller open-water test was performed to investigate the propeller performance in uniform flow and to provide data for evaluating the effective-wake factor and relative rotative efficiency based on the thrust-identity method. The results are shown by open symbols in standard format in figure 14. As expected, the value of  $J$  at which  $K_T = 0$  is a little larger than the geometrical pitch ratio. Also, note the rather wide range of  $J$  for which the propeller efficiency is large. The present results are in close agreement (figure not shown) with those of the MAU methodical series tests of Tsuchida et al. (1958).

The self-propulsion test results are shown in figure 15. Figure 15a shows the results for all six speeds tested, whereas figure 15b is for  $U = 1\text{m/s}$  which is the speed for the detailed measurements. As expected from physical considerations, the towing force  $R$  decreases with increasing thrust  $T$ . The decrease of  $R$  is smaller than the increase of  $T$ . The  $R$  vs.  $T$  relationship is almost linear with the same slope (about  $-.9$ ) for each  $U$ . Therefore, if this slope is used to define the thrust-deduction factor, it would be nearly constant for all load conditions and  $Fr$ . However, the usual definition, i.e.

$$(1-t) = (R_0 - R)/T \quad (\text{III-1})$$

where  $R_0$  is the without-propeller resistance, is used below. Figure 15b also shows  $R_0$  and  $(T + R)$  vs.  $T$ . It is seen that the interaction between the propeller and hull is weak for  $T = 0$  (i.e.,  $R(T = 0)$  is slightly larger than  $R_0$ ) and increases gradually with  $T$ .

The usual self-propulsion factors are shown vs. thrust-loading coefficient  $C_T$  for each  $U$  in figure 16. As already mentioned, the effective-wake factor  $(1-w)$  and relative rotative efficiency  $(\eta_R)$  were determined based on the thrust-identity method (e.g., Todd, 1967), i.e.

$$(1-w) = U_A \quad (\text{III-2})$$

$$\eta_R = Q_0/Q$$

where  $U_A$  is the speed of advance and  $Q_0$  the torque in open water, i.e., the speed and torque in uniform flow at which the propeller would produce the same thrust at the same revolutions per second as that measured behind the model. The effective-wake factor  $(1-w)$ , shown in figure 16a, increases gradually with  $C_T$  due to the propeller-induced flow contraction and axial acceleration. This is consistent with previous work in which it is also shown that the increase can be significant for hulls with large block coefficients (e.g., Nagamatsu and Sasajima, 1975). Note that the nominal volume mean velocity for  $U = 1\text{m/s}$  is  $.66$ . The thrust-deduction factor  $(1 - t)$ , shown in figure 16b, also increases gradually with  $C_T$ , in this case,

due to the resistance increase for  $T = 0$ . Lastly, the relative-rotative efficiency  $\eta_R$ , shown in figure 16c, is nearly constant, but shows some scatter for small  $C_T$  due to difficulties in measuring small values of torque. For the low  $Fr$  range of the present self-propulsion tests ( $.1 < Fr < .2$ ), the self-propulsion factors have almost constant values if plotted vs.  $Fr$  for fixed  $C_T$ , which is the usual format, e.g., at the model self-propulsion point  $C_T \approx .8$ ,  $(1 - w) = U_A = .74-.75$ ,  $(1 - t) = .86-.87$ , and  $\eta_R = 1-1.02$  for all  $Fr$ . However, based on previous work (e.g., Yamazaki and Nakatake, 1984), these factors are expected to vary with  $Fr$  for larger  $Fr$ .

### B. Wave Profiles

The wave profiles at the hull were measured using both 35mm and video cameras. The profiles for  $Fr = (.3, .25, .16)$  are shown in figure 17, including for the former two cases, comparisons with results from the CEP. Although there are some differences in the experimental conditions, the present results are in close agreement with those of the CEP. For  $Fr = .16$ , which is the condition for the detailed measurements, results are shown for both the with- and without-propeller conditions. It is seen that the propeller influence is negligible for  $x \leq .9$ . For  $.9 < x \leq .98$ , the wave elevation with propeller is less than without, but for  $.98 \leq x \leq 1$  the reverse holds true. As will be shown below, this correlates with the pressure measurements and is associated with the propeller thrust.

### C. Surface-Pressure Distributions

The surface-pressure distributions are shown in figures 18 through 20. The pressure-tap locations are shown in figure 5a. Figure 18 shows the pressure contours for both the with- and without-propeller conditions as well as for the difference between the two conditions. The results presented are for the port side only since, as will be shown below, the distributions are nearly symmetric. For the without-propeller condition, it is seen that the pressure is relatively low near the keel and the pressure recovery is larger for waterlines near the free surface. For the with-propeller condition, the expected pressure decrease is observed near the propeller, except above the propeller, where there is an increase. The

pressure decrease is larger in the lower part of the propeller disk than the upper, where the boundary layer is thick. At large distances upstream from the propeller ( $x \lesssim .95$ ), the pressure-difference contours are uniform with depth, whereas for smaller distances, they are curved towards the outer propeller radii. The influence of the propeller is restricted to  $x \gtrsim .9$  (which is about two diameters upstream of the propeller).

The girthwise and streamwise variations (figures 19 and 20, respectively) show the same trends as just described. Figure 19 shows that the magnitude of the pressure decrease is almost the same from the keel to the free surface for  $x < .95$ , but for  $.95 \leq x \leq 1$ , there is a large girthwise variation indicating a pressure decrease except above the propeller. Figure 20 shows that for the without-propeller condition, the port and starboard pressure variations are very nearly symmetric. The asymmetry is, no doubt, due to slight variations in the geometry of the pressure taps. The with-propeller condition results are less symmetric, but the differences between the port and starboard trends are difficult to discern. Near the propeller plane, the magnitude of the pressure decrease clearly depends on the propeller spanwise loading distribution (i.e.,  $(z-z_0)/R_p$ ). Also, the  $z = .008$  results (figure 20a) are quite similar to the wave elevation (cf. figure 17).

#### D. Mean-Velocity and Pressure Fields

The mean-velocity and pressure fields for the with- and without-propeller conditions are shown in figures 21 through 23. Figure 21 shows the mean-velocity vectors projected onto the crossplane and the contours of axial velocity. Figures 22 and 23 show the axial vorticity,  $\omega_x = (v_z - w_y)$ , and pressure contours, respectively.

Considering the without-propeller condition first, it is seen from figure 21a that, at the first measurement station,  $x = .5$ , the flow diverges off the bilge such that the boundary layer is thicker near the centerplane and the free surface than in the bilge region. However, at  $x = .6$  (figure 21b), which may be regarded as the beginning of the afterbody flow, the flow diverges off the centerplane such that the boundary-layer thickness is nearly uniform around the entire girth. For both these sta-

tions ( $x = .5, .6$ ), the crossplane flow is very small. It appears that, for this particular experiment,  $x = .6$  may be an ideal station to initiate stern-flow calculations with initial conditions based on simple two-dimensional boundary-layer correlations. Subsequently, at  $x = .7$  and  $.8$  (figures 21c,d), the flow begins to exhibit features that are well known for this type of hull form, features which become quite evident in the stern region,  $x = .9, .95, .975$ , and  $.98125$  (figures 21e-h). That is, the diminishing cross-section of the hull at the stern and the associated convergence of the inviscid streamlines leads to a thickening of the region of viscous flow, except near the keel where there is a thinning due to flow divergence off of the centerplane. Generally, the crossplane flow is directed upwards and towards the hull centerplane. Also, as will be discussed further below, quite apparent in the crossplane velocity vectors is the presence of a weak longitudinal vortex. The pronounced bulge in boundary-layer thickness near the region of maximum hull concavity and the rather complicated flow in the vicinity of the stern tube are particularly noteworthy. Finally, in the region  $.9875 \leq x \leq 1.1$  (figures 21i-m), the near wake shows relatively fast decay of the transverse velocity components and the initial stages of wake recovery. There is a gradual increase in the wake centerplane velocity and diffusion of the wake. Note the change in the shape of the wake as it evolves, indicating a relatively slower recovery near the free surface and wake centerplane. Some of these trends are due to the downward convection associated with the weak longitudinal vortex and the general upward motion of the external inviscid flow in this region.

For the with-propeller condition, at  $x = .9$  (figure 21e), the influence of the propeller is negligible, although there is a slight decrease in boundary-layer thickness. Subsequently, at  $x = .95, .975$ , and  $.98125$  (figures 21f-h), the propeller influence becomes increasingly apparent as the propeller plane ( $x = .9875$ ) is approached, especially in the axial velocity contours which exhibit increased velocity near the hull due to the combined effects of the propeller-induced flow contraction and axial acceleration. Also, evident in the crossplane vectors is a slight turning of the flow, i.e., the crossplane vectors are turned towards the propeller axis and increase slightly in magnitude due to a small, but discernible, propeller-

induced radial velocity. The vortical flow is still present, but appears to be compressed towards the hull. Note that the flow upstream of the propeller is nearly symmetric with respect to the hull centerplane. The flow in the propeller slipstream,  $x = 1, 1.01875, 1.05$ , and  $1.1$  (figures 2lj-m), is, of course, completely altered due to the action of the propeller, indicating characteristics which are similar to a swirling jet and a complex interaction between the hull boundary layer and wake and the propeller-induced flow. Quite obvious is the propeller-induced flow asymmetry within the propeller slipstream with respect to the hull centerplane, including a very significant drift of the wake centerplane off the hull centerplane towards the port side of the hull. Outside the propeller slipstream, the flow is nearly symmetric with respect to the hull centerplane. The swirl velocity is maximum just downstream of the propeller (figure 2lj) and then decays relatively rapidly in the near wake (figures 2lk-m). The swirl profiles reflect the complex interaction between the propeller and the hull boundary layer and wake, and cannot be explained simply as a superposition of the bare-hull and propeller-induced flows. Figures 2lk-m also suggest the occurrence of a secondary vortex on the starboard side of the hull near the free surface. The axial velocity contours indicate that the slipstream flow initially accelerates (figures 2lj-l) and then undergoes a rapid deceleration and gradual diffusion (figure 2lm). Considerably higher velocities are found on the starboard than on the port side of the hull. The concentration of the axial velocity contours in figures 2lj-l are, no doubt, the trace of the blade-tip vortices and its associated vortex sheet in the near wake (figures 2lj,k) which then diffuses with downstream distance (figures 2ll,m).

Next, we consider the characteristics of the axial vorticity contours shown in figure 22. These were determined by differentiation of the cross-plane velocity field, made possible by the closely-spaced Cartesian grid used in the measurements. For the without-propeller condition, the axial vorticity is small at the upstream stations ( $.5 \leq x \leq .8$ ) where the cross-plane flow is also small, and therefore, the flow is nearly two-dimensional (figures 22a-d). Subsequently ( $x = .9$  and  $.95$ ), there is a significant increase in the axial vorticity. This is primarily due to the developing three-dimensionality of the flow and the associated rotation of the bound-



ary-layer vorticity towards the axial direction (figures 22e,f). Finally, in the stern and near wake regions ( $.975 \leq x \leq 1.1$ ), the axial vorticity exhibits the expected pattern associated with the rapid boundary-layer thickening and weak longitudinal vortex typical for this type of hull form (figures 22g-m). Note the rather slow decay rate of the axial vorticity which can be correlated with, but is much slower than, that of the cross-plane flow. For the with-propeller condition, at  $x = .9$  and  $.95$  (figures 22e,f), the influence of the propeller is negligible. At  $x = .975$  and  $.98125$  (figures 22g,h), the axial vorticity shows an increase and a change in shape near the hull (i.e., the contours are compressed towards the hull centerplane) due to the propeller-induced flow contraction and axial acceleration. In the propeller slipstream,  $x = 1, 1.01875, 1.05$ , and  $1.1$  (figures 22j-m), the axial vorticity is very large. The regions of large negative and positive vorticity correspond, respectively, to the vortices from the blade-tips and the propeller hub. The flow asymmetry within the propeller disk with respect to the hull centerplane is quite apparent. The decay of axial vorticity with downstream distance again correlates with the crossplane velocity field described earlier, but with a considerably slower rate. Also, note the presence of both the primary and secondary propeller-induced vortices.

Lastly for this chapter, we consider the characteristics of the pressure field shown in figure 23. From the outset we should point out that the measurement of pressure in the flow field is difficult and the accuracy is limited (see Section II.F). As a result, the port and starboard results, even for the without-propeller condition, exhibit some anomalous differences and scatter. In general, the trends for both the with- and without-propeller conditions are consistent with the surface-pressure measurements (figures 18 through 20), but with some differences in the pressure magnitude, especially for the port side of the hull, due to the differences in the measurement technique and analysis methods. For the without-propeller condition, the pressure is largest near the hull and gradually decreases across the viscous- and inviscid-flow regions. The cross-plane variations are surprisingly uniform in view of the crossplane velocity field, although relatively lower pressures are found in the core region of the vortical flow. For the with-propeller condition, at  $x = .9$  (figure

23e), the influence of the propeller is negligible. Subsequently, at  $x = .95$ ,  $.975$ , and  $.98125$  (figures 23f-h), the influence becomes increasingly apparent as the propeller plane is approached. There is a large drop in pressure associated with the propeller thrust and the shape of the pressure contours is changed remarkably due to the propeller-induced flow contraction and axial acceleration, the pressure contours being nearly circular within the propeller disk. The pressure contours upstream of the propeller are nearly symmetric with respect to the hull centerplane. Immediately downstream of the propeller, at  $x = 1$  (figure 23j), there is a large increase in pressure, associated with the propeller thrust, except at the center of the slipstream where there is a low pressure region associated with the hub vortex. At this station, the pressure contours are asymmetric with respect to the hull centerplane. Considerably larger pressures are found on the starboard than on the port side of the hull. Finally, at  $x = 1.05$ ,  $1.01875$ , and  $1.1$  (figures 23k-m), there is a rapid decrease in pressure. This is consistent with the previously mentioned initial axial velocity increase in this region. The pressure field changes rapidly such that the contours become circular and nearly symmetric with respect to the wake centerplane. The continued presence of the low pressure region near the center of the slipstream indicates the hub vortex. It is interesting to observe that, unlike the axial velocity contours, the pressure contours have a similar shape (i.e., circular) within the propeller disk both upstream and downstream (except immediately downstream) of the propeller.

#### IV. PROPELLER-HULL INTERACTION

The foregoing discussion of the experimental results clearly indicates the complexity of the interaction between the propeller-induced flow and the hull boundary layer and wake. In this section, the results are analyzed further to assess the nature of this interaction. To this end, use is made of the Kerwin and Lee (1978) propeller-performance program with both nominal and effective inflows. The effective inflow was calculated using the method of Toda et al. (1987), who extended the method of Huang and associates (1976, 1980) for axisymmetric bodies to three-dimensional bodies. Since the method of Toda et al. (1987) is of general interest, an English translation has been provided as Appendix I.

Some modifications of the propeller-performance program were required in order to perform the present calculations. These included changes to handle the MAU propeller geometry and, as discussed further below, to evaluate the time-averaged angular and radial variation of thrust and torque for three-dimensional nonuniform inflow. In the discussions to follow, a cylindrical coordinate system  $(x,r,\theta)$  is adopted in which  $x$  coincides with the propeller shaft and is positive downstream,  $r$  is the radial distance from the  $x$ -axis, and  $\theta$  is the angle measured from top dead center and positive clockwise looking upstream (figure 4b). The mean-velocity components in the directions of the coordinate axes are denoted by  $(V_x, V_r, V_\theta)$ .

Before discussing propeller-hull interaction, it is helpful to first examine the propeller performance. Initial calculations were made for uniform inflow, i.e., the open-water condition. Referring to figure 14, it is seen that the calculations are in close agreement with the present experimental results. Also, the calculated spanwise circulation distribution  $\Gamma$  shown in figure 24b is typical, including the maximum value  $\Gamma_{\max}$  at  $r/R_p = .7$ .

Next, consideration is given to the results for the nominal inflow. The nominal inflow was obtained from the measurements in the propeller plane ( $x = .9875$ ) for the without-propeller condition (figure 21i). First, the velocity components were transformed from the Cartesian  $(x,y,z)$  to the cylindrical  $(x,r,\theta)$  coordinates, and then interpolated onto a fixed set of radii and expanded in a Fourier series in  $\theta$ . The axial  $V_x$  and tangential  $V_\theta$  velocity components obtained for  $r/R_p = .7$  are shown in figure 25. The circumferential-average axial velocity is shown vs.  $r/R_p$  in figure 24a. Figure 24 shows both the circumferential-average (figure 24b) and angular variation (figure 24c) of the spanwise circulation distribution  $\Gamma$ . It is clear from figure 24b that, for nonuniform inflow (i.e., the nominal inflow), the circumferential-average  $\Gamma$  changes significantly compared to the uniform-inflow distribution,  $\Gamma$  being considerably larger near the root and slightly smaller near the tip than that for uniform inflow. With nonuniform inflow,  $\Gamma_{\max}$  is larger and occurs at  $r/R_p = .6$ . These changes are due to the increase near the root and decrease near the tip of the circumferential-average section angle of attack for the nonuniform-inflow condition. Note that  $J = .581$  based on the nominal volume mean velocity. The

angular variation of  $\Gamma$  shown in figure 24c can also be correlated with variations in the section angle of attack:

$$\alpha = \phi - \beta_I \quad (IV-1)$$

with

$$\beta_I = \tan^{-1} \frac{V_x + V_{Px}}{2\pi n - V_{P\theta}} \quad (IV-2)$$

In (IV-1),  $\phi$  is the geometric-pitch angle and  $\beta_I$  the hydrodynamic-pitch angle defined by (IV-2), in which  $V_{Px}$  and  $V_{P\theta}$  are the axial and tangential components, respectively, of the propeller-induced velocity, which depend upon the inflow velocity ( $V_x$  and  $V_\theta$ ). Thus, we see that  $\Gamma$  is large for  $0^\circ \lesssim \theta_p \lesssim 90^\circ$  and  $\theta_p \approx -150^\circ$  mainly due to the effects of the nominal axial velocity  $V_x$ , but also due to the influence of the nominal tangential velocity  $V_\theta$  (i.e., influence of the crossplane flow which is directed upwards and towards the centerplane) for  $\theta_p \approx \pm 90^\circ$ .

For a three-dimensional nonuniform inflow, the total unsteady blade thrust  $K_T$  includes contributions from both circulation ( $K_{Tc}$ ) and added mass ( $K_{Ta}$ ). These are shown vs.  $\theta_p$  in figure 25. Results are shown both with and without the nominal tangential velocity  $V_\theta$ . Also shown is the variation of the nominal axial velocity  $V_x$  for  $r/R_p = .7$ . First, we consider the results without  $V_\theta$ .  $K_{Tc}(\theta_p)$  is, as expected, based on  $\Gamma(\theta_p)$  and nearly symmetric with respect to its maximum value at  $\theta_p = -24^\circ$ .  $K_{Ta}(\theta_p)$ , which by definition is almost proportional to  $d\Gamma/dt$ , is nearly antisymmetric with respect to  $\theta_p = 0$ .  $K_{Tc}$  and  $K_{Ta}$  combine such that the total thrust  $K_T$  is also nearly symmetric with respect to its peak value at  $\theta_p = 8^\circ$ , and furthermore, can be directly correlated as a quasi-steady response to  $V_x(\theta_p)$ . Although the results including  $V_\theta$  are similar, there is a remarkable difference such that  $K_T$  and  $K_{Tc}$  are no longer symmetric, but indicate significantly larger values on the starboard than on the port side of the hull. This important influence of  $V_\theta$  on the propeller loading will be discussed further below.

The experiments described above involved steady mean-flow measurements, i.e., averages were taken over a sufficient length of time to remove

the unsteadiness of both the turbulence and the propeller to define time-mean values. Therefore, to relate the propeller performance to the mean-flow measurements, of importance is not the unsteady blade thrust and torque, but rather the time-averaged angular variation of thrust and torque. As mentioned above, the propeller-performance program was modified to provide the latter. The usual definitions for unsteady blade thrust and torque are

$$K_T(\theta_p) = \frac{1}{\rho n^2 D_p^4} \int_{r_h}^{R_p} \int_{\xi_{TE}}^{\xi_{LE}} f_x(r, \xi, \theta_p) r d\xi dr \quad (IV-3)$$

$$K_Q(\theta_p) = \frac{1}{\rho n^2 D_p^5} \int_{r_h}^{R_p} \int_{\xi_{TE}}^{\xi_{LE}} f_\theta(r, \xi, \theta_p) r^2 d\xi dr \quad (IV-4)$$

where

$$f_x = \Delta p n \cdot e_x \quad (IV-5)$$

$$f_\theta = \Delta p n \cdot e_\theta$$

and  $\xi = \theta - \theta_p$  and  $\theta_p = 2\pi n t$  (see List of Symbols for definitions). On the other hand, the definitions for the time-averaged angular variation of thrust and torque are

$$\bar{K}_T(\theta) = \int_{r_h}^{R_p} \bar{f}_x(r, \theta) r dr \quad (IV-6)$$

$$\bar{K}_Q(\theta) = \int_{r_h}^{R_p} \bar{f}_\theta(r, \theta) r^2 dr \quad (IV-7)$$

where

$$\bar{f}_x = \frac{N}{2\pi \rho n^2 D_p^4} \int_0^{2\pi} f_x(r, \theta - \theta_p, \theta_p) d\theta_p \quad (IV-8)$$

$$\bar{f}_\theta = \frac{N}{2\pi \rho n^2 D_p^5} \int_0^{2\pi} f_\theta(r, \theta - \theta_p, \theta_p) d\theta_p \quad (IV-9)$$

The steady thrust and torque are obtained equivalently by either time-averaging (i.e., averaging over  $\theta_p$ ) (IV-3) and (IV-4), or circumferentially-averaging (i.e., averaging over  $\theta$ ) (IV-6) and (IV-7). The calculated values based on the nominal inflow are compared with the present measurements in Table 5. It is seen that the calculated values overpredict the thrust and torque by about 13% and 8%, respectively. Also shown in Table 5 are the calculated steady side forces and moments as well as the three components of the unsteady first blade harmonic forces and moments, although none of these quantities were measured.

Figure 26 shows a comparison of the unsteady and time-averaged angular variation of blade thrust and torque. For comparison purposes,  $\bar{K}_T(\theta)$  and  $\bar{K}_Q(\theta)$ , which represent total thrust and torque, are converted to per blade values by the multiplicative factor  $2\pi/N$ , where  $N$  is the number of blades. It is seen that both the unsteady and time-averaged angular varying thrust and torque are quite similar. The main difference is that the time-averaged angular varying values are shifted towards the 1/4 chord (forward of the blade generator line, see figure 4b) relative to the unsteady values. We also see significantly larger loading on the starboard than the port side of the hull for reasons mentioned earlier. To display further the characteristics of the propeller loading, figure 27a,b shows the time-averaged angular and radially varying thrust and torque contours, i.e.,  $\bar{f}_x(r,\theta)$  and  $\bar{f}_\theta(r,\theta)$ , defined in (IV-8) and (IV-9), respectively. Also shown in parentheses on figure 27a are the corresponding thrust-loading values (i.e.,  $2n^2 D_p^2 \bar{f}_x / U^2$ ). Clearly evident are the large values of thrust for  $0 \lesssim \theta \lesssim 90^\circ$  and near  $\theta \approx -150^\circ$  (figure 27a). Also, note that, in the lower part of the propeller disk near the hub, the thrust is generally larger on the starboard than the port side of the hull, in this case, due to the influence of the weak longitudinal vortex. The torque contours are similar to those for thrust, but with greater symmetry and more gradual variations (figure 27b).

Lastly, regarding the propeller performance, consideration is given to the results for the effective inflow. As mentioned above, the effective inflow was calculated using the method of Toda et al. (1987) (see Appendix I). In this approach, the method of Huang and associates (1976, 1980) is applied two-dimensionally in x-y planes (i.e., for  $z = \text{constant}$ ) to obtain

the lateral propeller-induced flow contraction. The vertical contraction is determined based on that for the propeller operating in open water with the same advance coefficient as the model (or ship). For the present application, only the axial component of the effective inflow was calculated, since for fine hull forms, the effects of the propeller on the crossplane components for the region upstream of the propeller are quite small (see figures 21f-h, also Kasahara (1985)). As will be shown below, the primary differences between the nominal and effective inflows are that the latter has increased velocity and uniformity.

Included in figure 24 are the circumferential-average axial velocity (figure 24a) and the spanwise circulation distribution  $\Gamma$  (figure 24b) for the effective inflow. Although the shape of the distribution for the effective inflow is similar to that for the nominal inflow, there is a slight shift towards the uniform-inflow distribution. With the effective inflow,  $\Gamma_{\max}$  is smaller than that for either the nominal or uniform inflow and occurs at  $r/R_p = .64$ . These differences between the results for the nominal and effective inflows are due to the increased uniformity of the latter resulting in smaller section angle of attack variations. This effect is clearly demonstrated by the circumferential-average axial velocity (figure 24a), which also shows that the largest increases in velocity for the effective inflow are for the inner radii.

Figure 28 shows a comparison of the unsteady and time-averaged angular variation (converted to per-blade values) of blade thrust and torque for the effective inflow. Also shown is the variation of the effective axial velocity  $V_x$  at  $r/R_p = .7$  as well as that for the nominal inflow, reproduced here from figure 25 for the purpose of direct comparison. Quite apparent is the already pointed out increased velocity and uniformity of the effective as compared to the nominal inflow. The velocity increase is nearly the same for all angular positions ( $\theta$  or  $\theta_p$ ). A comparison of figures 26 and 28 indicates that the results for the effective inflow are similar and consistent with those described earlier for the nominal inflow, but with decreased values and differences between the starboard and port sides of the hull for reasons mentioned earlier. Also included in Table 5 are the calculated values of steady and first blade harmonic forces and moments based on the effective inflow. It is seen that, in this case, the calcula-

tions for the steady thrust and torque are in excellent agreement with the measurements.

Finally, for the effective inflow, figure 29 shows the time-averaged angular and radially varying thrust  $\bar{f}_x(r,\theta)$  (figure 29a) and torque  $\bar{f}_\theta(r,\theta)$  (figure 29b) contours using the same format as figure 27. A comparison of figures 27 and 29 indicates that, here again, the results for the effective inflow are similar and consistent with those described earlier for the nominal inflow, but with decreased values, especially near the hull centerplane, for reasons mentioned earlier. For the present application, it appears that the effective and nominal inflows are qualitatively, but not quantitatively, similar.

Keeping in mind the above discussion of propeller performance, consideration is now given to propeller-hull interaction. First, we consider the interaction for the region upstream of the propeller plane. In order to aid in explaining the propeller effects pointed out earlier, figure 30 shows contours of the difference in axial velocity  $\Delta u$  between the with- and without-propeller conditions for  $x = .975$  and  $.98125$ . Also shown is  $\Delta u$  vs.  $y$  at various horizontal planes. The circumferential-averaged propeller-induced axial velocity  $V_{px}$  for both the nominal and effective inflows is included for comparison. Unfortunately, our version of the propeller-performance program only allows for the evaluation of steady (i.e., circumferentially averaged) field-point velocities. However, for the region upstream of the propeller plane, unsteady effects on the field-point velocities are negligible. It is apparent that the low-momentum fluid near the hull and in the longitudinal-vortex core undergo the largest axial acceleration. Within the propeller disk,  $\Delta u$  is considerably larger than  $V_{px}$  for both inflows, which indicates that the increase in velocity is not simply due to the superposition of the propeller-induced flow and the hull boundary layer, but the result of the contraction and axial acceleration of the hull boundary layer due to the action of the propeller. The magnitude of the axial acceleration depends both on hull proximity and on the distribution of propeller loading, i.e., radial location. The flow is very nearly symmetric with respect to the hull centerplane. Consistent with the previous discussion, the  $V_{px}$  values for both the nominal and effective inflow are quite similar, but with the latter slightly smaller due to its reduced loading.



Next, we consider the interaction in the propeller slipstream. As will now be discussed, most of the flow-field features pointed out earlier can be explained as a direct consequence of the time-averaged angular and radially varying propeller loading. A comparison of the loading contours (figures 27 and 29) with both the axial velocity (figure 21j,k) and pressure (figure 23j) contours in the very near wake indicates that all three have a very similar pattern, i.e., increased values on the starboard side of the hull for  $0^\circ \lesssim \theta_p \lesssim 90^\circ$  and on the port side for  $\theta_p \approx -150^\circ$  in comparison to the other regions within the propeller disk. Note that the increased values of pressure on the starboard as compared to the port side of the hull are, no doubt, the cause of the drift of the wake centerplane off the hull centerplane towards the port side. Subsequently, in the near wake, the axial velocity (figures 21l,m) and pressure (figures 23k-m) contours become more uniform due to diffusion. The rate of recovery of the pressure is considerably larger than that of the axial velocity. Thus, it appears that the propeller loading resulting from its operation in nonuniform inflow is responsible for the nature of the complicated flow within the propeller slipstream. This effect is further displayed in figure 31 which shows the difference in axial velocity contours between the with- and without-propeller conditions  $\Delta u$  for  $x = 1$ . Also shown is  $\Delta u$  vs.  $y$  for various horizontal planes, including the time-averaged angular and radially varying thrust  $\bar{f}_x$  and propeller-induced axial velocity  $V_{Px}$  for both the nominal and effective inflows for comparison. Note that  $\bar{f}_x$  and  $V_{Px}$  are evaluated at the propeller plane. Two methods were used to calculate  $V_{Px}$ . The first method is the propeller-performance program which, as already mentioned, provides circumferentially-averaged values. The second method is based on the momentum theorem, i.e.

$$V_{Px} = \frac{V_x}{2} (-1 + \sqrt{1 + 2n_D^2 \bar{f}_x / V_x^2}) \quad (\text{IV-10})$$

The latter method, although quite approximate, includes unsteady effects, which are known to be important in the propeller slipstream. A comparison of figures 31 and 27 or 29 indicates that the  $\Delta u$  contours show even greater similarity with the propeller loading than that noted above for the axial velocity and pressure contours. For  $z = .02$  and  $.045$  the shape of the  $\Delta u$

vs.  $y$  curves are nearly identical to those of  $\bar{f}_x$ . For  $z = .033$ , the differences between  $\Delta u$  and  $\bar{f}_x$  are due to the influence of the hub and its vortex. Just as was the case for the region upstream of the propeller plane, within the propeller disk,  $\Delta u$  is considerably larger than  $V_{px}$ , again indicating a significant acceleration of the hull boundary and wake due to the action of the propeller. However, in this case, only a qualitative assessment is possible due to the approximations involved in calculating  $V_{px}$  and due to the fact that the values shown are for the propeller plane and not  $x = 1$ . Note that the interaction is largest near the hull centerplane. Also, for  $z = .02$  the boundary layer is thick such that the  $\bar{f}_x$  and  $\Delta u$  curves are fairly broad, whereas for  $z = .045$  the boundary layer is thin and the  $\bar{f}_x$  and  $\Delta u$  curves are quite sharply peaked. Here again, the  $V_{px}$  values for both the nominal and effective inflow are quite similar. The differences are consistent with the previous discussions.

## V. CONCLUDING REMARKS

Detailed experimental information has been presented which documents the interaction between a propeller and the hull boundary layer and wake for a Series 60  $C_B = .6$  model ship. The experimental equipment and procedures have been described, and the results discussed to point out the essential differences between the flows with and without propeller. The results have been analyzed to assess the nature of the interaction between the propeller and the hull boundary layer and wake. To this end, use is made of a propeller-performance program with both nominal and effective inflows. The interaction for the region upstream of the propeller is mainly the result of the contraction and axial acceleration of the hull boundary layer due to the action of the propeller. Thus, for the present application, a simple prediction method for the effective inflow was shown to be adequate. However, for more complex geometries (e.g., full hull forms, appended bodies, etc.) it is expected that more comprehensive methods will be required. The interaction in the propeller slipstream is quite complicated, i.e., the flow is completely altered due to the action of the propeller, indicating characteristics which are similar to a swirling jet. However, most features can be explained as a direct consequence of the propeller loading resulting from its operation with a three-dimensional nonuniform inflow.

Although we have been able to qualitatively explain most of the experimental results solely with reference to the propeller loading predicted from a propeller-performance program with the nominal and effective inflows, it should be recognized that quantitative prediction of the complete flow field requires the use of advanced viscous-flow methods, including the effects of the propeller (Stern et al., 1988a). In fact, one of the motivations of the present study was to provide documentation of both the test conditions and results in sufficient detail to be useful as a test case for validating computational methods. The data discussed here are available on magnetic tape upon request from IIHR. A comparison of the present experimental results with the predictions of the method of Stern et al. (1988a) is in progress and will be reported in the near future.

Finally, with regard to the direction of future work, additional experiments in the intermediate- and far-wake regions are desirable to determine the evolution and recovery of the wake as well as experiments at higher  $Fr$  to determine free-surface effects. Also, of interest are experiments for other geometries, e.g., full hull forms, high-speed ships, and appended bodies.

## REFERENCES

- Baba, E. and Ikeda, T., (1979), "Flow Measurements in the Slipstream of a Self-Propelling Ship with and without Rudder," Trans. West Japan Soc. Naval Arch., Vol. 59, pp. 57-69 (in Japanese).
- Chen, C.N., (1964), "Turbulence Studies in the Wake Behind a Powered Surface Vessel," M.S. Thesis, Dept. of Mech. and Hydraulics, The University of Iowa.
- Cox, B.D. and Hansen, A.G., (1977), "A Method for Predicting Thrust Deduction Using Propeller Lifting-Surface Theory," DTNSRDC Report SPD-77-0087.
- Dyne, G., (1974), "A Study of the Scale Effect on Wake, Propeller Cavitation and Vibratory Pressure at Hull of Two Tanker Models," Trans SNAME, Vol. 82, pp. 162-185.
- Fujii, A. and Fukuda, K., (1984), "On the Hull Surface Pressure Under the Action of a Propeller," J. Kansai Soc. Naval Arch. Japan, Vol. 145, pp. 53-60 (in Japanese).
- Fujita, T., (1979), "On the Flow Measurement in High Wake Region at the Propeller Plane," J. Soc. Naval Arch. Japan, Vol. 145, pp. 1-7.
- Huang, T.T., Wang, H.T., Santelli, W. and Groves, N.C., (1976), "Propeller/Stern/Boundary-Layer Interaction on Axisymmetric Bodies: Theory and Experiment," DTNSRDC Report 76-0113.
- Huang, T.T. and Groves, N.C., (1980), "Effective Wake: Theory and Experiment," Proc. 13th ONR Sym. on Naval Hydro., Tokyo, Japan, pp. 651-673.
- Hucho, von W.H., (1967), "Untersuchungen uber den Einflub einer Hockshraube auf die Druckverteilung und die Grenzschicht schiffsahnlicher korper," Bericht 66/40, Institutes fur Stromungsmechanik der Technischen Hochschule Braunschweig (in German).
- Ishida, S., (1986), "The Influence of a Hull on the Rotational Energy in the Propeller Slipstream," Trans West Japan Soc. Naval Arch., Vol. 72, pp. 83-91 (in Japanese).
- ITTC, (1987), "Report of the Resistance and Flow Committee," Proc. 18th Int. Towing Tank Conf., Kobe, Japan, pp. 47-92.
- Kasahara, Y., (1985), "An Experimental Investigation of the Scale Effect on Nominal and Effective Wake Distributions Using Geosim Models of Two Different Ships," Proc. Osaka Int. Colloquium on Ship Viscous Flow, Osaka, Japan, pp. 432-449.
- Kasahara, Y., (1986), "Experimental Investigation of the Influence on the Stern Flow Field due to the Operating Propeller," J. Kansai Soc. Naval Arch. Japan, Vol. 202, pp. 29-37 (in Japanese).

Kerwin, J.E. and Lee, C.S., (1978), "Prediction of Steady and Unsteady Marine Propeller Performance by Numerical Lifting-Surface Theory," Trans. SNAME, Vol. 86, pp. 218-253.

Kux, J. and Laudan, J., (1984), "Correlation of Wake Measurements at Model and Full Scale Ship," Proc. 15th ONR Sym. on Naval Hydro., Hamburg, FRG, pp. 16-34.

Laudan, J., (1981), "The Influence of the Propeller on the Wake Distribution as Established in a Model Test," Proc. SNAME Propeller '81 Sym., Virginia Beach, USA, pp. 233-242.

Nagamatsu, T. and Sasajima, T., (1975), "Effect of Propeller Suction on Wake," Soc. Naval Arch. Japan, Vol. 137, pp. 58-63.

Nagamatsu, T. and Tokunaga, K., (1978), "Prediction of Effective Wake Distribution for Body of Revolution," J. Soc. Naval Arch. Japan, Vol. 143, pp. 93-100.

Nagamatsu, T., (1985), "Effect of Propeller on the Boundary Layer and Wake for Simple Three-Dimensional Forms," Proc. Osaka Int. Colloquium on Ship Viscous Flow, Osaka, Japan, pp. 450-467.

Neu, W., Mitra, P. and Schetz, J., (1988), "The Wake of Self-Propelled and Over-Thrusted Slender Bodies Near a Simulated Free Surface," J. Ship Research, Vol. 32, No. 1, pp. 70-79.

Patel, V.C., (1988), "Ship Stern and Wake Flows: Status of Experiment and Theory," Proc. 17th ONR Sym. on Naval Hydro., The Hague, The Netherlands.

Rood, E.P. and Anthony, D.G., (1988), "An Experimental Investigation of Propeller/Hull/Appendage Hydrodynamic Interactions," Proc. 17th ONR Sym. on Naval Hydro., The Hague, The Netherlands.

Sato, T. and Nagamatsu, T., (1986), "Calculation of Effective Wake Distribution of a Simple Hull Form," J. Soc. Naval Arch. Japan, Vol. 160, pp. 28-39.

Schetz, J.A. and Jakubowski, A.K., (1975), "Experimental Studies of the Turbulent Wake behind Self-Propelled Slender Bodies," AIAA Journal, Vol. 13, pp. 1568-1575.

Schetz, J.A. and Stottmeister, H.P., (1981), "The Flowfield Near the Propeller of a Self-Propelled Slender Body with Appendages," Proc. SNAME Propeller '81 Sym., Virginia Beach, USA, pp. 1-14.

Schetz, J.A., Lee, H. and Kong, F., (1983), "Measurements in the Near-Wake Region of a Slender, Self-Propelled Model at Pitch or Yaw," J. Ship Research, Vol. 27, No. 4, pp. 227-235.

Stern, F., Kim, H.T., Patel, V.C. and Chen, H.C., (1988a), "A Viscous-Flow Approach to the Computation of Propeller-Hull Interaction," J. Ship Research, Vol. 32, No. 4, to appear.

Stern, F., Kim, H.T., Patel, V.C. and Chen, H.C., (1988b), "Computation of Viscous Flow Around Propeller-Shaft Configurations," J. Ship Research, Vol. 32, No. 4, to appear.

Taniguchi, K. and Watanabe, K., (1969), "Unstable Phenomenon in the Self-Propulsion Test of Full Ship Form Models," Proc. 12th Int. Towing Tank Conf., pp. 252-256.

Tasaki, R. et al., (1987), "Twenty Years of Ship Research at IHI with the Ship Model Basin 1966-1987," Research Institute, Ishikawayama-Harima Heavy Industries Co., Ltd., Yokohama, Japan.

Toda, Y., (1984), "Distortion of Boundary Layer around a Ship Hull due to Propeller Suction," Doctoral Thesis, Dept. of Naval Arch., Osaka University (in Japanese).

Toda, Y., Tanaka, I. and Iwasaki, Y., (1982), "Distortion of Axisymmetric Boundary Layer Due to Propeller Suction," J. Kansai Soc. Naval Arch. Japan, Vol. 185, pp. 39-48 (in Japanese).

Toda, Y., Tanaka, I., Sugioka, H. and Mori, H., (1984), "Distortion of Three-Dimensional Boundary Layer due to Propeller Suction," J. Kansai Soc. Naval Arch. Japan, Vol. 192, pp. 69-79 (in Japanese).

Toda, Y., Kasahara, Y. and Tanaka, I., (1987), "A Simple Prediction Method for Effective Wake Distribution," J. Kansai Soc. Naval Arch. Japan, Vol. 204 (in Japanese). English translation is reproduced here as Appendix I.

Todd, F.H., (1963), "Series 60 Methodical Experiments with Models of Single-Screw Merchant Ships," David Taylor Model Basin Report 1712.

Todd, F.H., (1967), "Resistance and Propulsion," Principles of Naval Architecture, Comstock, J.P., ed., SNAME, Pavonia, NJ, Chap. VII.

Tsuchida, K., Yazaki, A. and Takahashi, M., (1958), "Open Water Tests Series With Modern Five-Bladed Propeller Models," J. Soc. Naval Arch. Japan, Vol. 102, pp. 77-81.

Yamazaki, R. and Nakatake, K., (1984), "Free-Surface Effect on the Hull-Propeller Interaction," Proc. 15th ONR Sym. on Naval Hydro., Hamburg, FRG, pp. 32-45.

Table 1  
Principal dimensions of ship model and propeller

<u>model</u>		<u>propeller</u>	
Length	4.0m	Diameter ( $= 2R_p$ )	145.64mm
Breadth	0.5333m	Pitch ratio (constant pitch)	1.0310
Draft	0.2133m	Boss ratio	0.2
$C_B$	0.6	Number of blades	5
$C_m$	.977	Direction of turning	right
$m = (A_m/A_T)$	.0033	Expanded area ratio	0.7451
$z_o$ (shaft center)	129.05mm	Projected area ratio	0.6249
Wetted surface area	2.7189m <sup>2</sup>	Thickness ratio at $0.7R_p$	3.992%
		Thickness distribution	$n = 25$
		Blade section	MAU
		Rake	6°

Table 2  
Measurement locations for the with- and without-propeller  
conditions (port and starboard)

	x	x/ $R_p$	Surface- Pressure Distribution	Mean- Velocity and Pressure Field	WT °C	Re $\times 10^{-6}$
	.5	-26.79		w/o	19.5	3.94
	.6	-21.29		w/o	19.5	3.94
	.7	-15.8		w/o	19.5	3.94
	.8	-10.3	w,w/o	w/o	10.6	3.11
	.85	-7.55	w,w/o			
	.9	-4.81	w,w/o	w,w/o	10.2	3.08
	.925	-3.43	w,w/o			
	.95	-2.06	w,w/o	w,w/o	8.0	2.89
	.9625	-1.37	w,w/o			
	.975	-.69	w,w/o	w,w/o	11.6	3.20
	.981	-.36	w,w/o			
	.98125	-.34		w,w/o	8.0	2.89
Propeller-Plane	.9875	.0	w,w/o	w/o	3.0	2.89
	1.	.69		w,w/o	16.0	3.60
	1.01875	1.72		w,w/o	10.7	3.12
	1.05	3.43		w,w/o	15.4	3.55
	1.1	6.18		w,w/o	14.9	3.50

Resistance test (11.6°C)

Self-propulsion test (11.7°C)

Propeller-open water test (11.5°C)

Surface-Pressure Distribution (10.2°C,  $Re = 3.08 \times 10^6$ )

Table 3  
Series 60 C<sub>B</sub> = .6 offsets\*

Length Beam Depth	121.92 m 16.256 m 9.758 m	Draft Bilge Radius Shaft Center			Stern Tube Diameter										.950 m			
		6.502 m 2.353 m 3.933 m			6.502 m 2.353 m 3.933 m			6.502 m 2.353 m 3.933 m			6.502 m 2.353 m 3.933 m			6.502 m 2.353 m 3.933 m			6.502 m 2.353 m 3.933 m	
-----Waterlines-----																		
Sta.	Tan	.122	.244	.488	.732	.976	1.3	1.626	2.438	3.251	4.064	4.877	5.69	6.502 (DWL)	7.315	8.128	8.94	9.758
10.(FP)																		
9.75	.052	.115	.155	.219	.256	.277	.302	.318	.337	.342	.346	.351	.366	.415	.082	.162	.250	.341
9.5	.076	.214	.303	.444	.533	.588	.636	.660	.692	.707	.720	.732	.768	.829	.495	.610	.768	.976
9.25	.110	.334	.467	.675	.808	.896	.973	1.018	1.094	1.140	1.167	1.189	1.228	1.298	.930	1.082	1.298	1.609
9.	.137	.430	.624	.900	1.085	1.216	1.339	1.423	1.573	1.658	1.701	1.731	1.777	1.853	1.990	2.195	2.502	2.926
8.5	.317	.735	1.018	1.428	1.722	1.950	2.187	2.353	2.661	2.825	2.923	2.990	3.066	3.179	3.341	3.575	3.883	4.289
8.	.759	1.386	1.754	2.268	2.640	2.934	3.253	3.490	3.871	4.081	4.228	4.343	4.455	4.569	4.724	4.935	5.190	5.532
7.5	1.588	2.513	2.858	3.359	3.761	4.103	4.452	4.715	5.139	5.364	5.514	5.617	5.721	5.837	5.968	6.130	6.322	6.525
7.	2.707	3.707	4.060	4.542	4.939	5.273	5.612	5.867	6.288	6.520	6.635	6.703	6.764	6.832	6.910	7.007	7.114	7.227
6.5	3.844	4.836	5.167	5.608	5.975	6.285	6.590	6.816	7.197	7.364	7.422	7.452	7.483	7.516	7.556	7.596	7.638	7.690
6.	4.795	5.692	5.999	6.456	6.776	7.026	7.294	7.486	7.766	7.891	7.934	7.940	7.946	7.952	7.961	7.967	7.980	7.983
5.5	5.453	6.281	6.572	6.972	7.271	7.487	7.698	7.865	8.081	8.127	8.128	8.128	8.128	8.128	8.128	8.128	8.128	8.128
5.25	5.674	6.457	6.750	7.140	7.422	7.628	7.826	7.972	8.128	8.128	8.128	8.128	8.128	8.128	8.128	8.128	8.128	8.128
5.	5.770		6.818	7.210	7.481	7.683		8.013	8.128	8.128	8.128	8.128	8.128	8.128	8.128	8.128	8.128	8.128
4.5	5.569		6.684	7.077	7.359	7.574		7.928	8.099	8.128	8.128	8.128	8.128	8.128	8.128	8.128	8.128	8.128
4.	5.090		6.237	6.648	6.965	7.221		7.672	7.955	8.080	8.123	8.128	8.128	8.128	8.128	8.128	8.128	8.128
3.5	4.426		5.544	5.956	6.285	6.570		7.125	7.548	7.800	7.935	8.010	8.062	8.086	8.101	8.105	8.117	8.126
3.	3.587		4.622	5.054	5.385	5.657		6.251	6.800	7.184	7.455	7.666	7.815	7.925	7.998	8.047	8.086	8.120
2.5	2.673		3.608	4.022	4.319	4.560		5.115	5.654	6.130	6.565	6.965	7.324	7.605	7.809	7.940	8.019	8.080
2.	1.783		2.603	2.963	3.218	3.428		3.868	4.340	4.813	5.340	5.913	6.477	6.956	7.321	7.583	7.775	7.925
1.5	.969		1.602	1.914	2.135	2.307		2.643	2.993	3.356	3.816	4.410	5.151	5.870	6.410	6.846	7.209	7.510
1.	.375		0.877	1.094	1.238	1.356		1.554	1.737	1.917	2.176	2.615	3.389	4.356	5.123	5.767	6.309	6.779
.75	.183		0.559	0.732	0.846	0.930		1.067	1.173	1.265	1.408	1.734	2.432	3.445	4.343	5.093	5.724	6.251
.5	.079		.294	.418	.498	.549		.615	.655	.683	.735	.942	1.512	2.493	3.480	4.322	5.023	5.575
.375	.065		.184	.263	.316	.353		.391	.415	.427	.458	.600	1.083	2.022	3.010	3.888	4.607	5.189
.25	.058		.090	.116	.135	.149		.162	.171	.176	.189	.268	.680	1.360	2.514	3.399	4.118	4.706
.125												.305		1.108	2.514	3.399	4.118	4.706
0.(AP)													.305		1.108	2.514	3.399	4.118
-.062													.305		1.108	2.514	3.399	4.118
-.125													.305		1.108	2.514	3.399	4.118
-.187													.305		1.108	2.514	3.399	4.118
-.25													.305		1.108	2.514	3.399	4.118

\*Offsets are in meters for full scale



Table 4  
Propeller offsets

Propeller geometry

	r/R	0.2	0.3	0.4	0.5	0.6	0.66	0.7	0.8	0.9	1.0
Chord Length $C_{0.66}$ x 100 (Chord length at .66R $C_{0.66} = 0.3460$ )	From Generator Line to Trailing Edge	27.95	33.45	38.76	43.54	47.96	49.74	51.33	52.39	48.49	17.29
	From Generator Line to Leading Edge	38.58	44.25	48.32	50.80	51.15	50.26	48.31	40.53	25.13	-
	Chord Length	66.54	77.70	87.08	94.34	99.11	100.00	99.64	92.92	73.62	-
Max. Thickness Diameter x 100		4.06	3.59	3.12	2.65	2.18	1.90	1.71	1.24	0.77	0.30 B.T.F. = 0.050
Maximum thickness Position from L.E.		32.0	32.0	32.0	32.5	34.9	37.9	40.2	45.4	48.9	-

Wing section offsets

X: distance from L.E. (% of chord)

r: % of maximum thickness;  $Y_u$  = upper surface;  $y_l$  = lower surface

0.20	X	0	2.00	4.00	6.00	10.00	15.00	20.00	30.00	32.00	40.00	50.00	60.00	70.00	80.00	90.00	95.00	100.00
	$Y_u$	35.00	51.85	59.75	66.15	76.05	85.25	92.20	99.80	100.00	97.75	89.95	78.15	63.15	45.25	25.30	15.00	4.50
	$Y_l$		24.25	19.05	15.00	10.00	5.40	2.35										
0.30	X	0	2.00	4.00	6.00	10.00	15.00	20.00	30.00	32.00	40.00	50.00	60.00	70.00	80.00	90.00	95.00	100.00
	$Y_u$	35.00	51.85	59.75	66.15	76.05	85.25	92.20	99.80	100.00	97.75	89.95	78.15	63.15	45.25	25.30	15.00	4.50
	$Y_l$		24.25	19.05	15.00	10.00	5.40	2.35										
0.40	X	0	2.00	4.00	6.00	10.00	15.00	20.00	30.00	32.00	40.00	50.00	60.00	70.00	80.00	90.00	95.00	100.00
	$Y_u$	35.00	51.85	59.75	66.15	76.05	85.25	92.20	99.80	100.00	97.75	89.95	78.15	63.15	45.25	25.30	15.00	4.50
	$Y_l$		24.25	19.05	15.00	10.00	5.40	2.35										
0.50	X	0	2.03	4.06	6.09	10.16	15.23	20.31	30.47	32.50	40.44	50.37	60.29	70.22	80.15	90.07	95.04	100.00
	$Y_u$	35.00	51.85	59.75	66.15	76.05	85.25	92.20	99.80	100.00	97.75	89.95	78.15	63.15	45.25	25.30	15.00	4.50
	$Y_l$		24.25	19.05	15.00	10.00	5.40	2.35										
0.60	X	0	2.18	4.36	6.54	10.91	16.36	21.81	32.72	34.90	42.56	52.13	61.70	71.28	80.85	90.43	95.21	100.00
	$Y_u$	34.00	49.60	58.00	64.75	75.20	84.80	91.80	99.80	100.00	97.75	89.95	78.15	63.15	45.25	25.30	15.00	4.50
	$Y_l$		23.60	18.10	14.25	9.45	5.00	2.25										
0.70	X	0	2.51	5.03	7.54	12.56	18.84	25.12	37.69	34.20	47.23	56.03	64.82	73.62	82.41	91.21	95.60	100.00
	$Y_u$	30.00	42.90	52.20	59.90	71.65	82.35	90.60	99.80	100.00	97.75	89.95	78.15	63.15	45.25	25.30	15.00	4.50
	$Y_l$		20.50	15.45	11.95	7.70	4.10	1.75										
0.80	X	0	2.51	5.68	8.51	14.19	21.28	28.38	42.56	45.40	51.82	59.85	67.89	75.91	83.94	91.97	95.99	100.00
	$Y_u$	21.00	32.45	41.70	50.10	64.60	78.45	88.90	99.80	100.00	97.75	89.95	78.15	63.15	45.25	25.30	15.00	4.50
	$Y_l$		14.00	10.45	8.05	5.05	2.70	1.15										
0.90	X	0	3.06	6.11	9.17	15.28	22.92	30.56	45.85	48.90	54.91	62.42	69.94	77.46	84.97	92.49	96.24	100.00
	$Y_u$	8.30	21.10	31.50	40.90	57.45	74.70	87.45	99.70	100.00	98.65	92.75	83.00	69.35	51.85	30.80	19.40	6.85
	$Y_l$		4.00	2.70	2.05	1.20	0.70	0.30										
0.95	X	0	3.13	6.25	9.38	15.63	23.44	31.25	46.87	50.00	55.88	63.23	70.59	77.94	85.30	92.65	96.32	100.00
	$Y_u$	6.00	19.65	30.00	39.60	56.75	74.30	87.30	99.65	100.00	99.00	93.85	84.65	71.65	54.30	33.50	21.50	8.00
	$Y_l$																	

Table 5  
Steady and unsteady first blade harmonic propeller  
forces and moments

		<u>steady</u>		
		nominal inflow	effective inflow	experiment
Forces	Thrust ( $K_T$ )	.265	.233	.234
	Horizontal (+ port)	.00244	.00403	
	Vertical (+ upward)	.00982	.00962	
Moments	Torque ( $K_Q$ )	.0444	.0403	.0411
	Horizontal (+ port)	.00793	.00886	
	Vertical (+ upward)	.00673	.00657	

		<u>unsteady first blade harmonic</u>	
		nominal inflow	effective inflow
Forces	Thrust	.00665	.00670
	Horizontal (+ port)	.00858	.00837
	Vertical (+ upward)	.00440	.00463
Moments	Torque	.00080	.00090
	Horizontal (+ port)	.00771	.00693
	Vertical (+ upward)	.00205	.00214

Forces are nondimensionalized using  $\rho n^2 D_p^4$

Moments are nondimensionalized using  $\rho n^2 D_p^5$



(a)



(b)

Figure 1. Series 60  $C_B = .6$  4m models; (a) wood; and  
(b) fibre-reinforced-plexiglass with  
pressure taps.

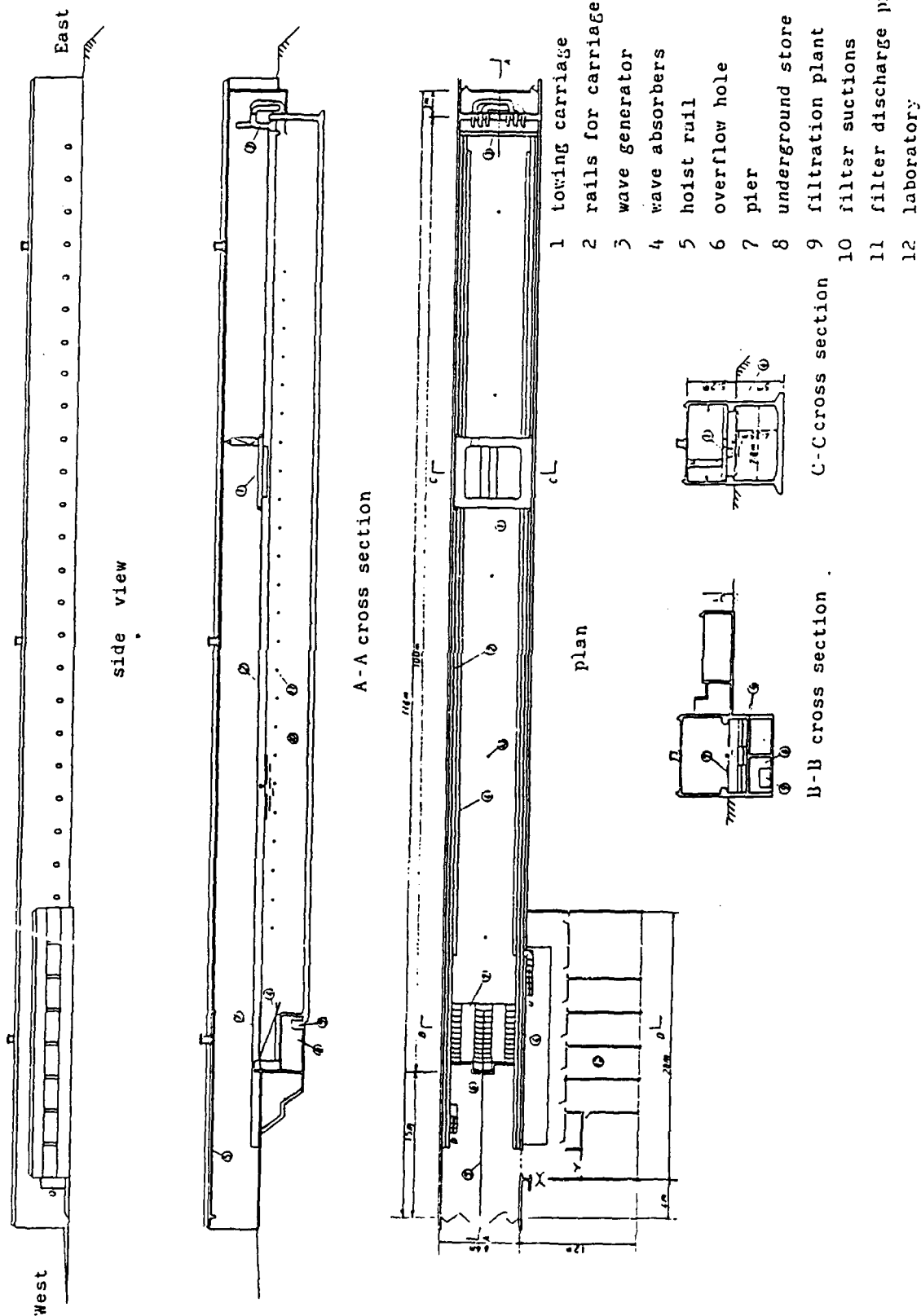
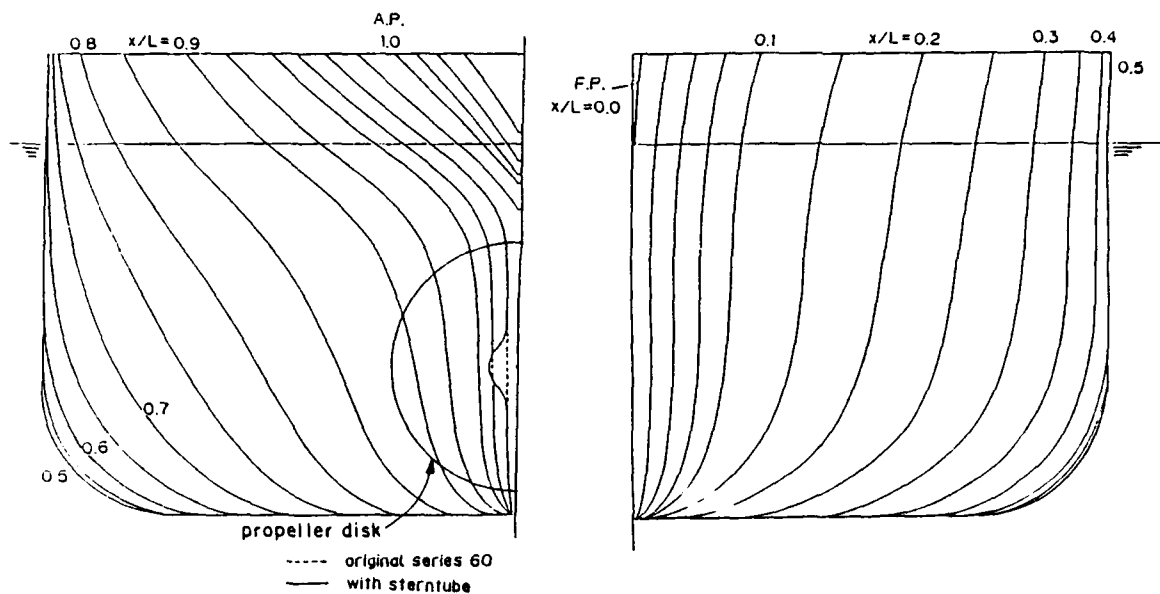
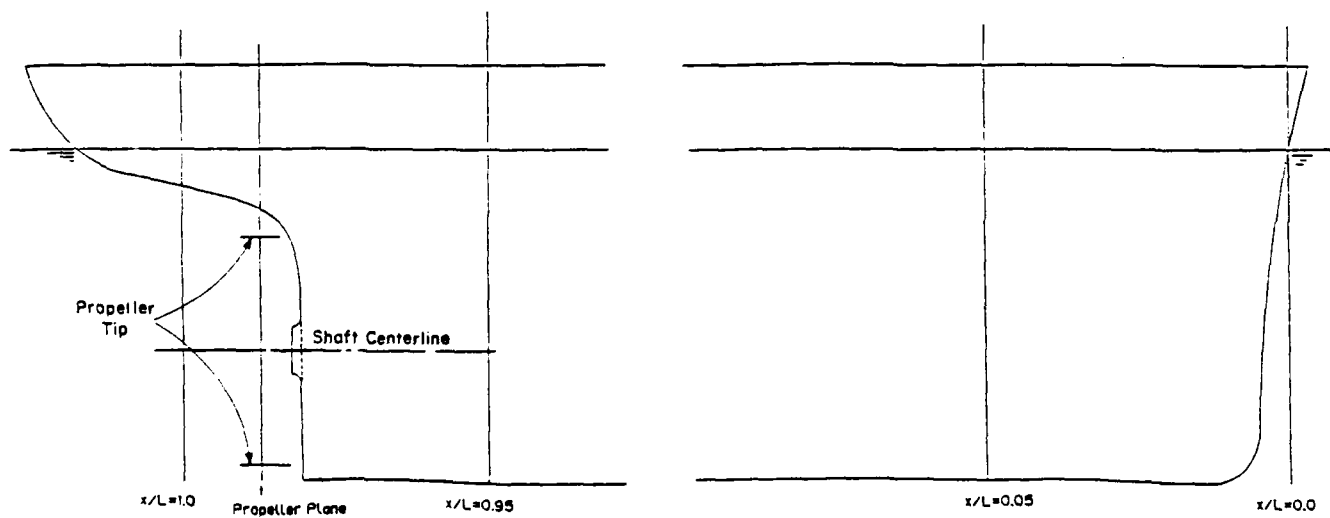


Figure 2. Osaka University, Department of Naval Architecture, towing tank.

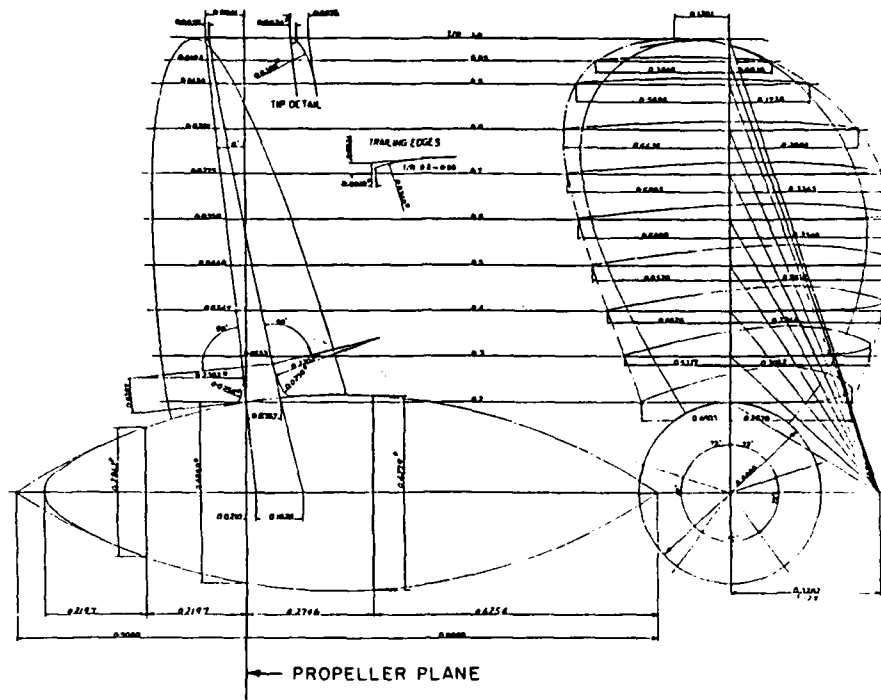


(a) body plan (transverse sections)

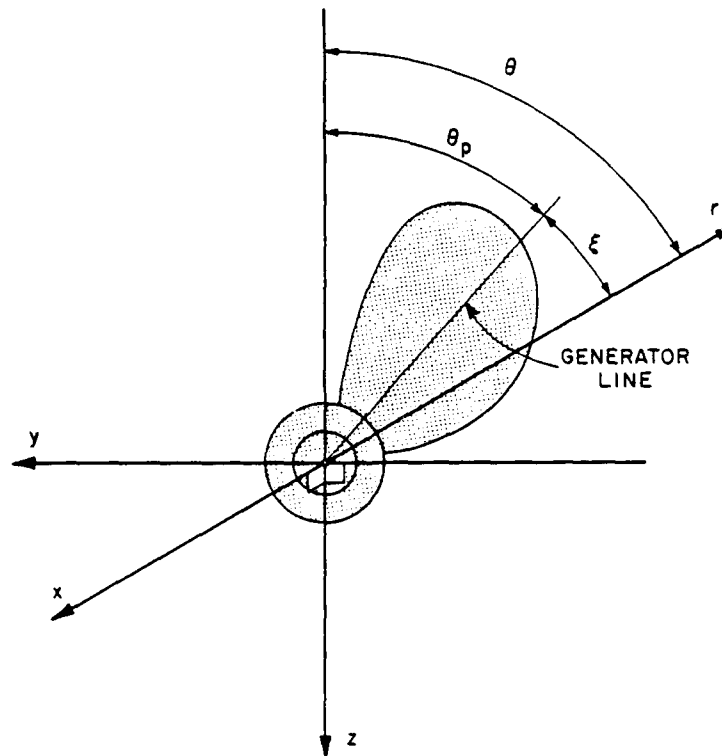


(b) profile plan (longitudinal section through centerplane)

Figure 3. Series 60  $C_B = .6$  lines drawing.

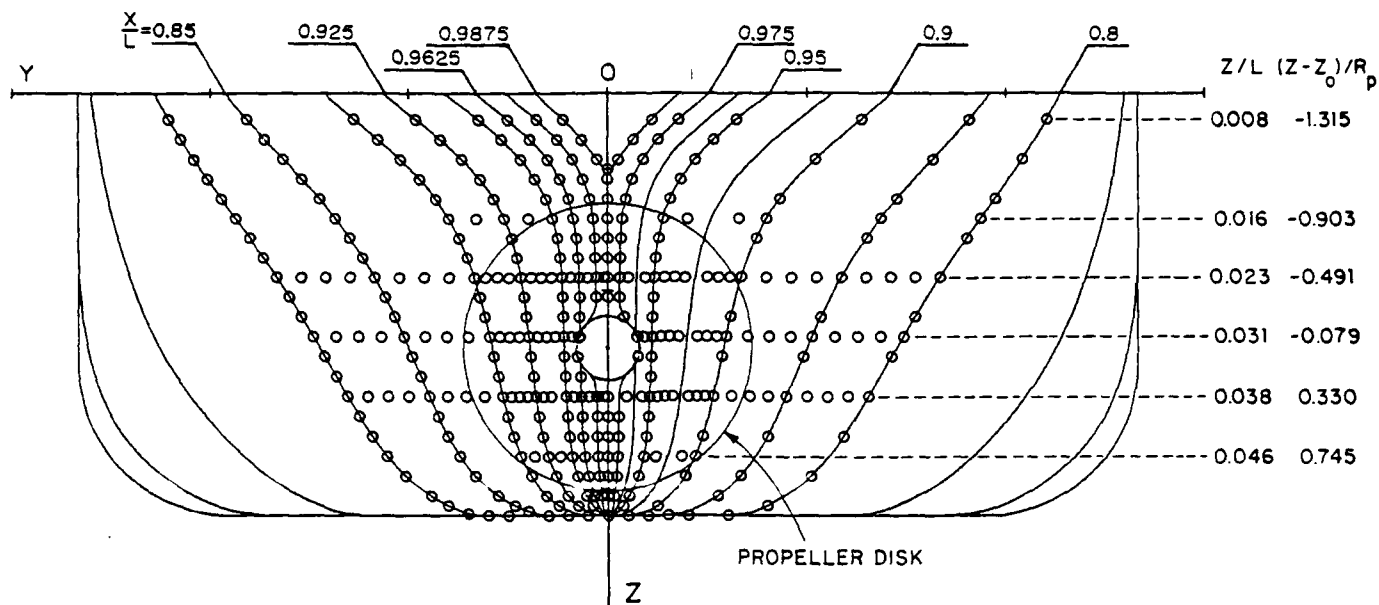


(a) drawing

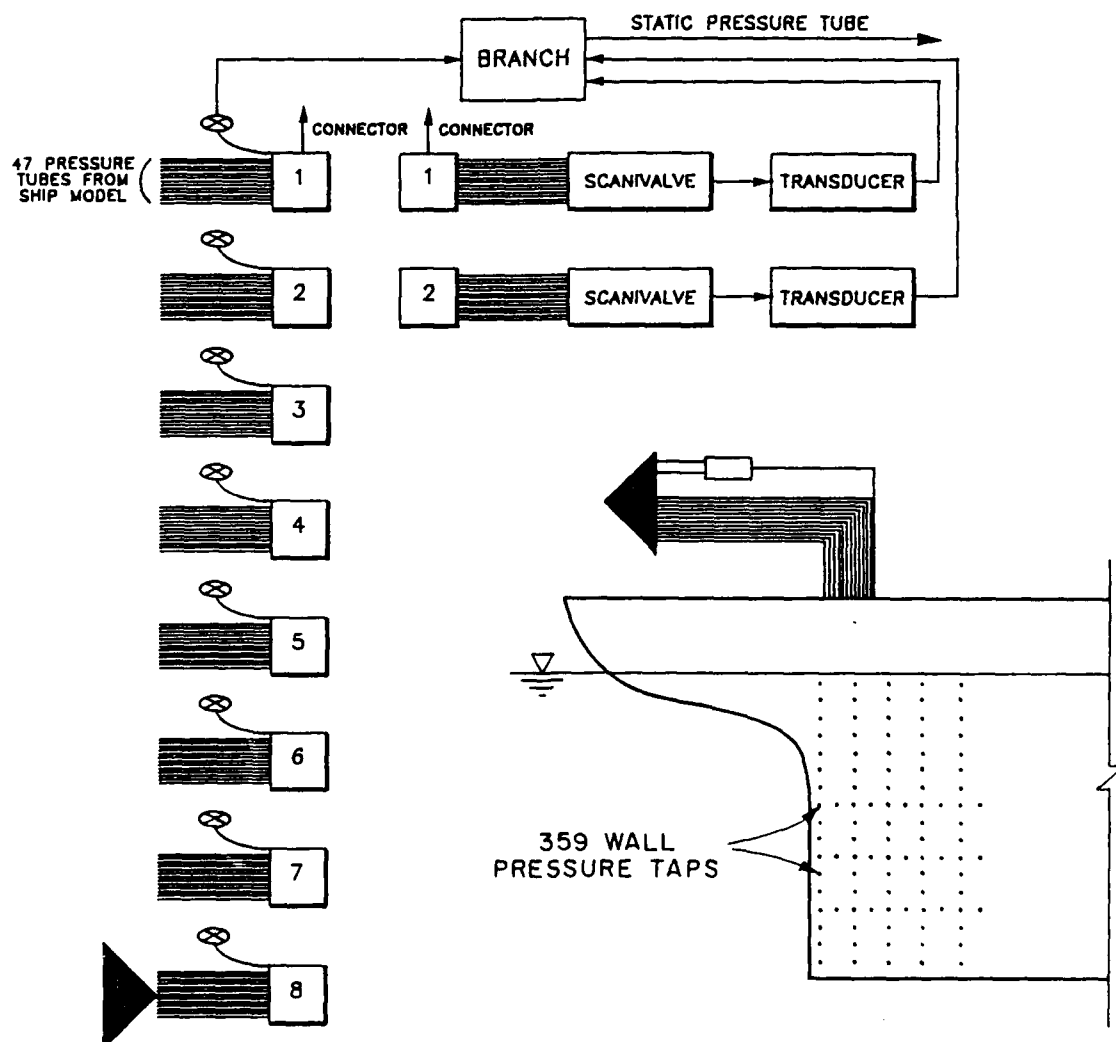


(b) coordinate system

Figure 4. Propeller drawing and coordinate system.



(a) pressure-tap locations



(b) block diagram

Figure 5. Pressure-tap locations and block diagram for surface-pressure measurements.

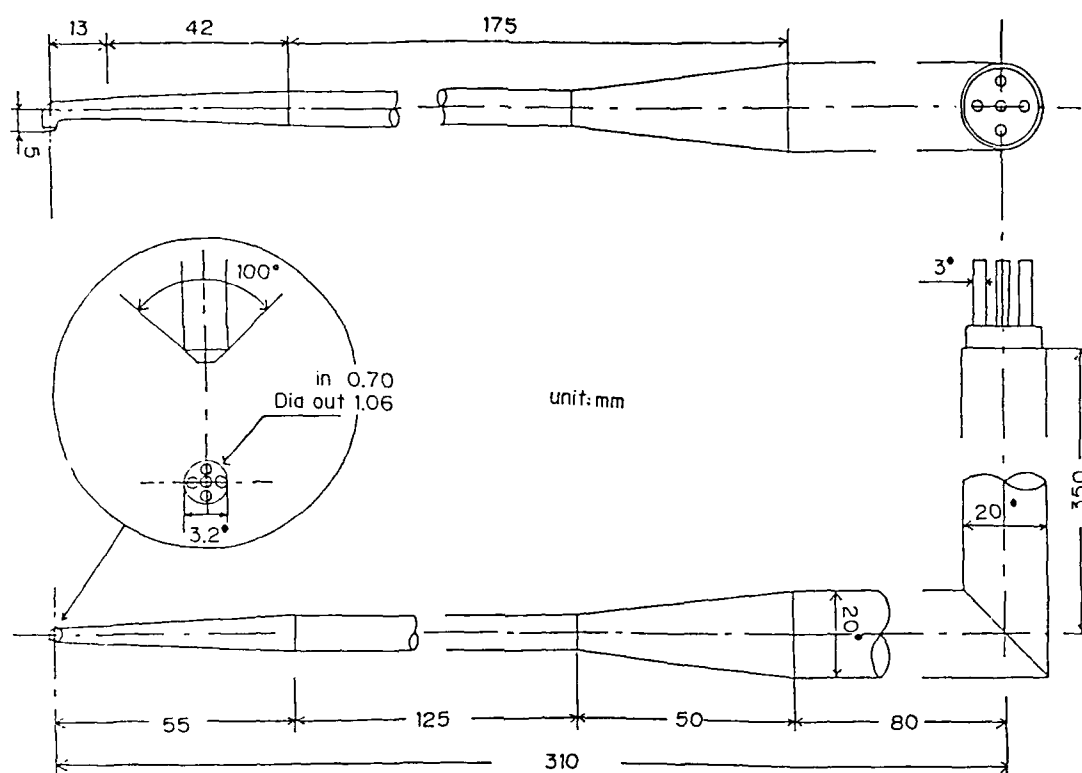


Figure 6. Five-hole pitot probe: starboard side.

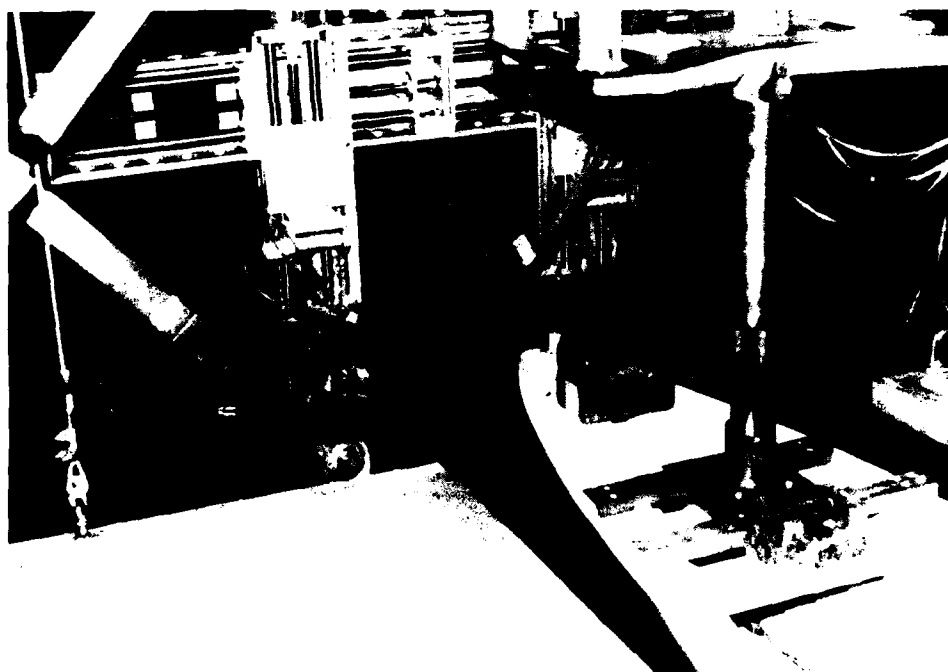
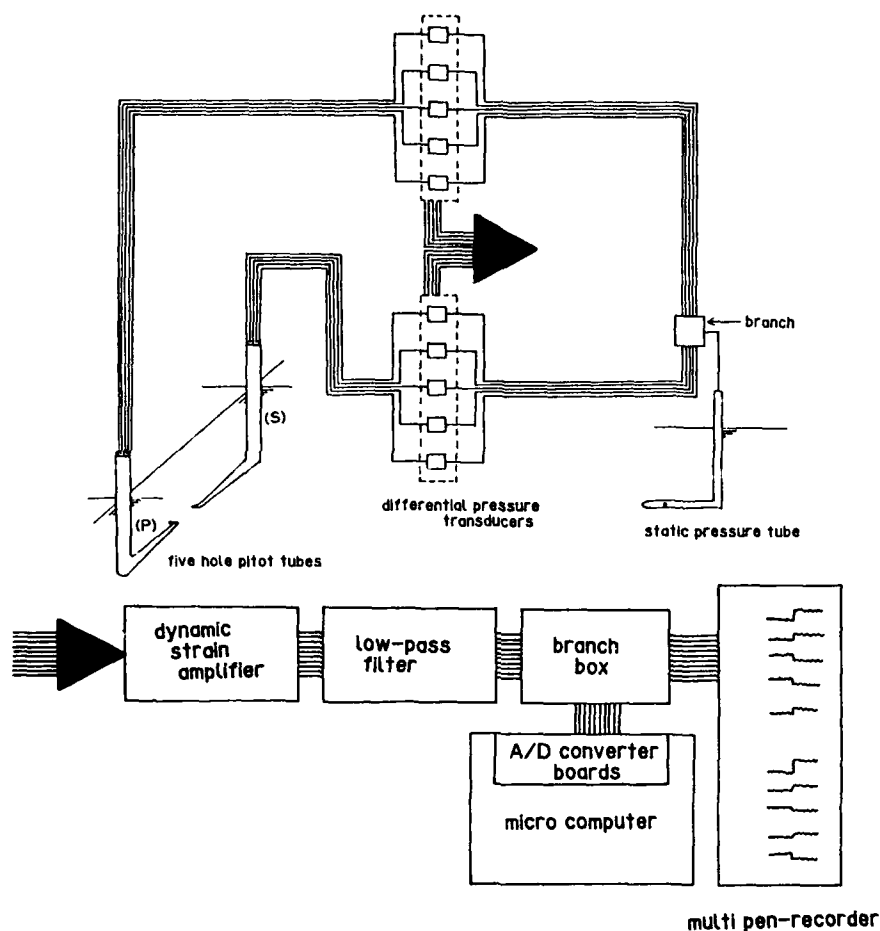
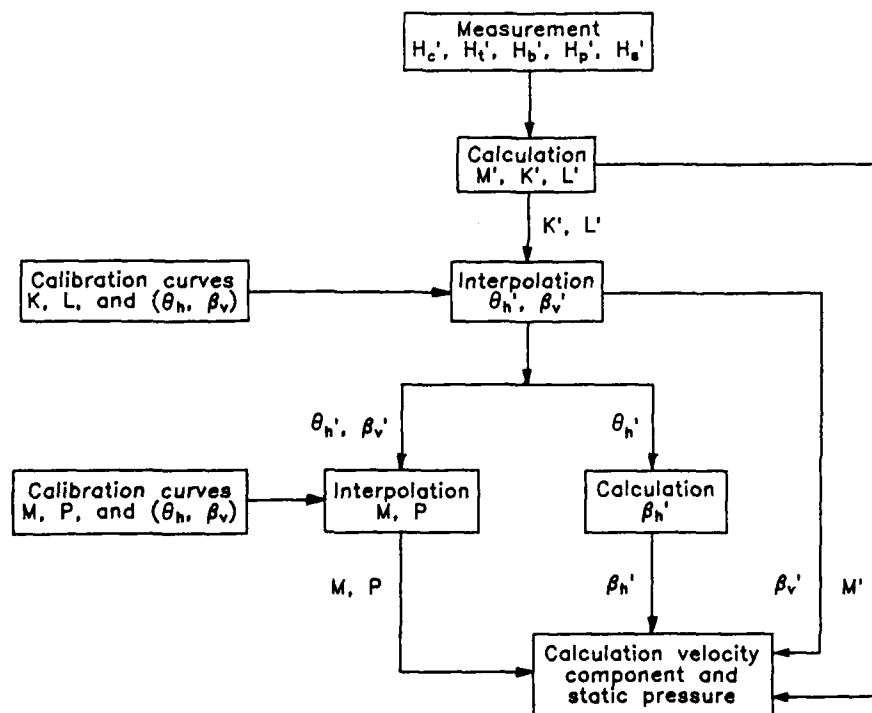


Figure 7. Automated traverse.





(a) data acquisition



(b) probe calibration

Figure 8. Block diagrams for mean-velocity and pressure field measurements.

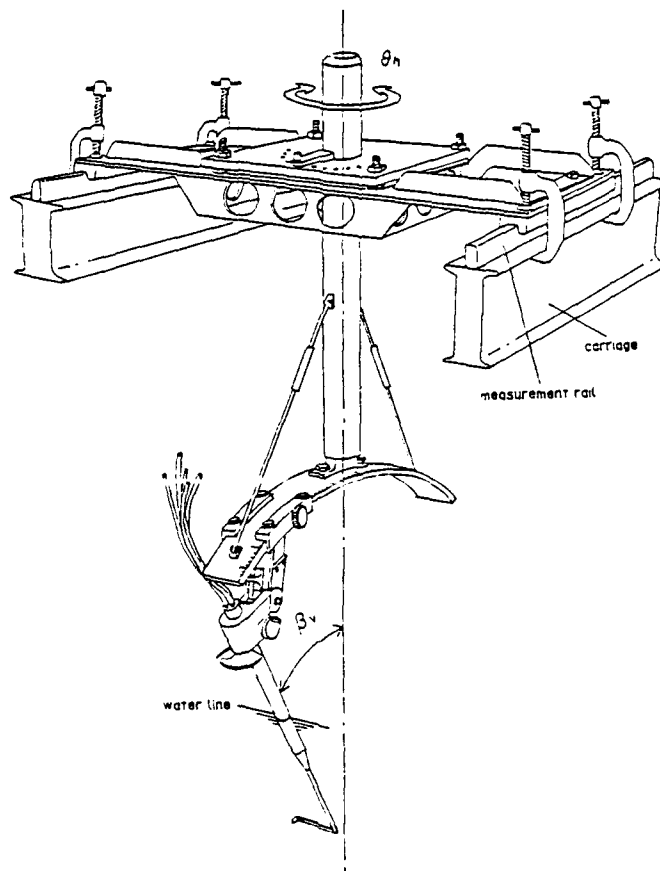


Figure 9. Calibration device.

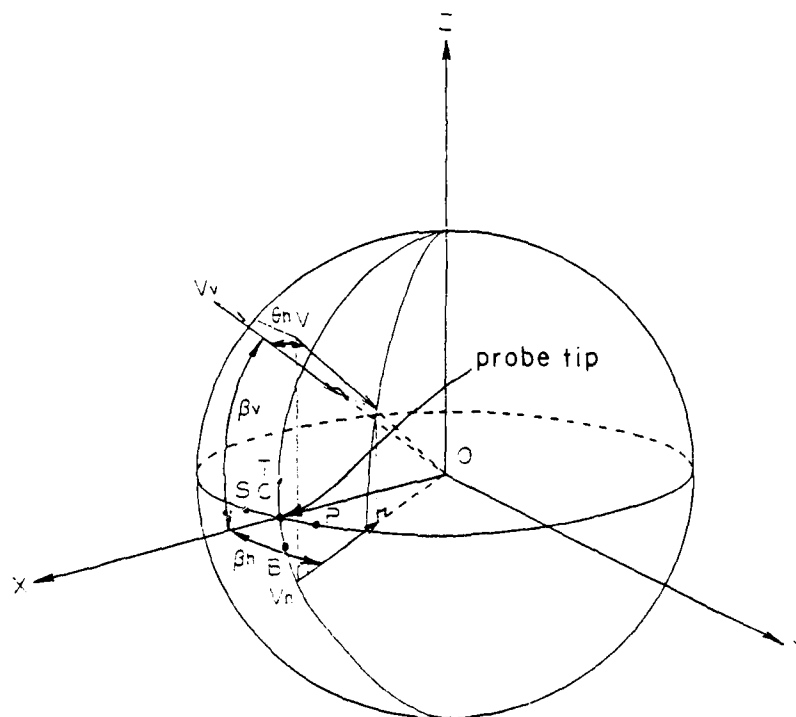
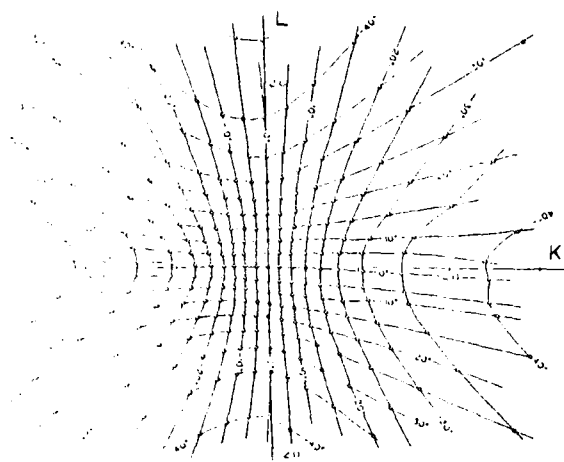
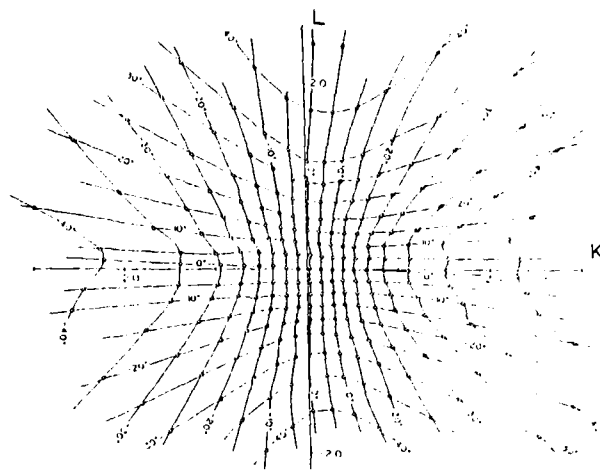


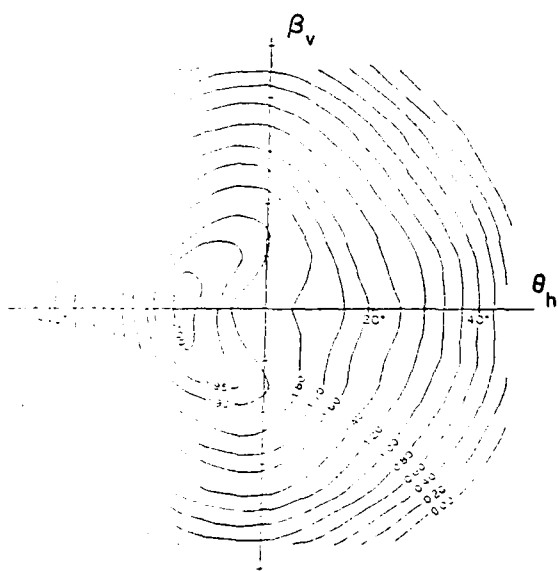
Figure 10. Five-hole pitot probe coordinate system.



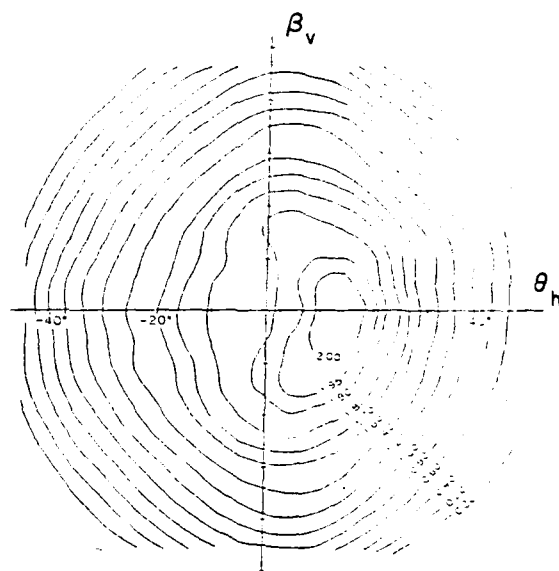
(a)



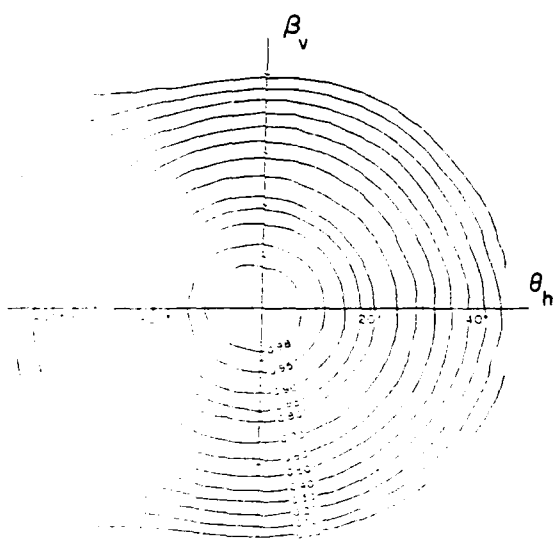
(b)



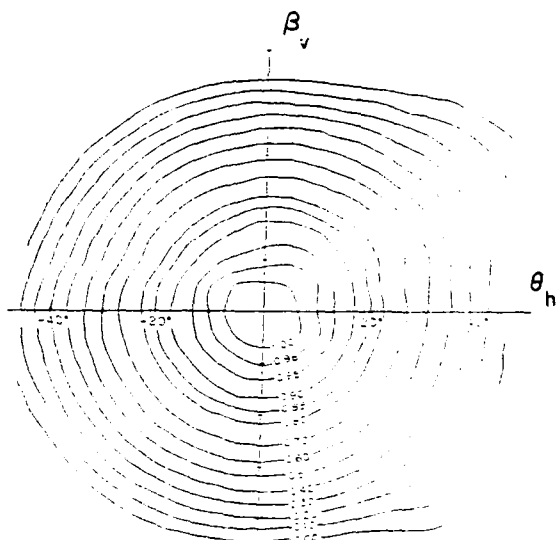
(c)



(d)



(e)



(f)

Figure 11. Calibration coefficients: (a) starboard L vs. K; (b) port L vs. K; (c) port M; (d) starboard M; (e) port P; and (f) starboard P.

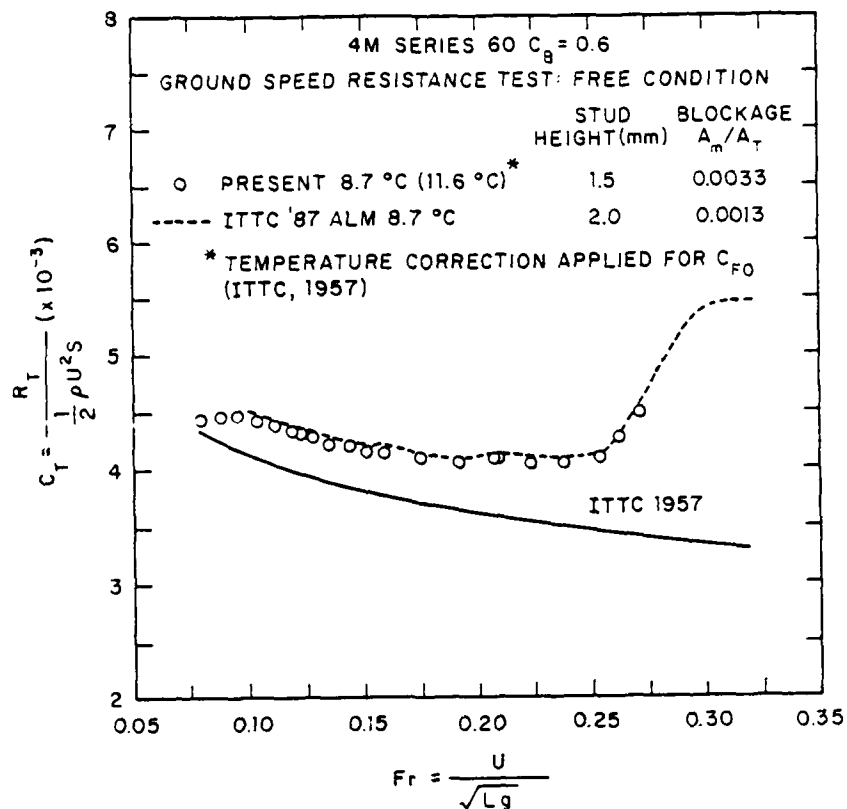


Figure 12. Total-resistance coefficient.

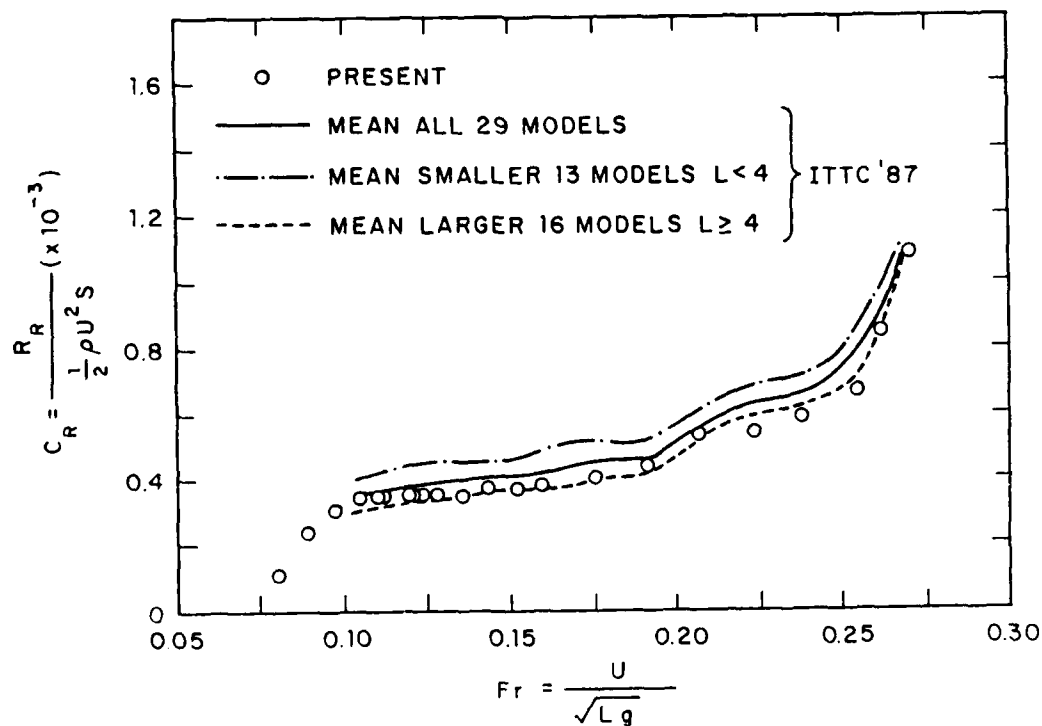


Figure 13. Residuary-resistance coefficient.

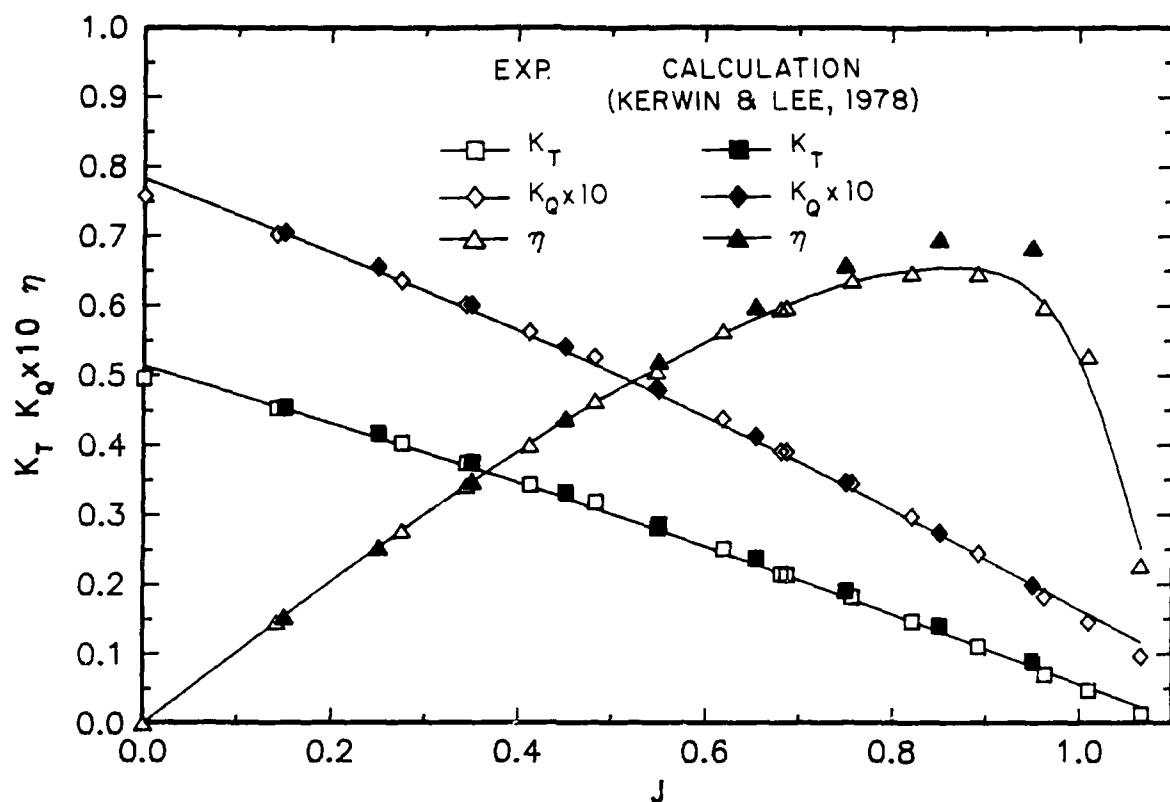


Figure 14. Propeller open-water curves.

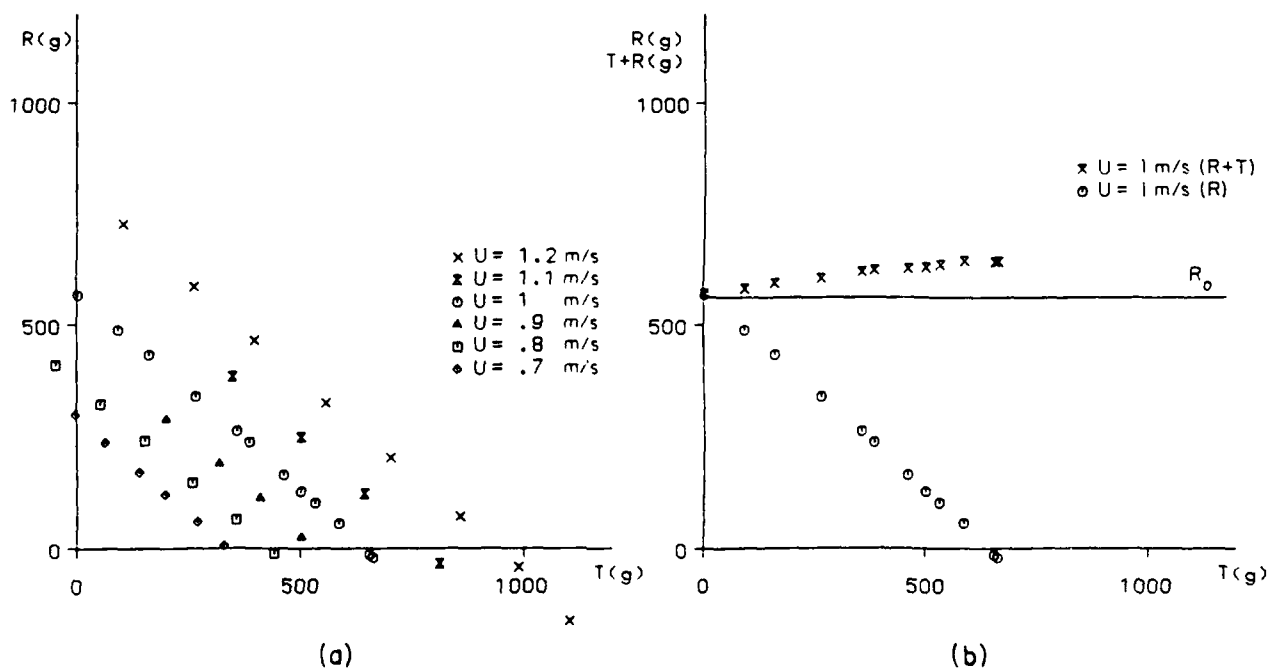


Figure 15. Self-propulsion test results: (a) load-varying test for all speeds; and (b) load-varying test for the detailed-measurement condition.

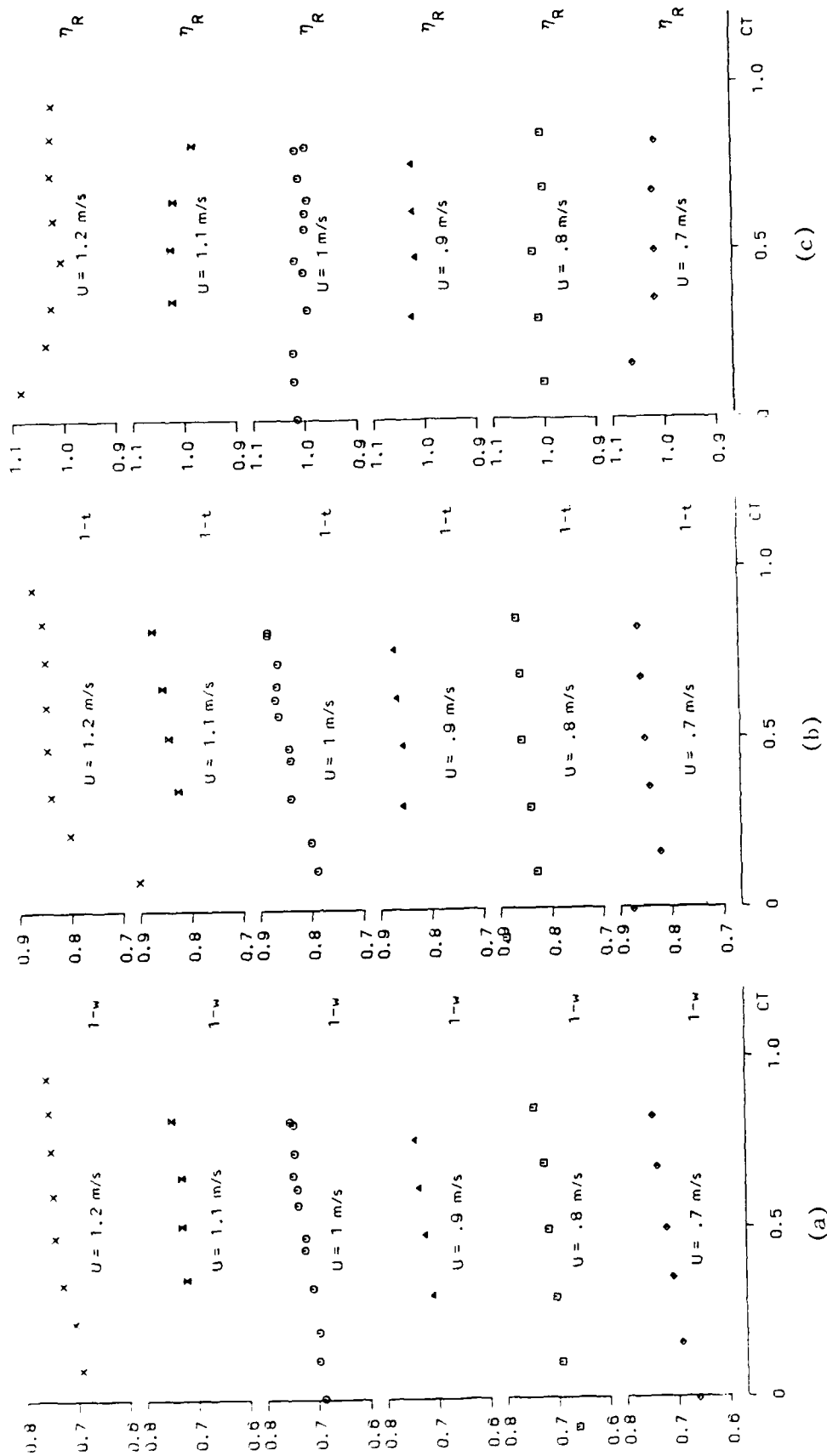


Figure 16. Self-propulsion factors: (a) wake fraction ( $1-w$ ); (b) thrust deduction ( $1-t$ ); and (c) relative rotative efficiency ( $\eta_R$ ).

# SERIES 60 WAVE PROFILES

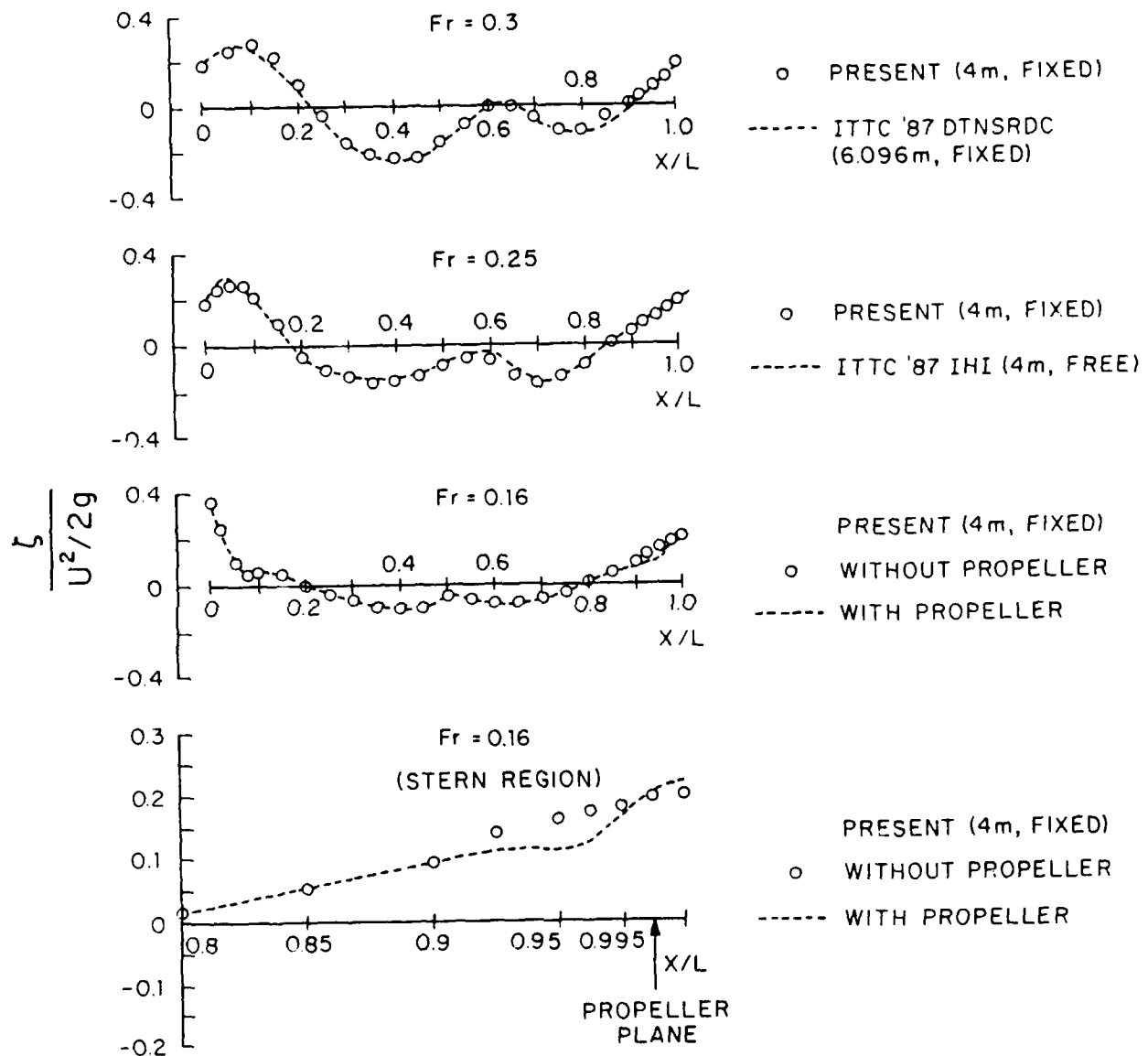


Figure 17. Wave profiles.

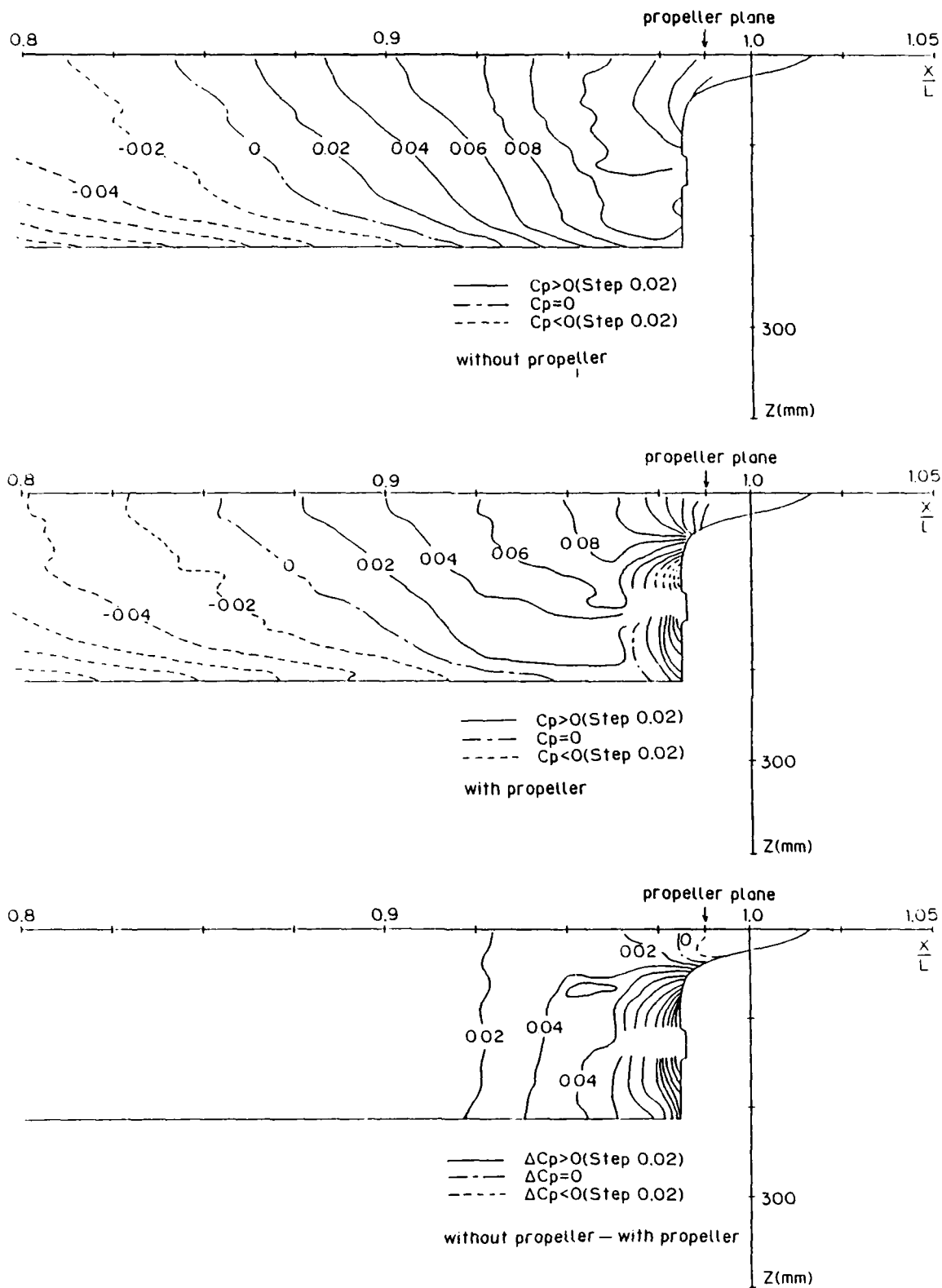


Figure 18. Surface-pressure distribution: pressure contours.



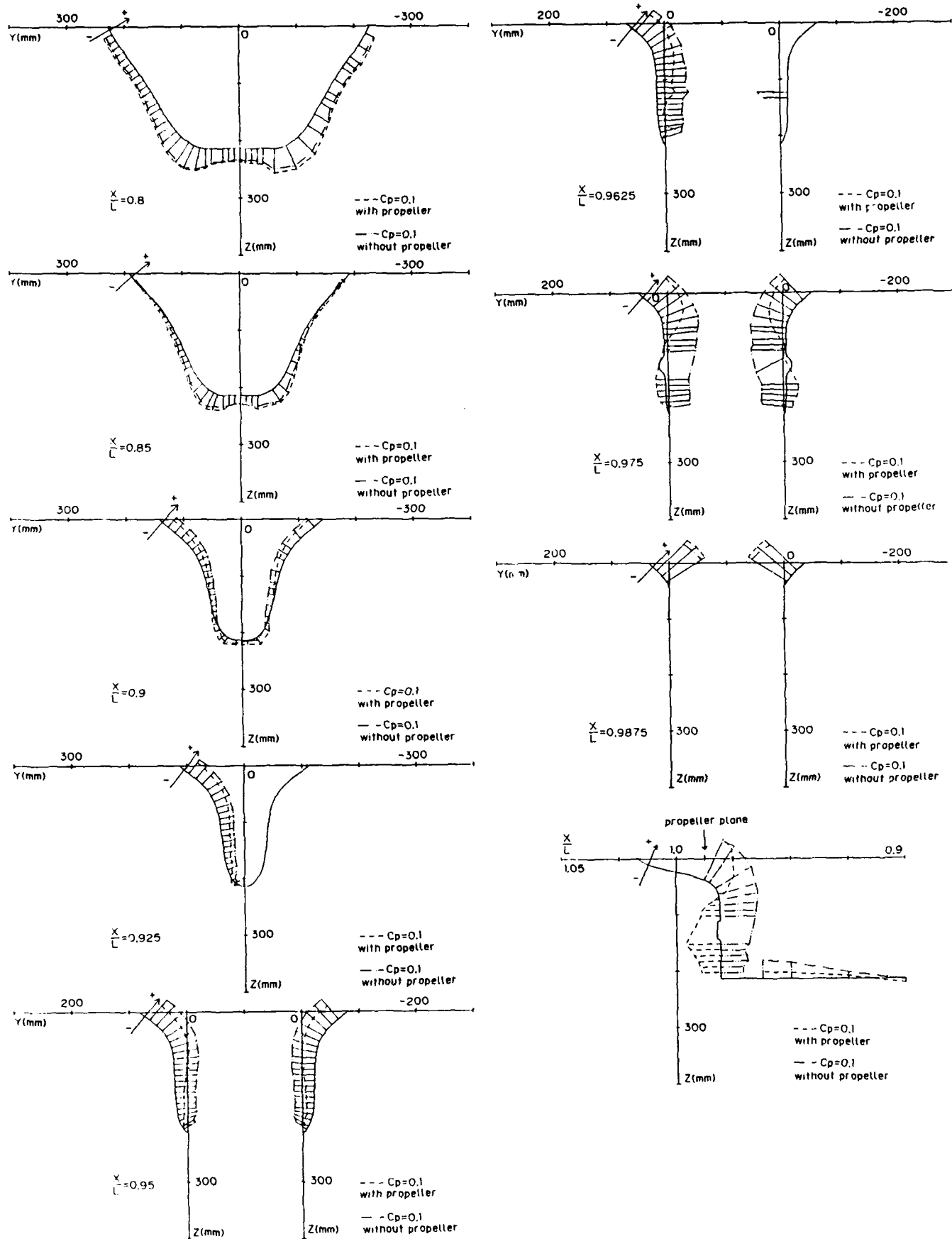


Figure 19. Surface-pressure distribution: girthwise variation.

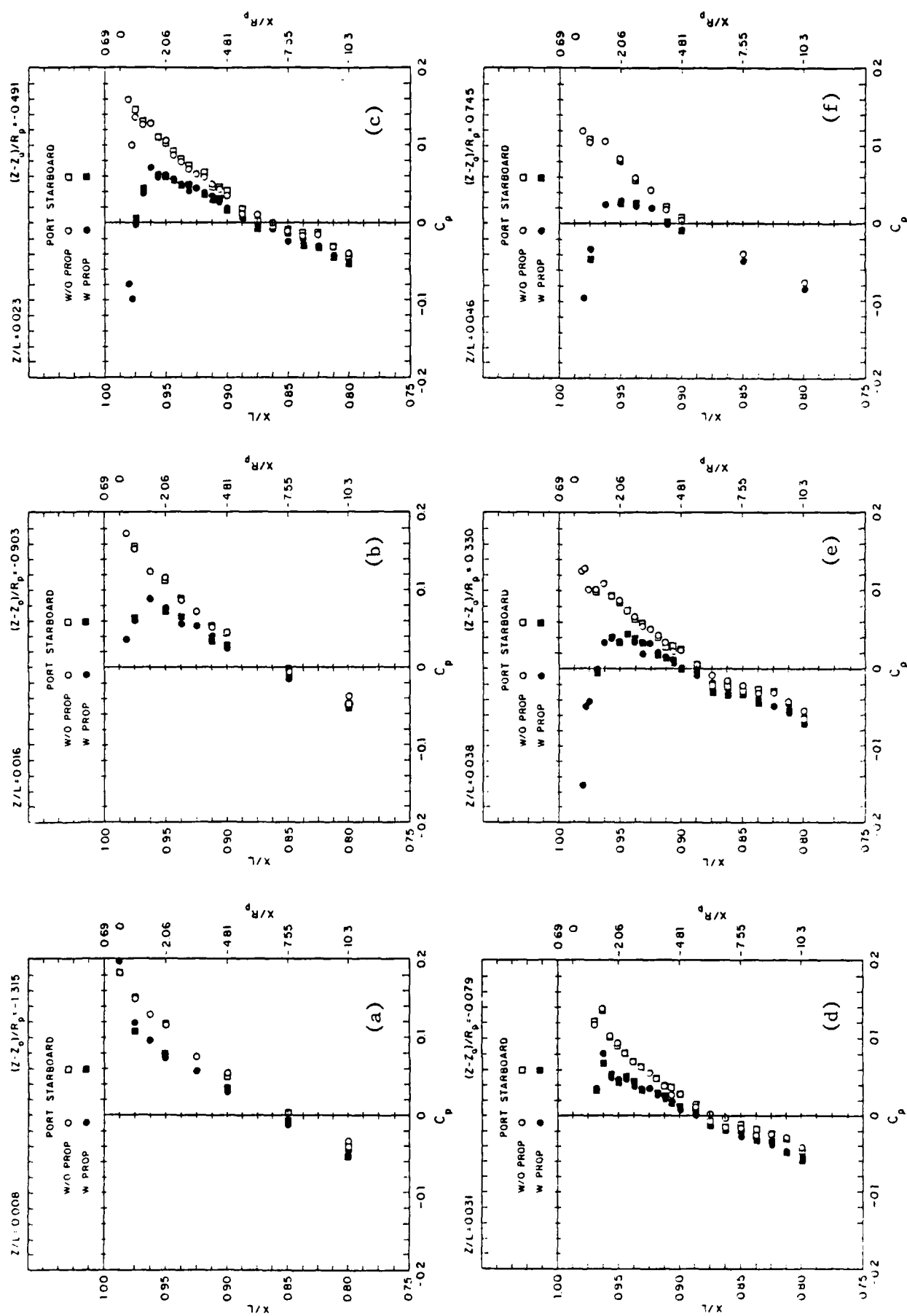


Figure 20. Surface-pressure distribution: streamwise variation.

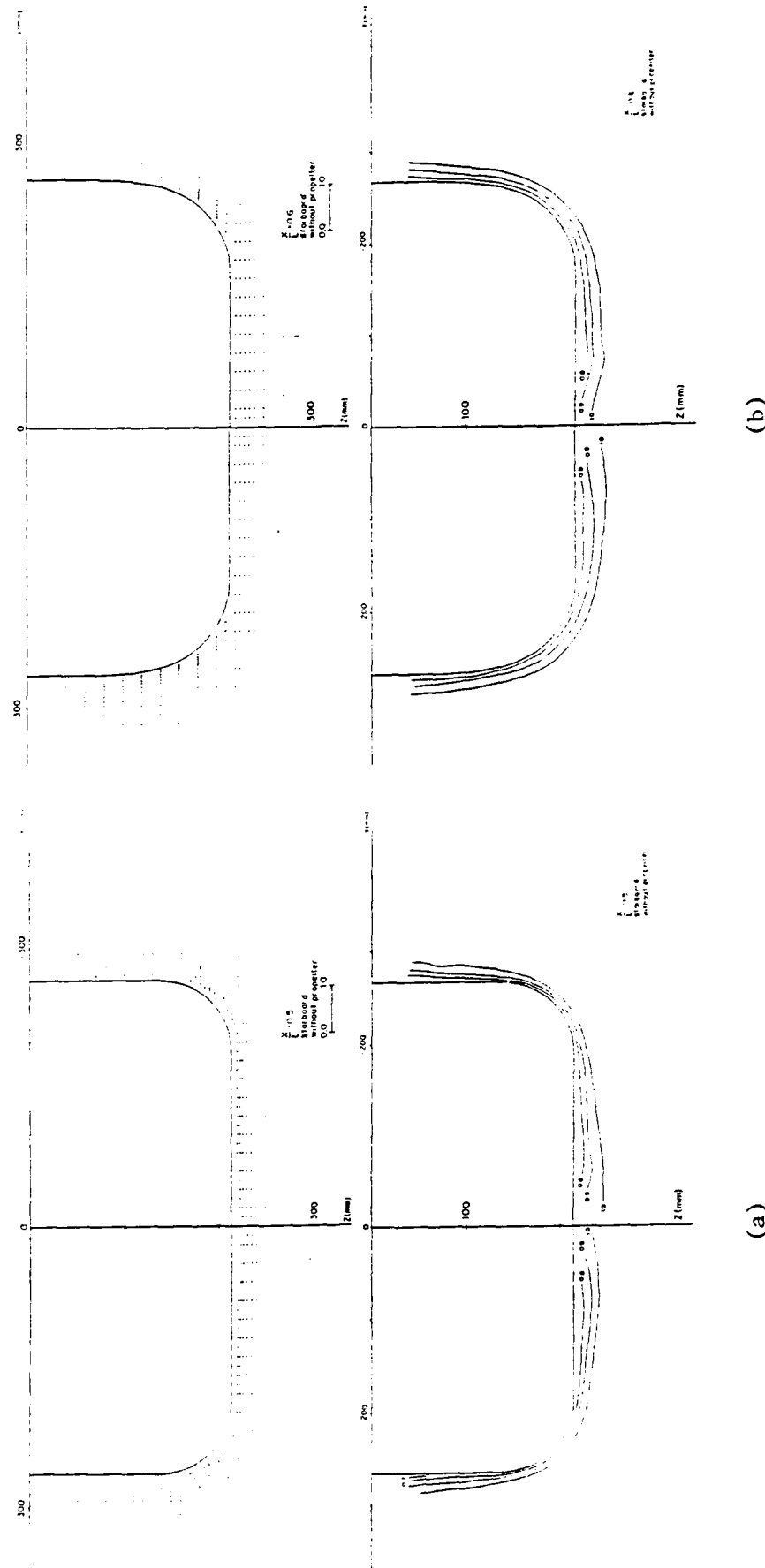


Figure 21. Mean-velocity crossplane vectors and axial velocity contours (continued).

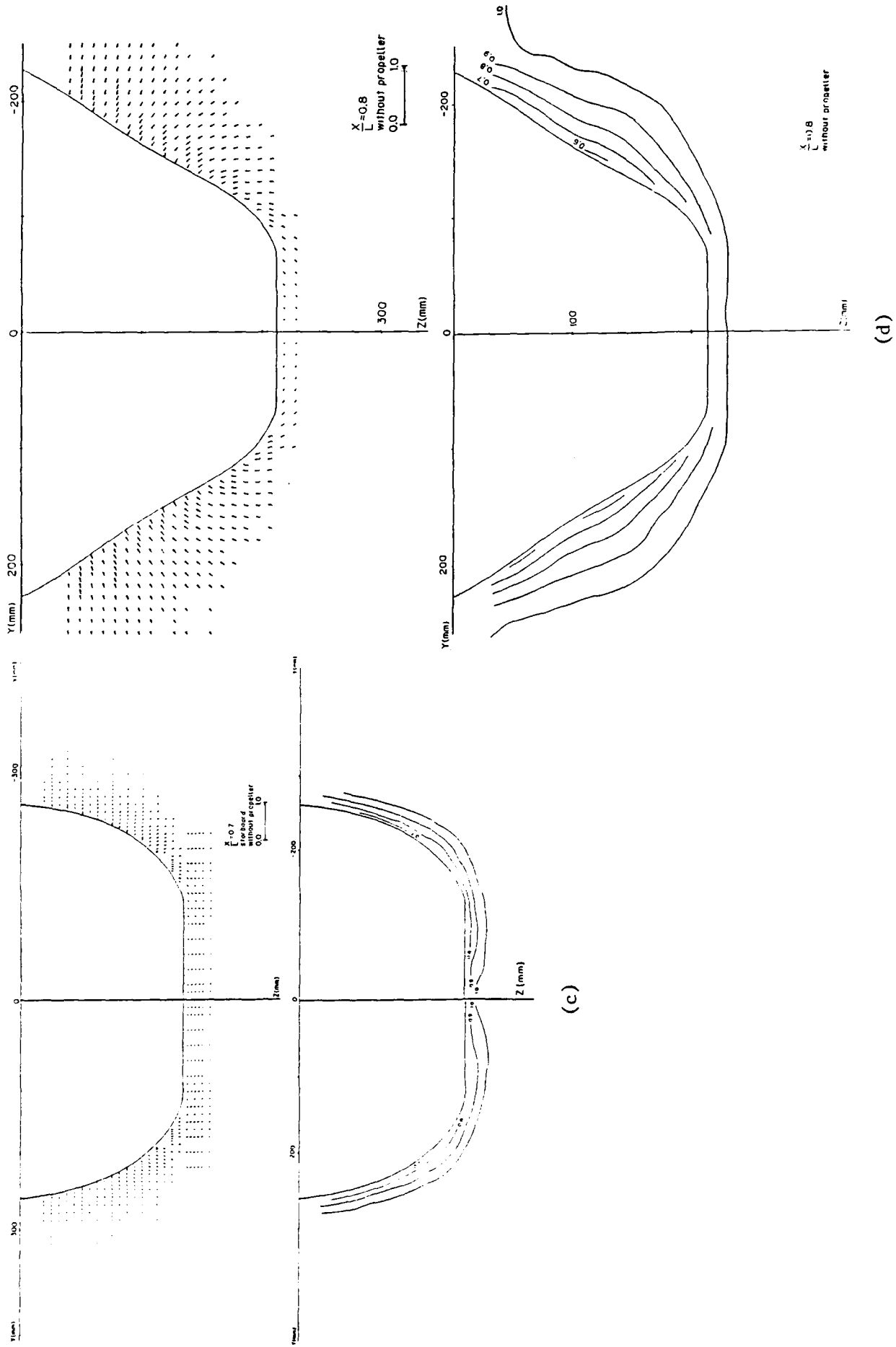


Figure 21 (continued)

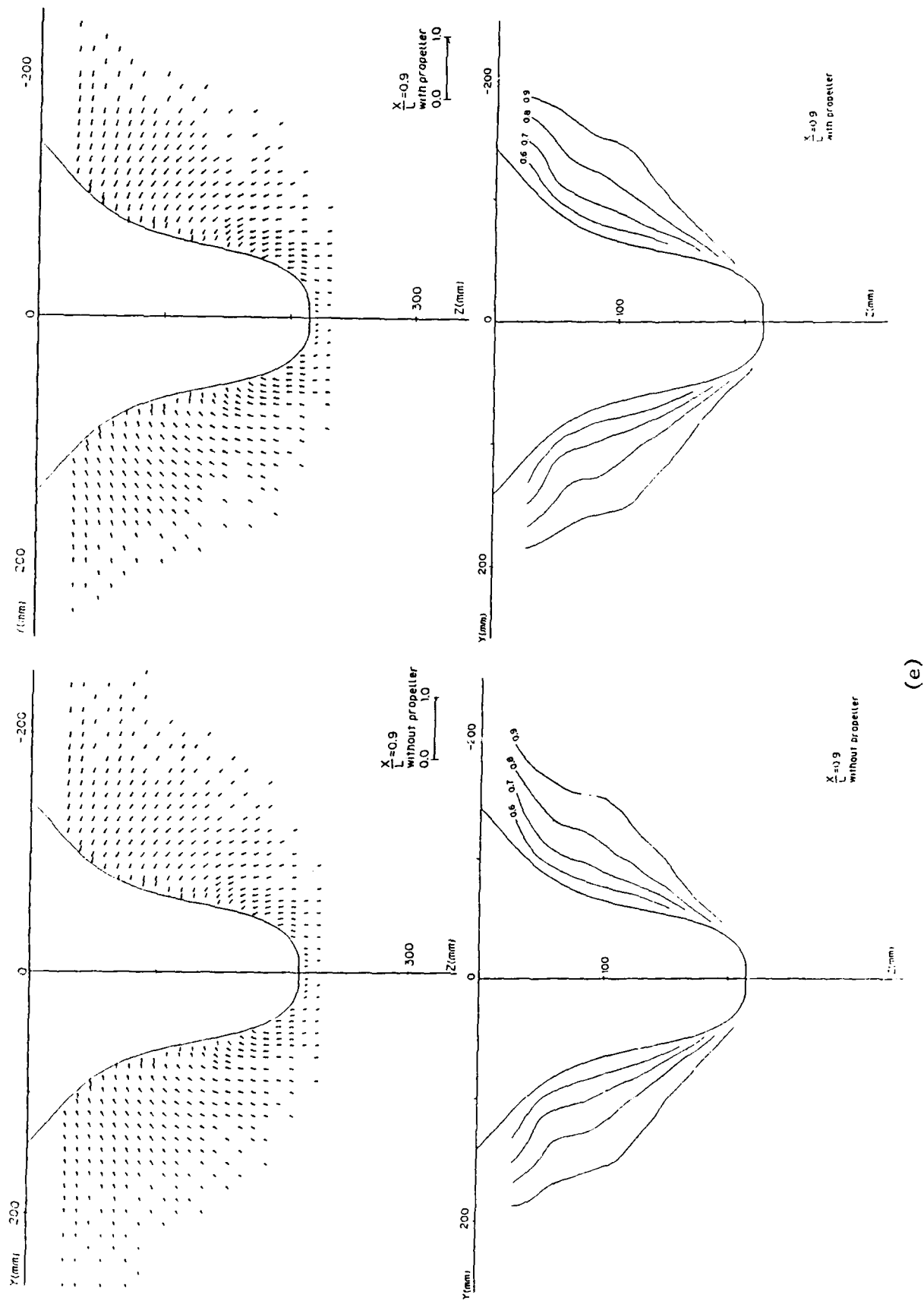
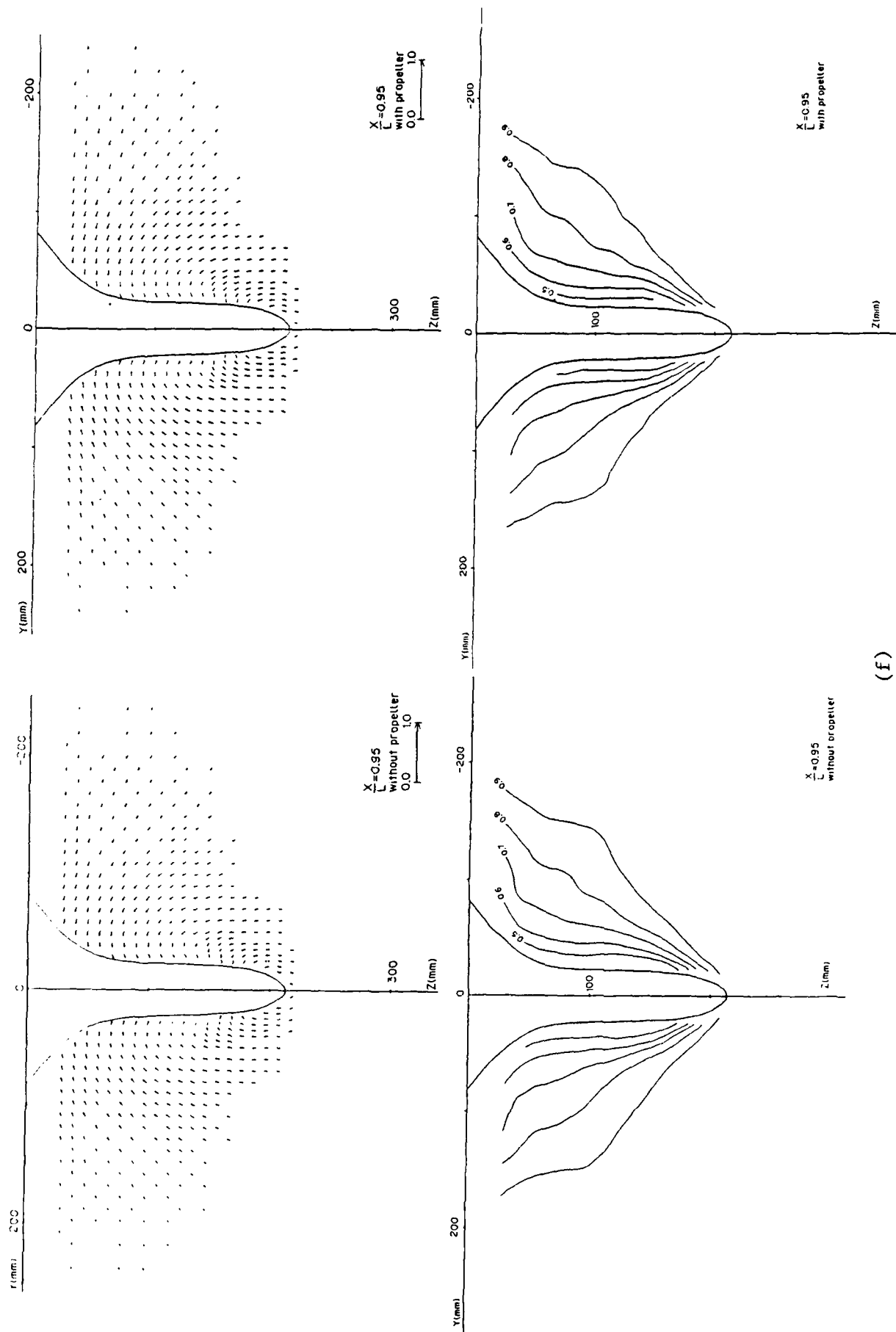
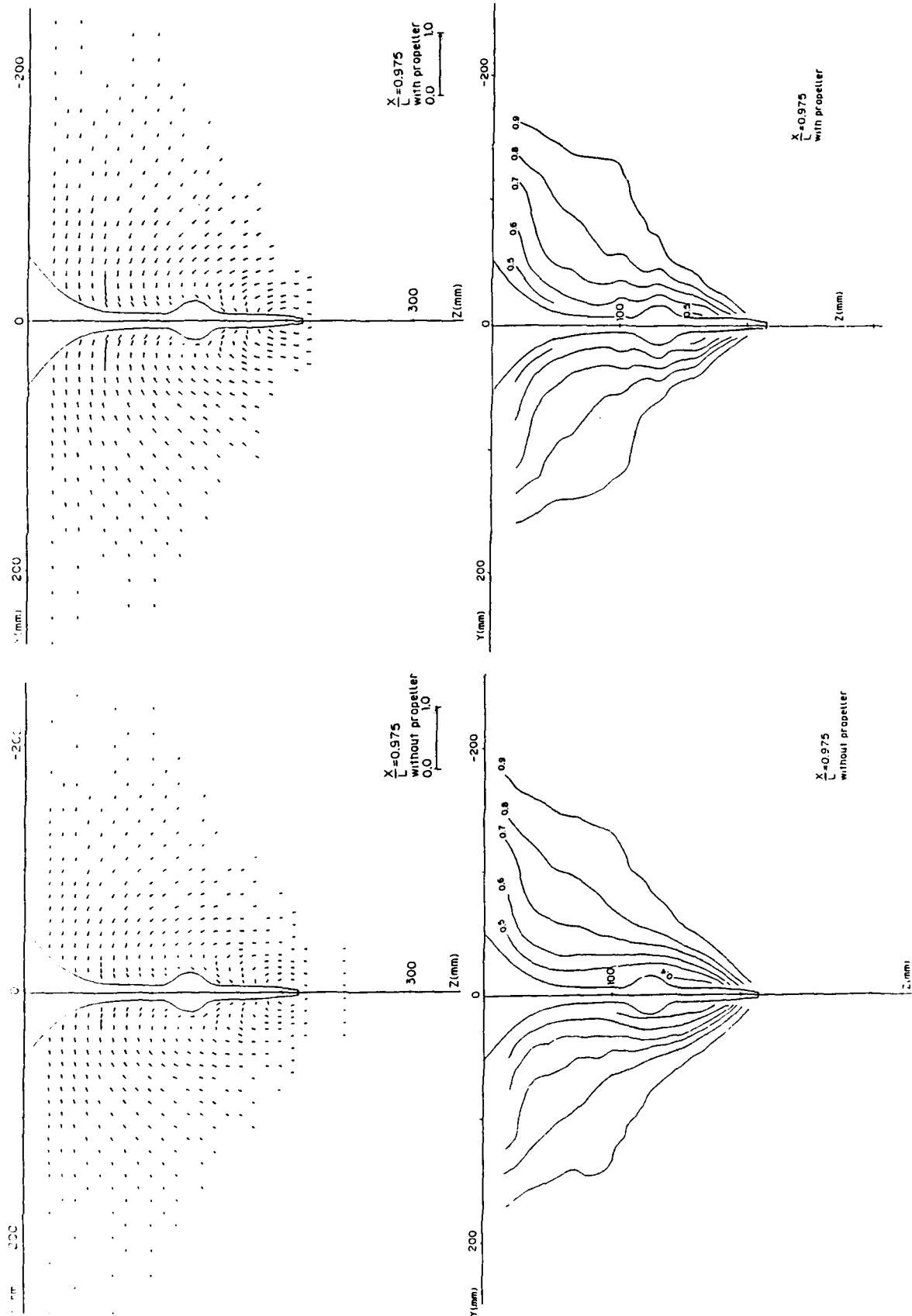


Figure 21. (continued)



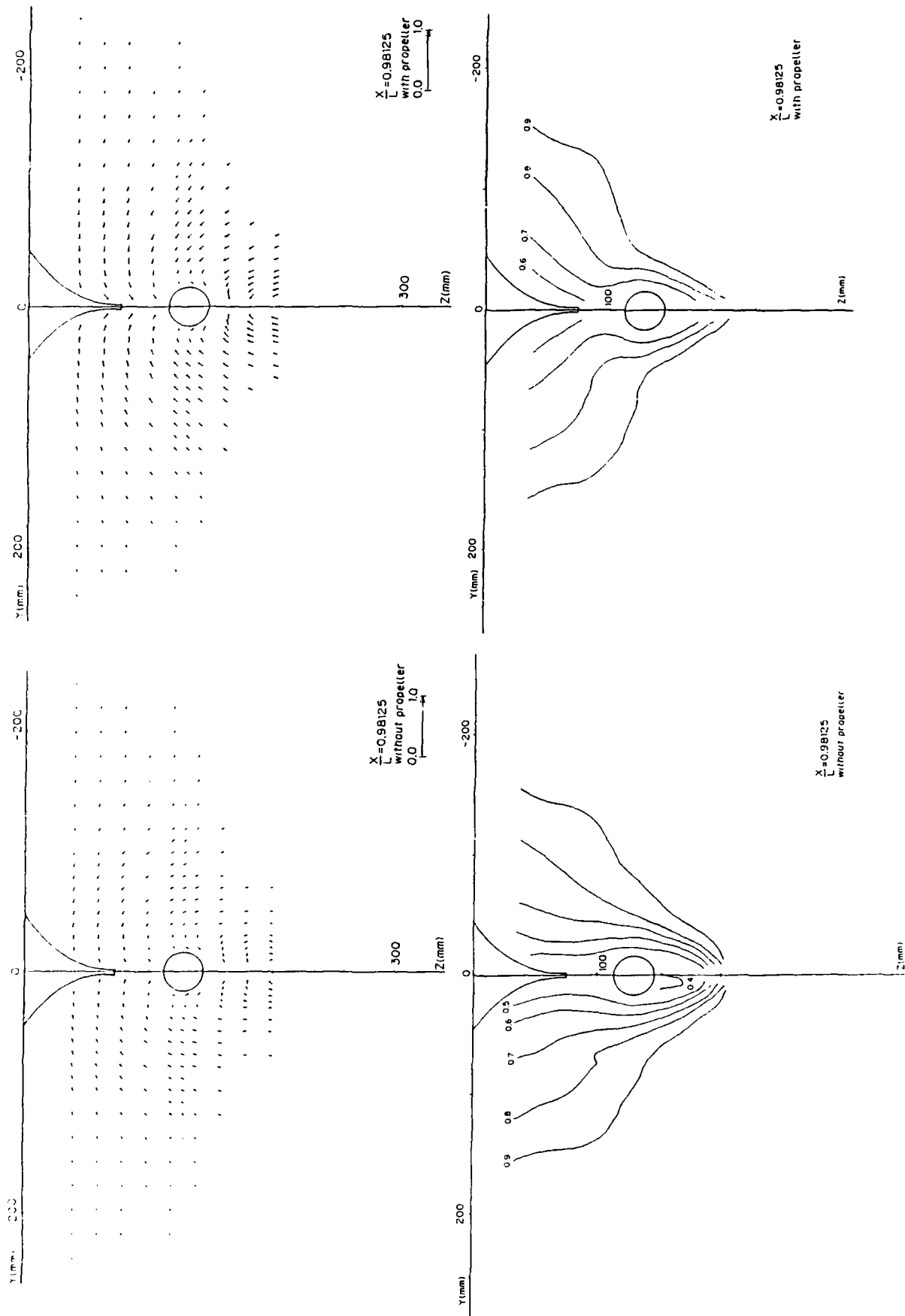
(f)

Figure 21. (continued)



(g)

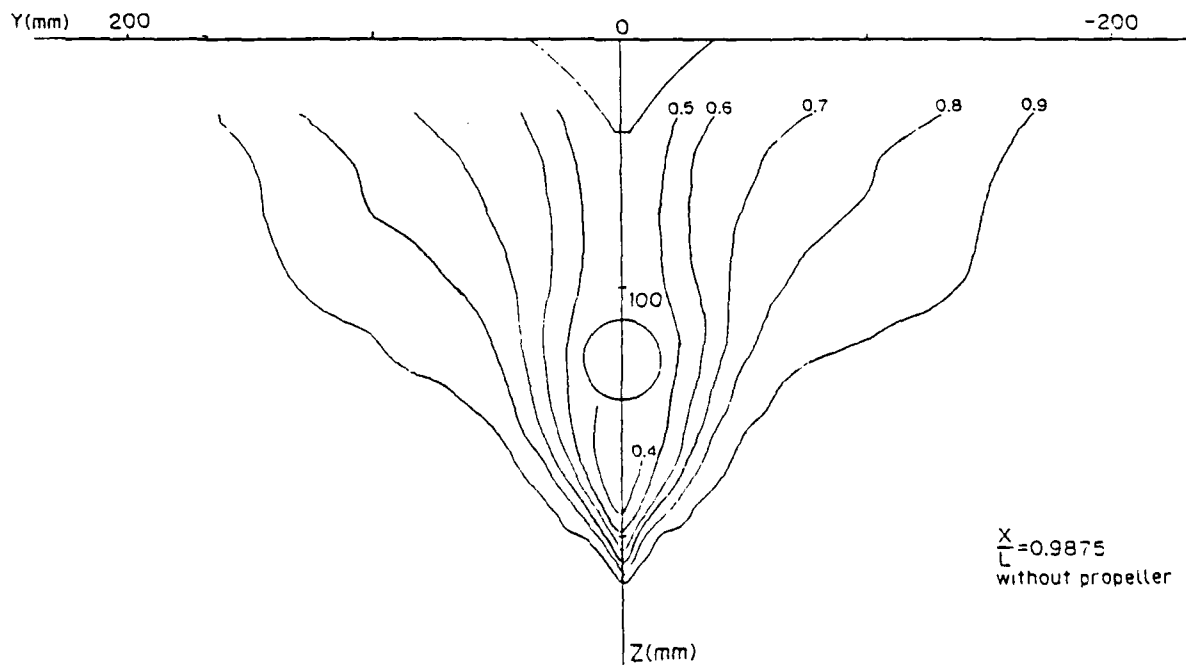
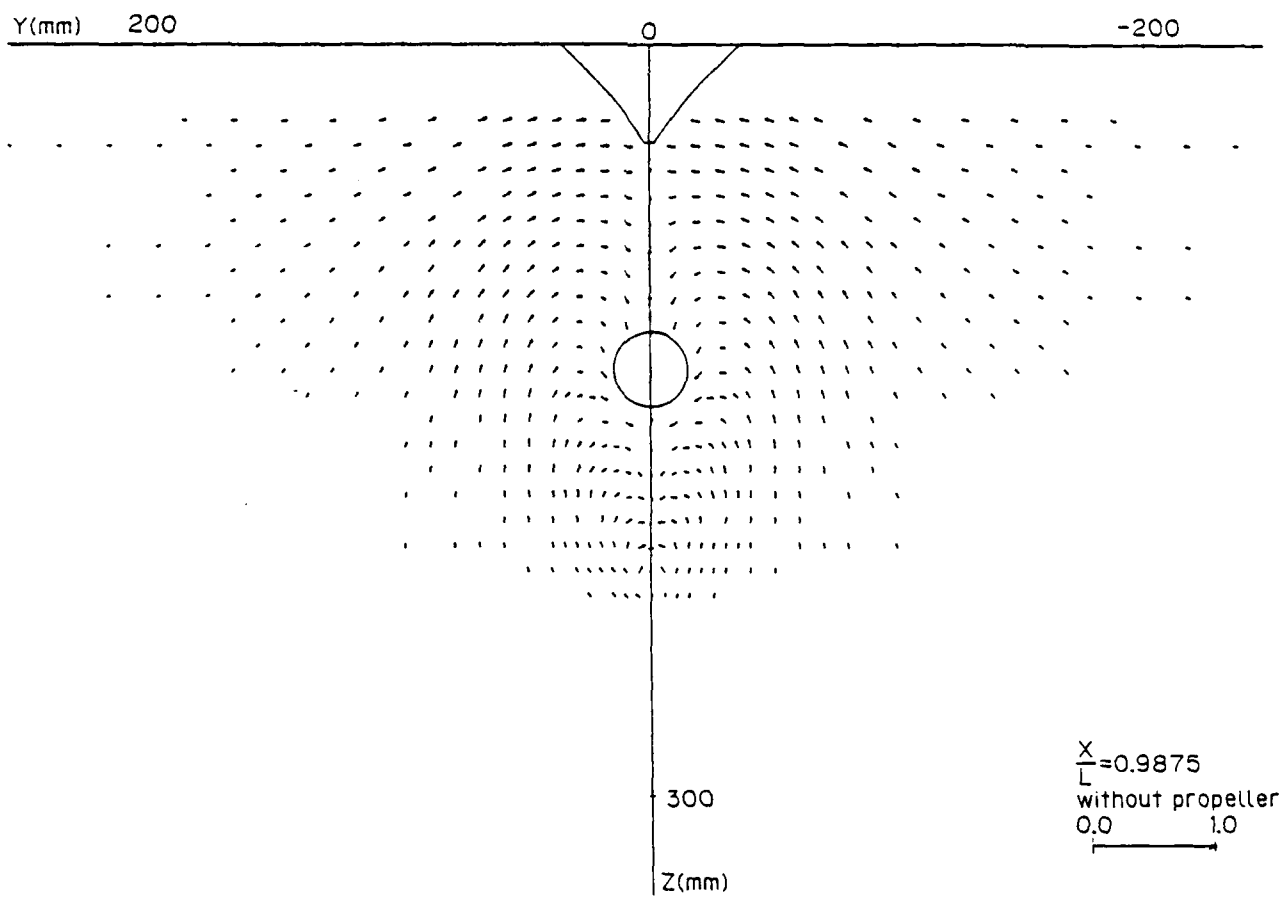
Figure 21. (continued)



(h)

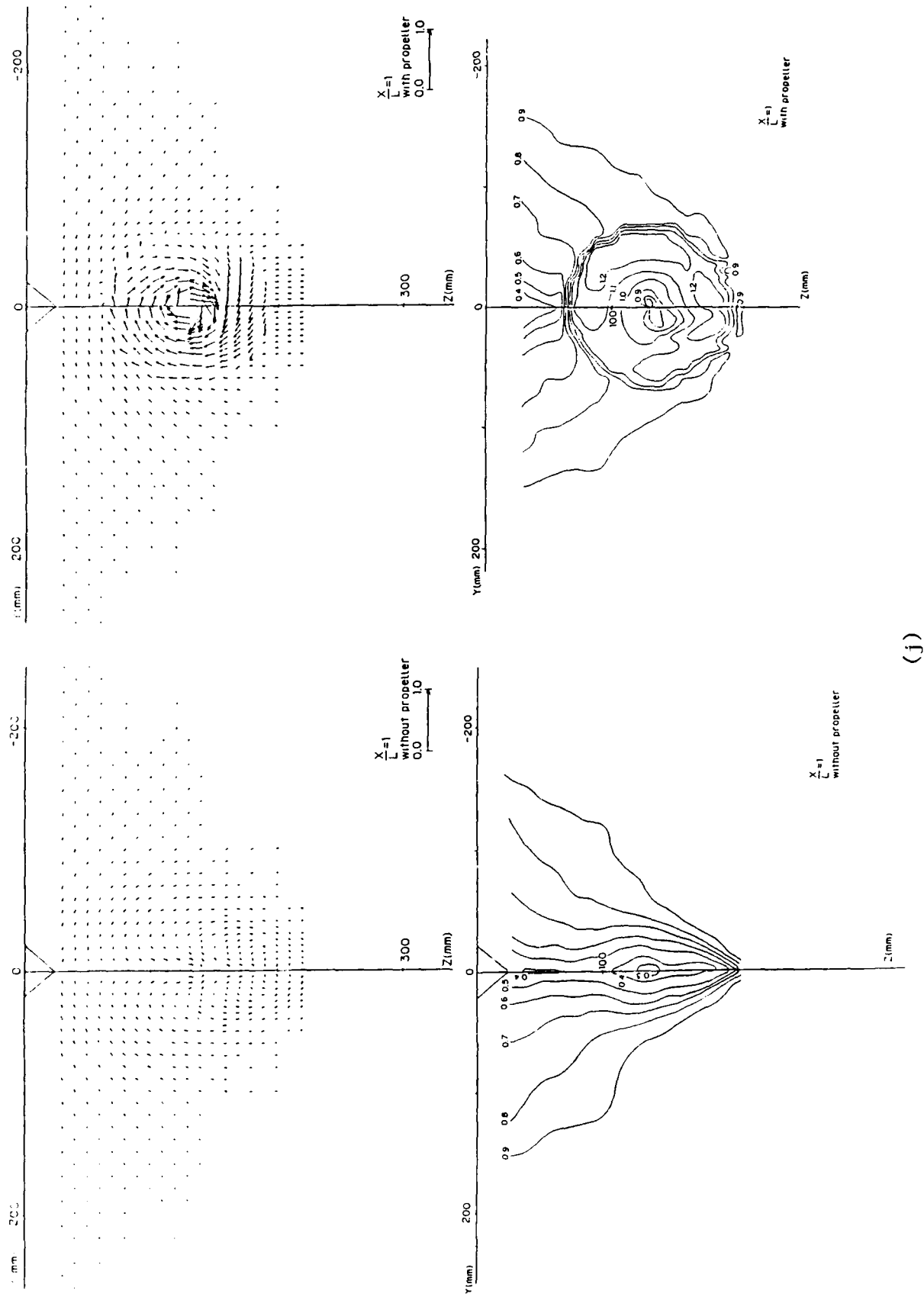
Figure 21. (continued)





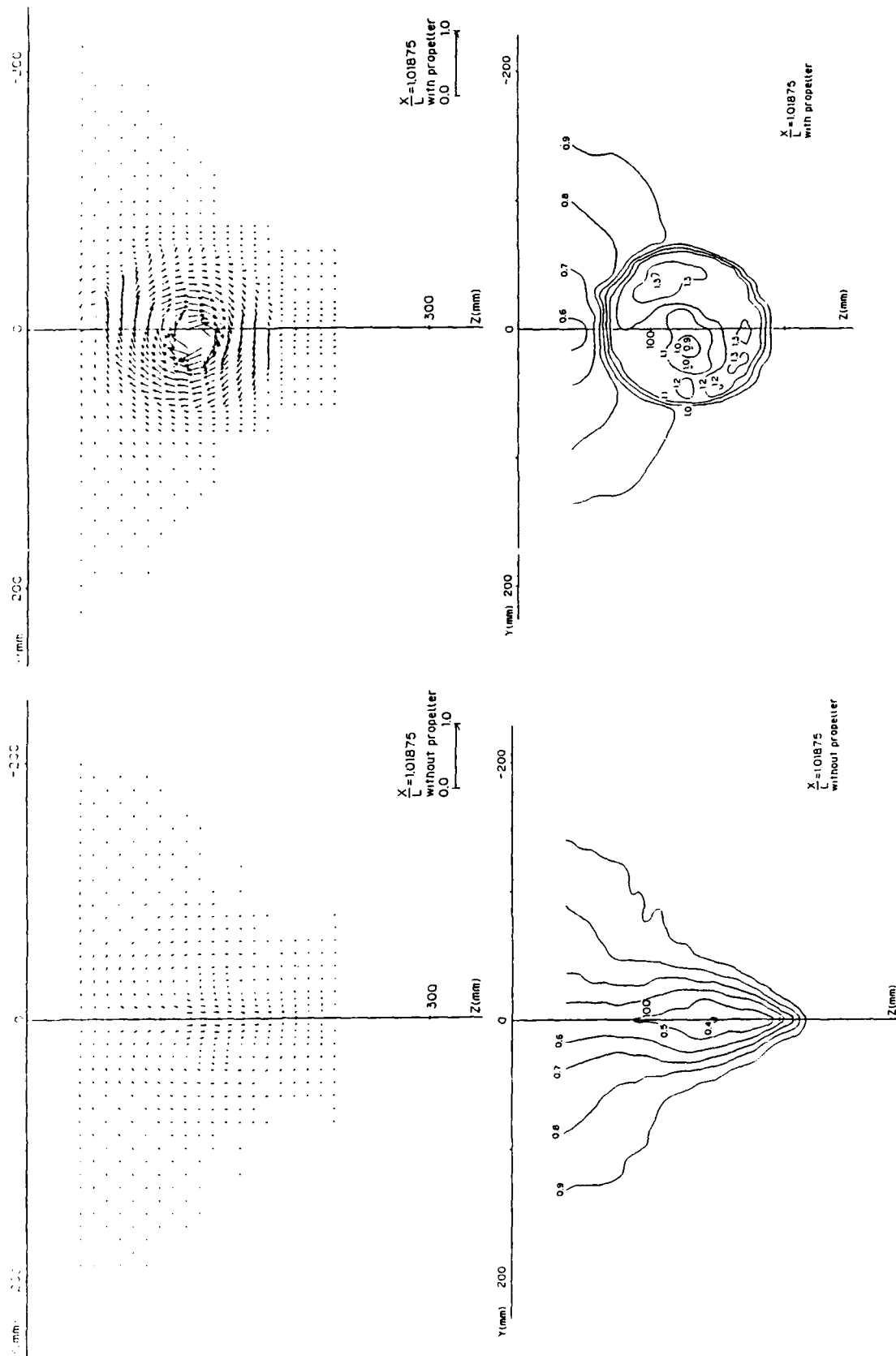
(i)

Figure 21. (continued)



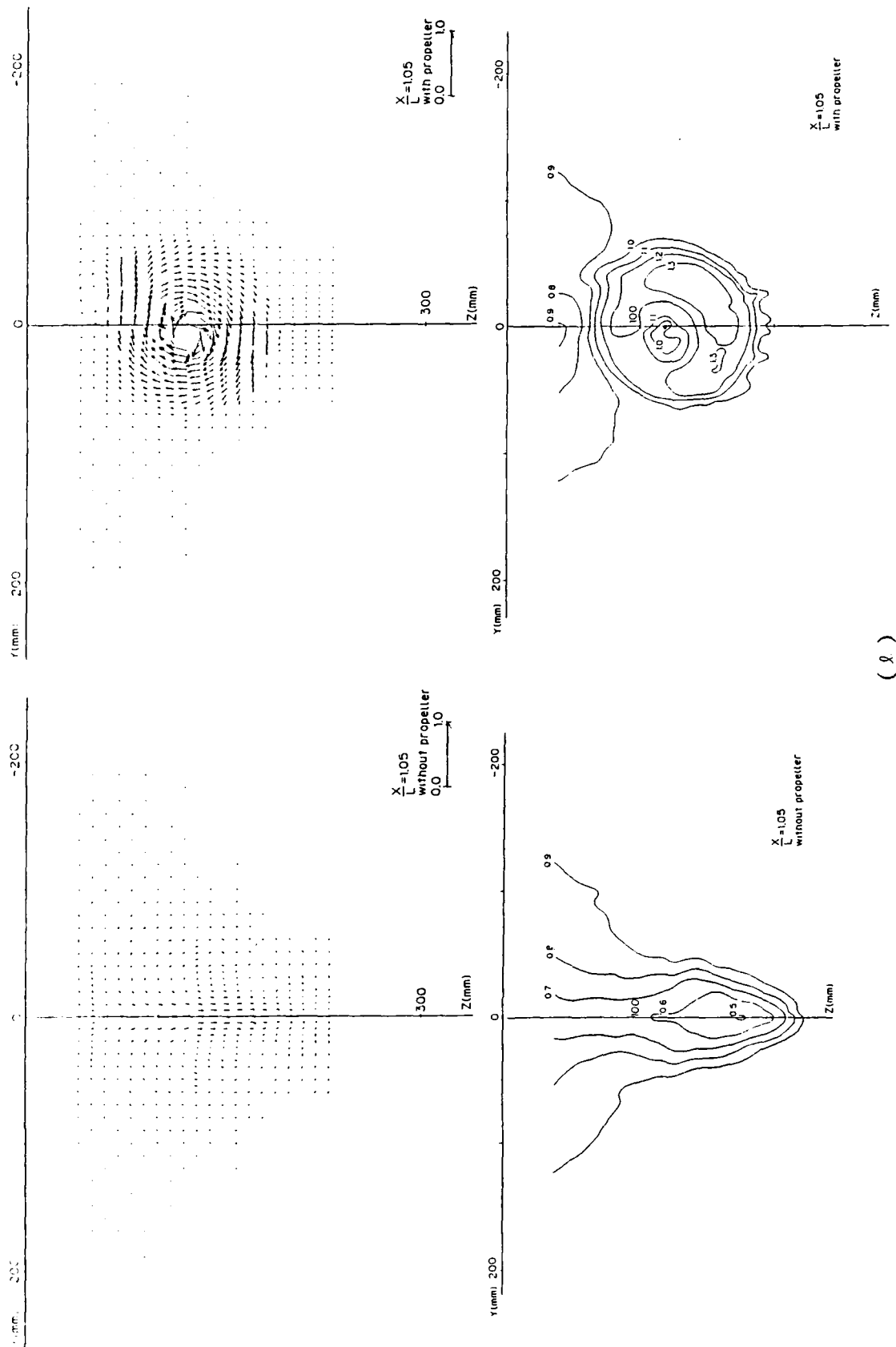
(j)

Figure 21. (continued)



(k)

Figure 21. (continued)



( 8 )

Figure 21. (continued)

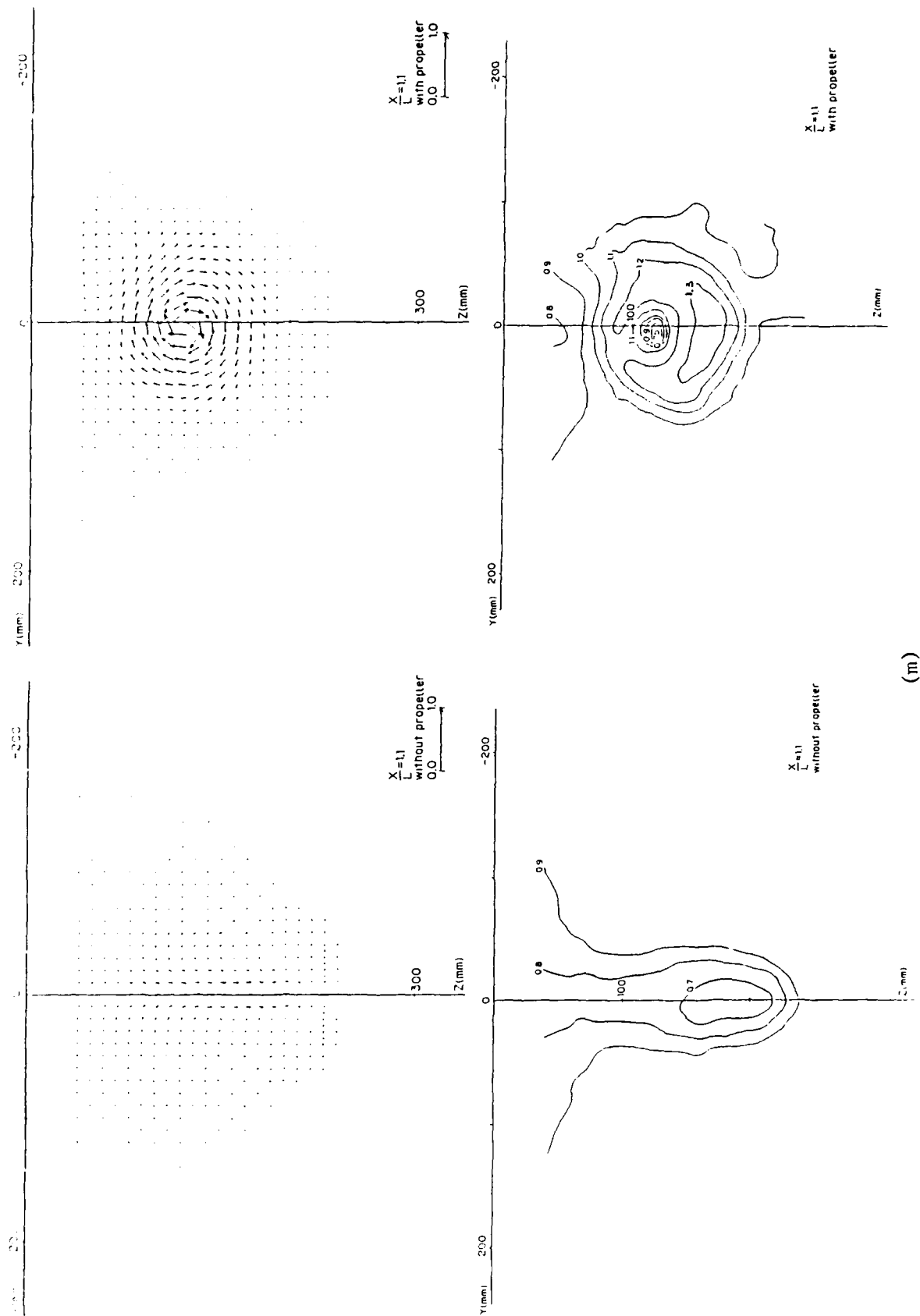


Figure 21. Mean-velocity crossplane vectors and axial velocity contours (concluded).

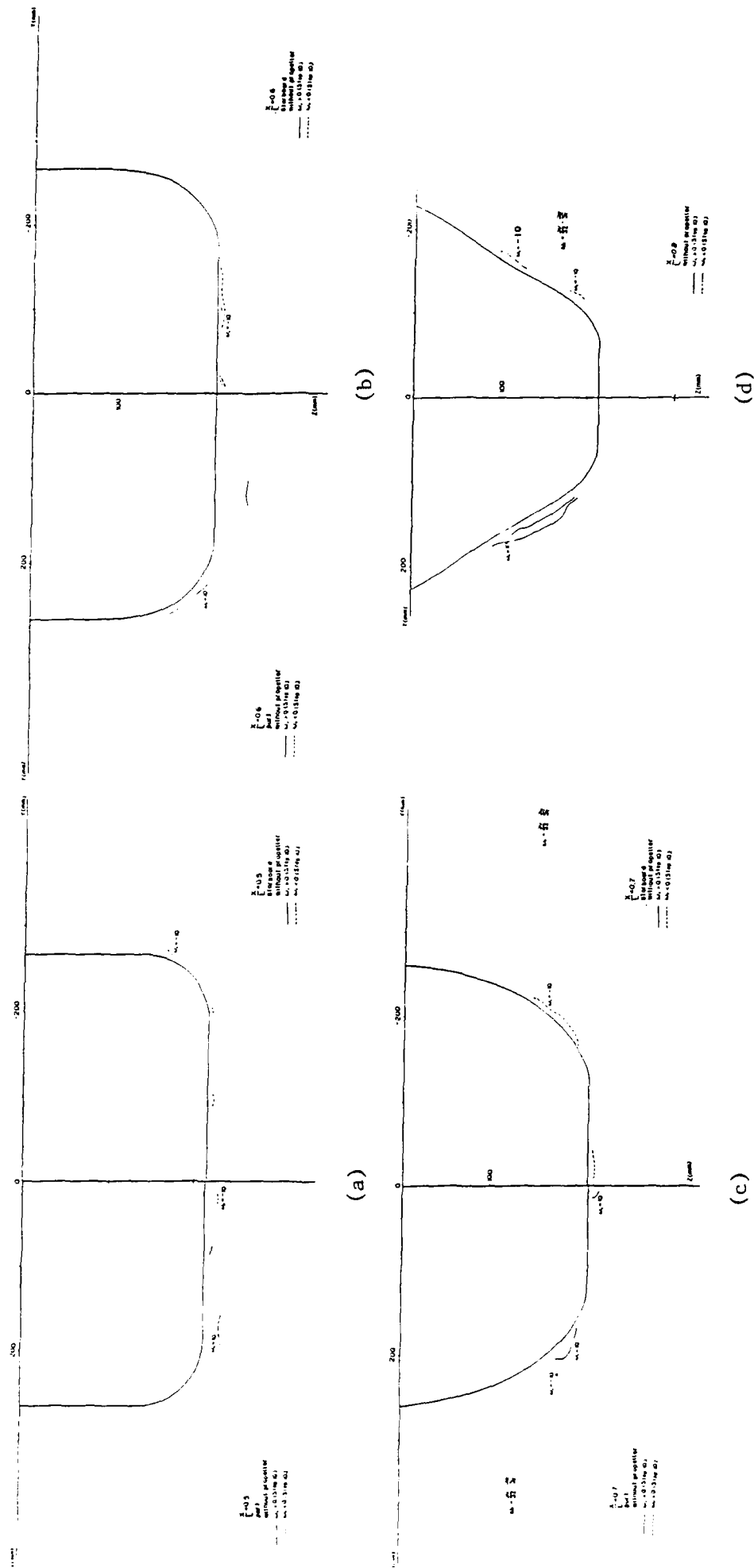


Figure 22. Axial vorticity contours (continued).

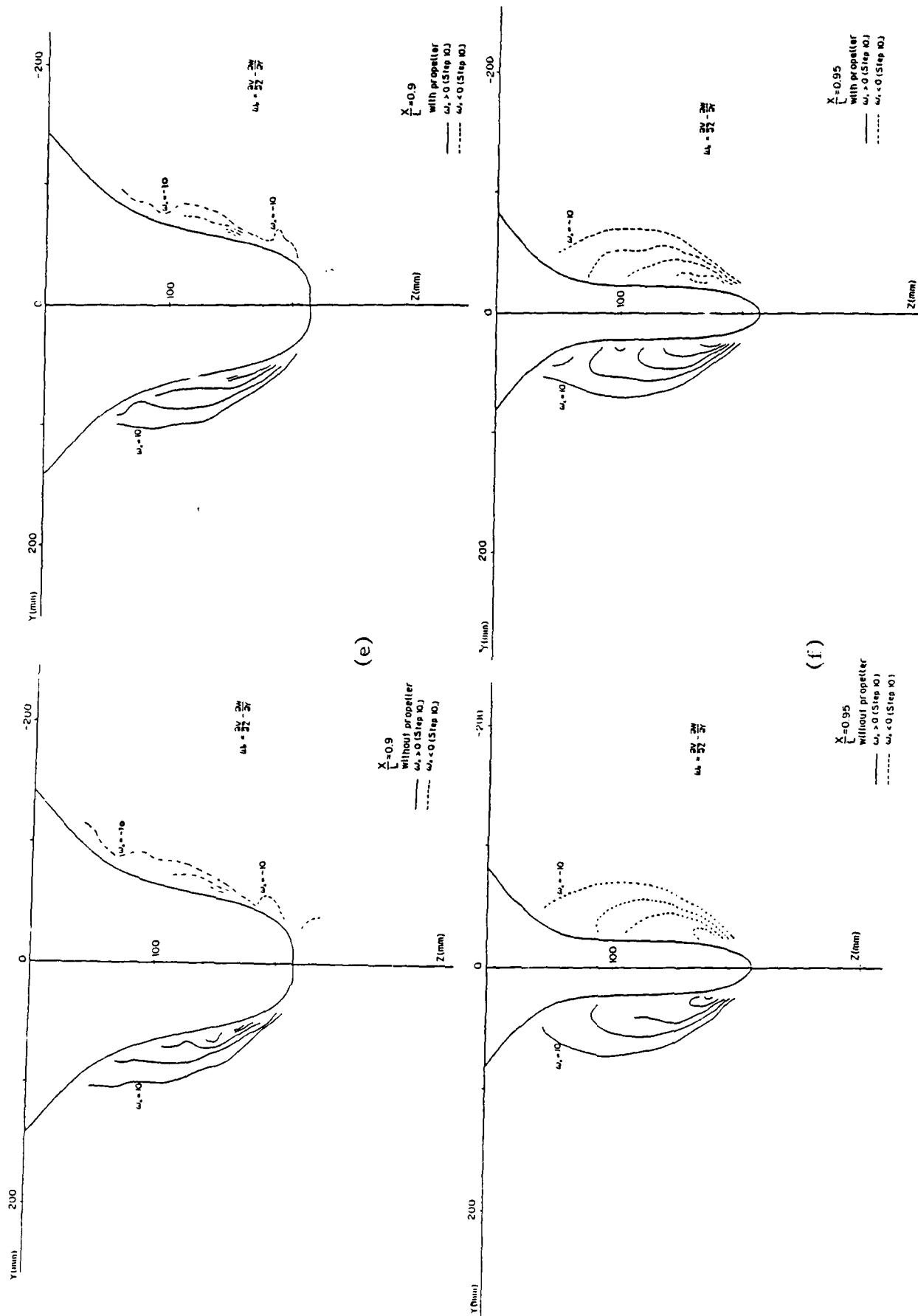
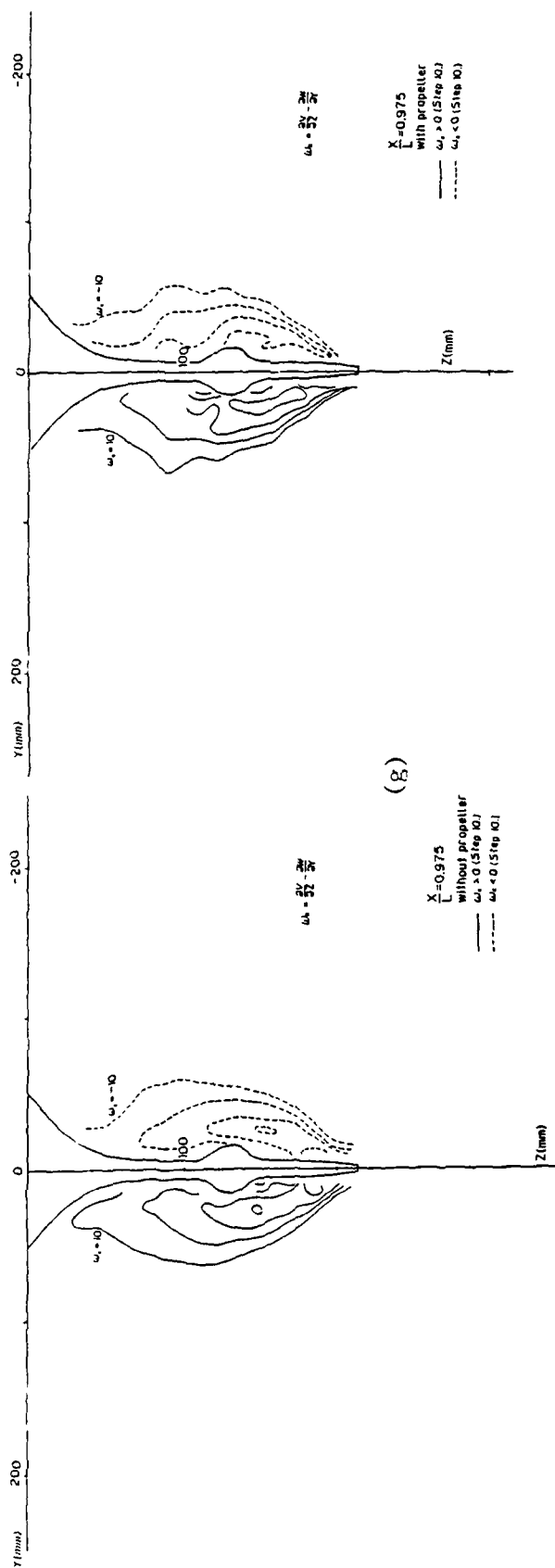


Figure 22. (continued)



65

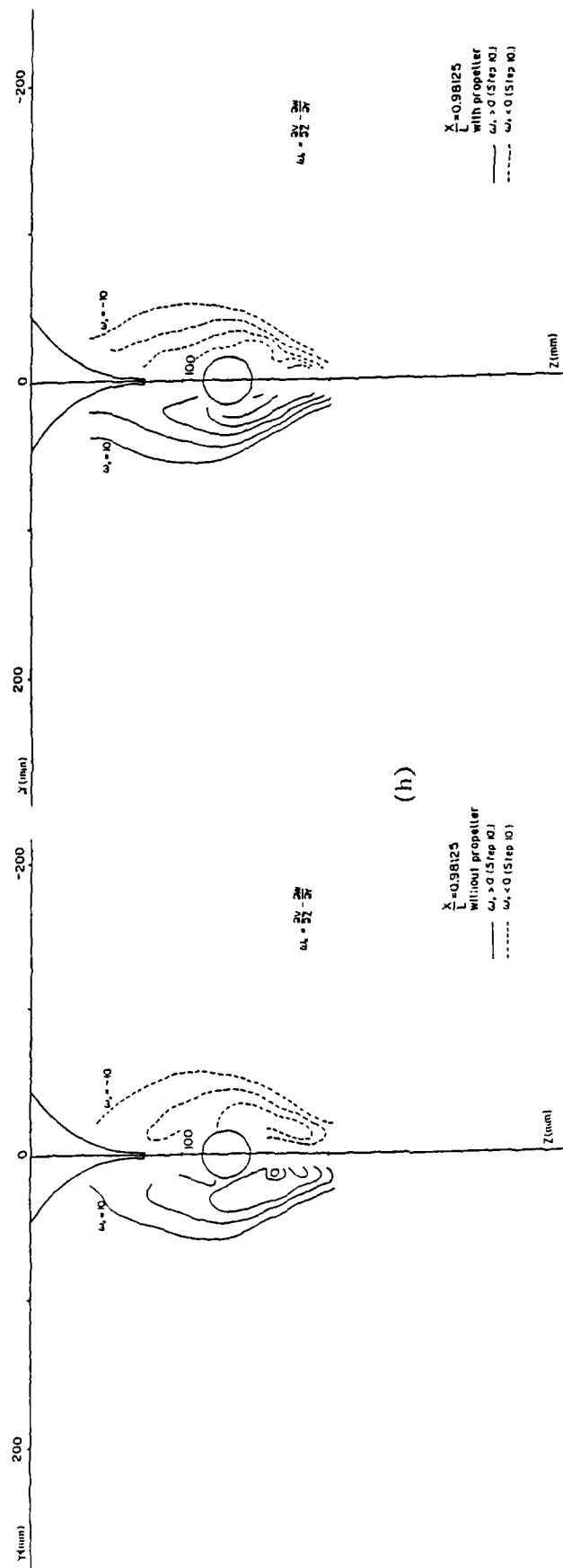


Figure 22. (continued)



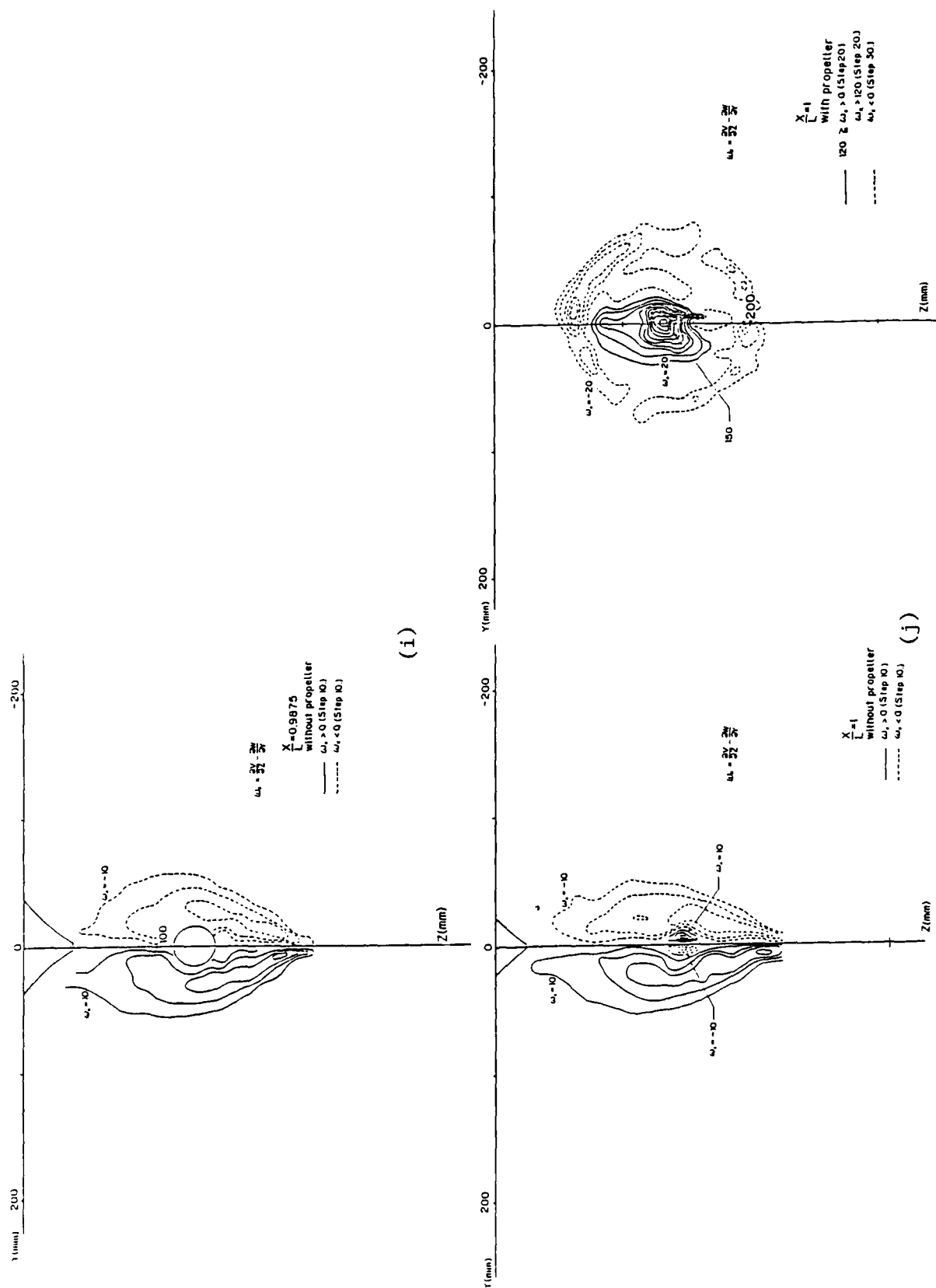


Figure 22. (continued)

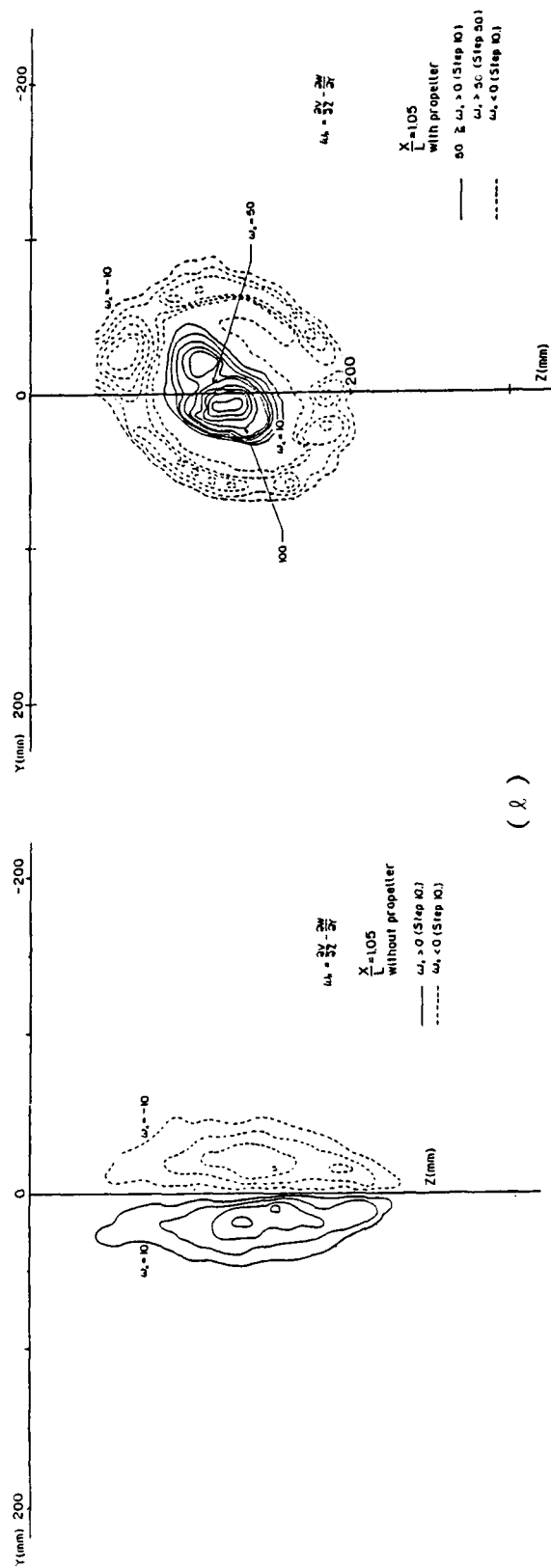
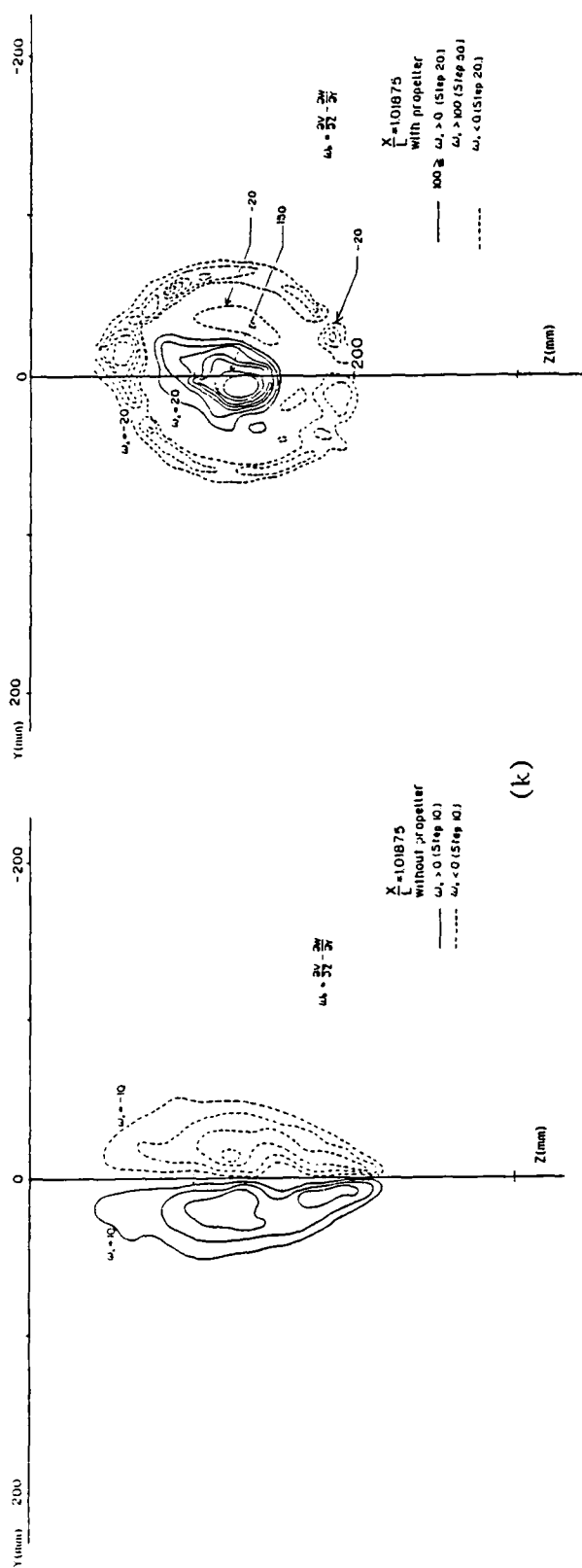
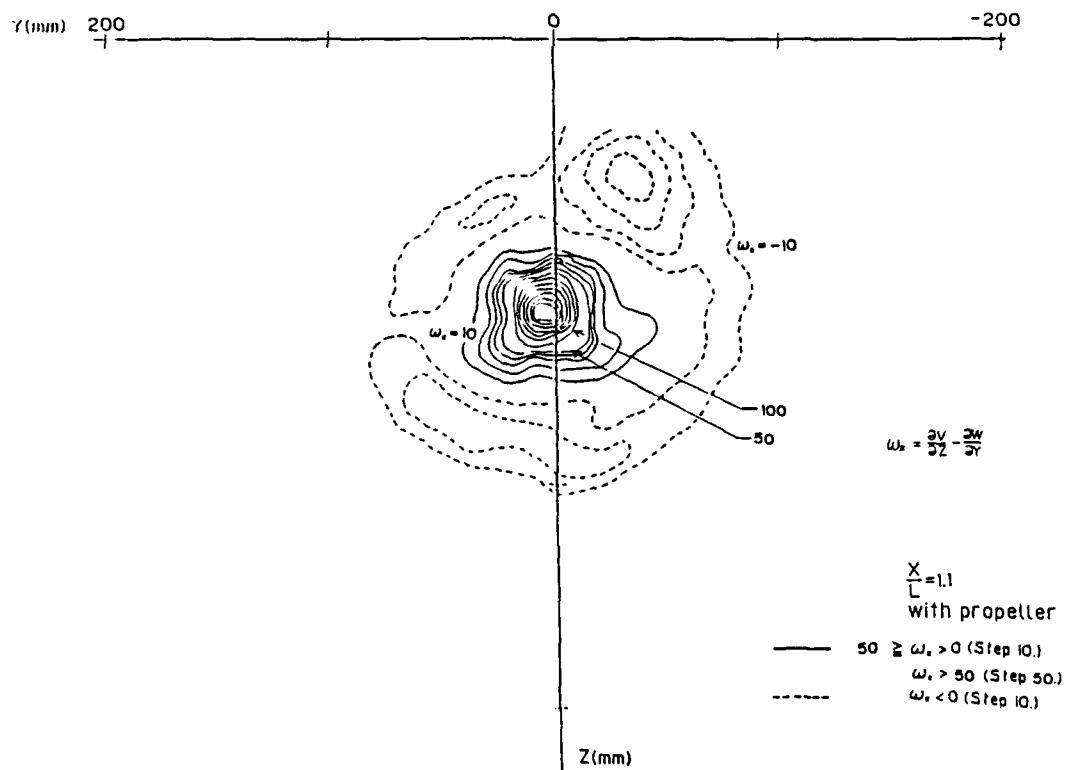
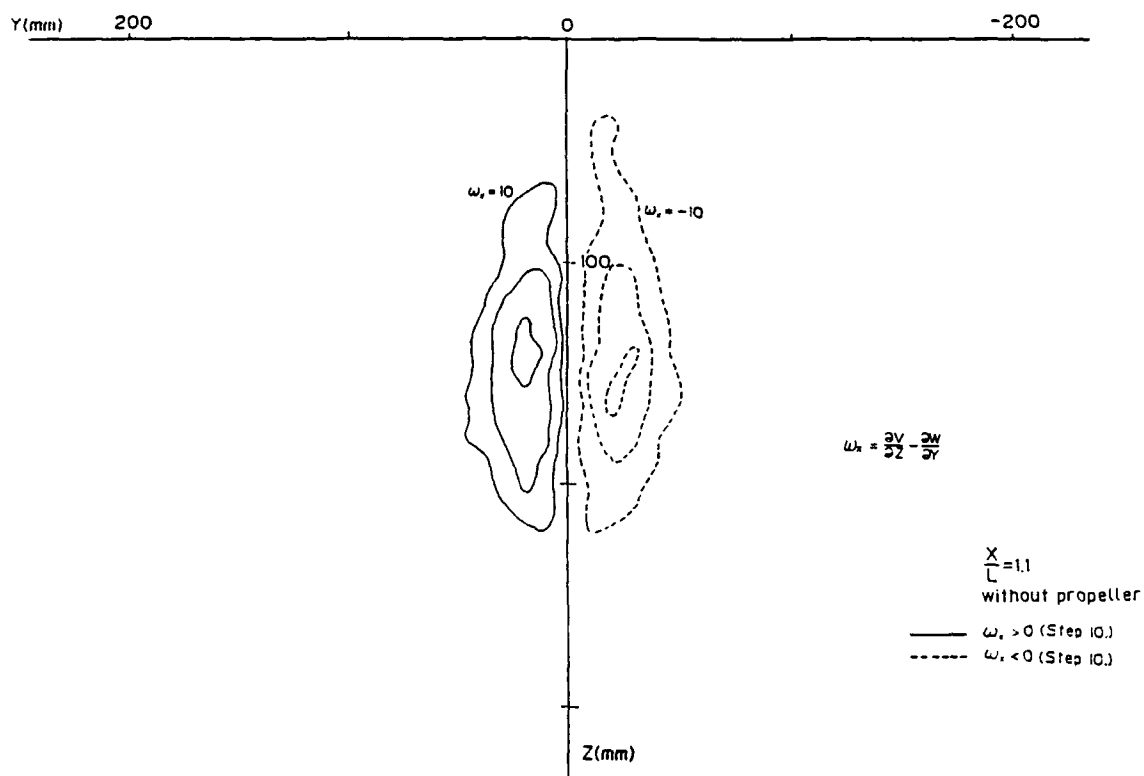


Figure 22. (continued)



(m)

Figure 22. Axial vorticity contours (concluded).

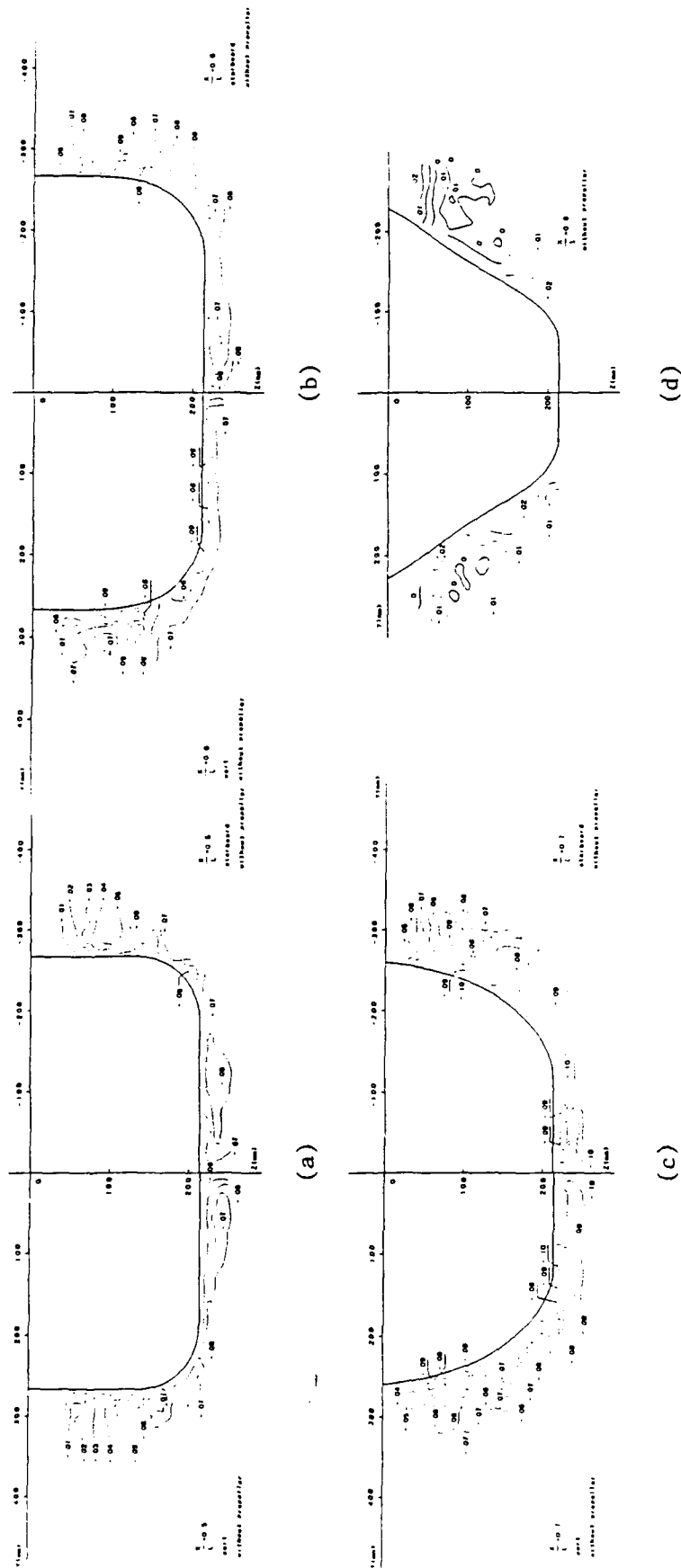
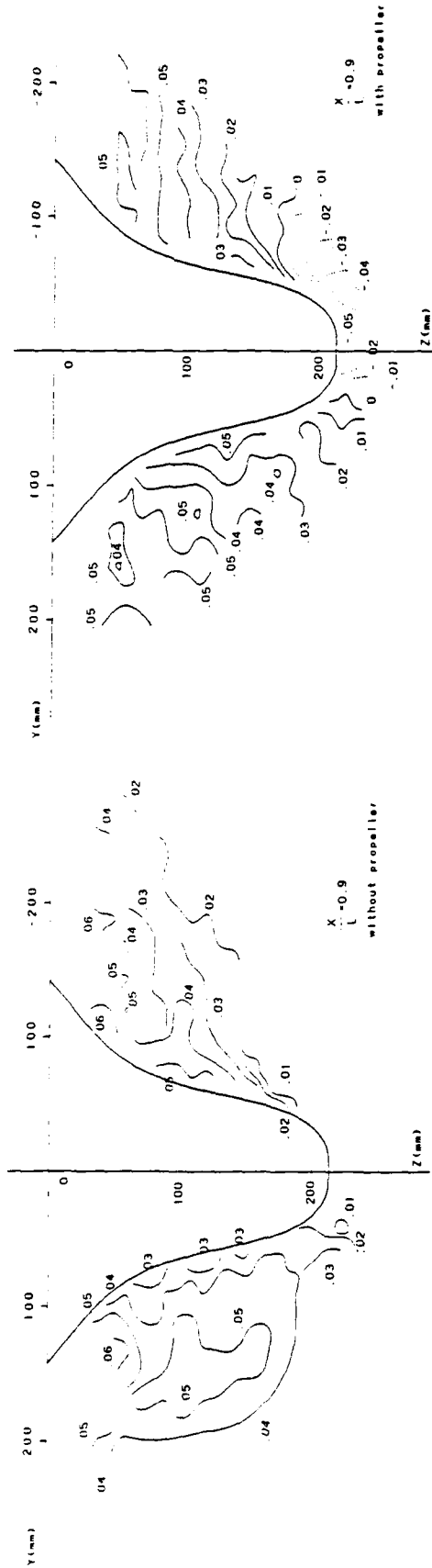
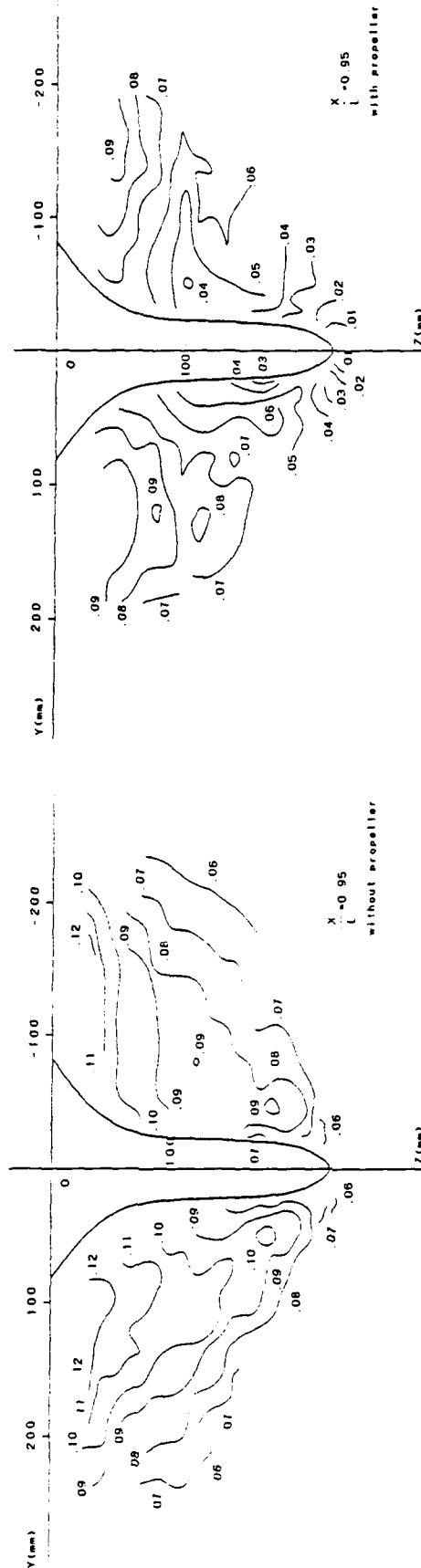


Figure 23. Pressure contours (continued).



(p)



(f)

Figure 23. (continued)

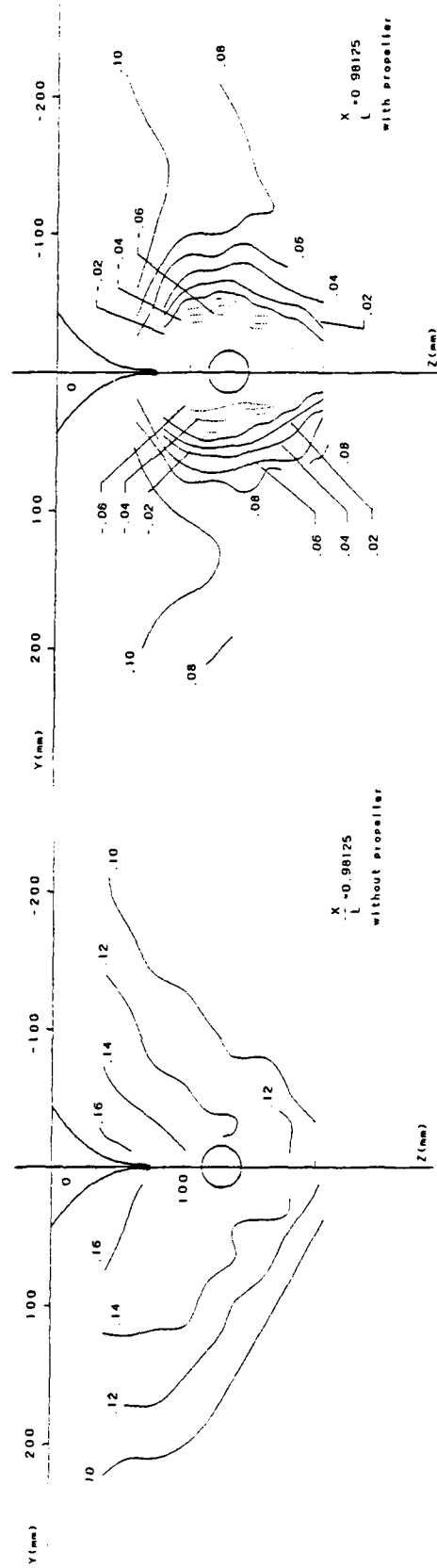
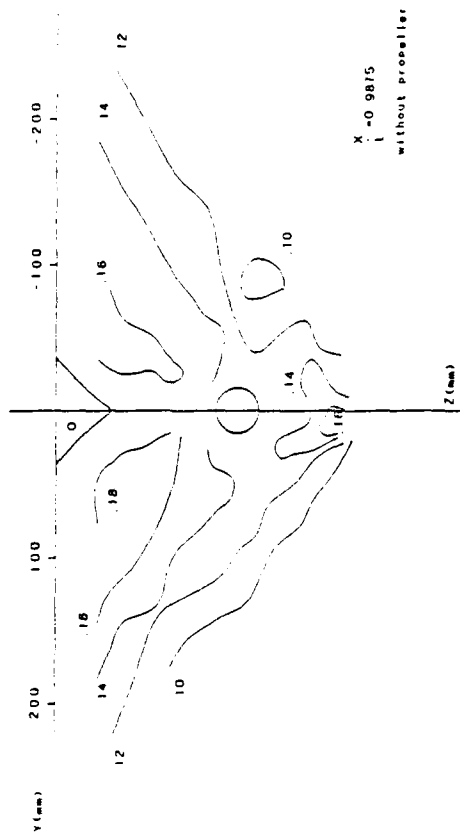
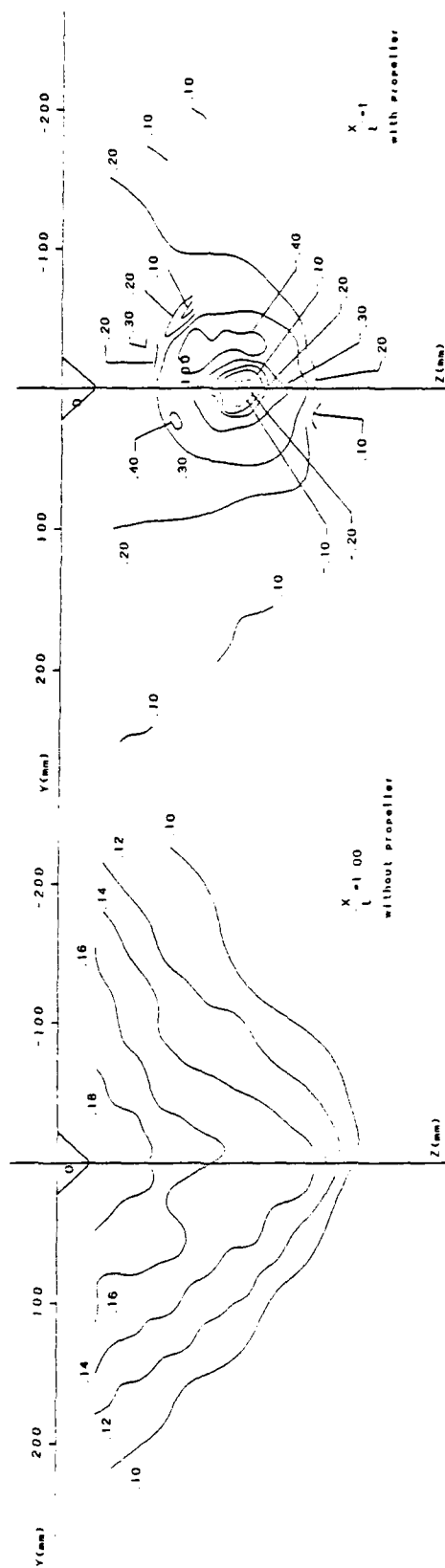


Figure 23. (continued)

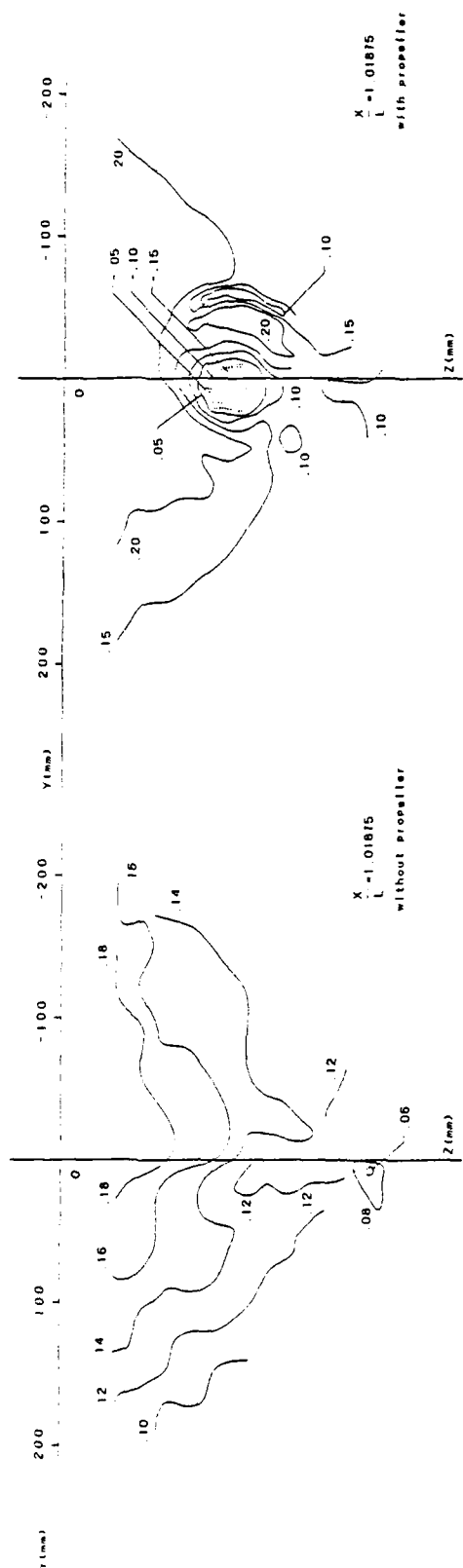


(i)



(j)

Figure 23. (continued)



(k)



(l)

Figure 23. (continued)



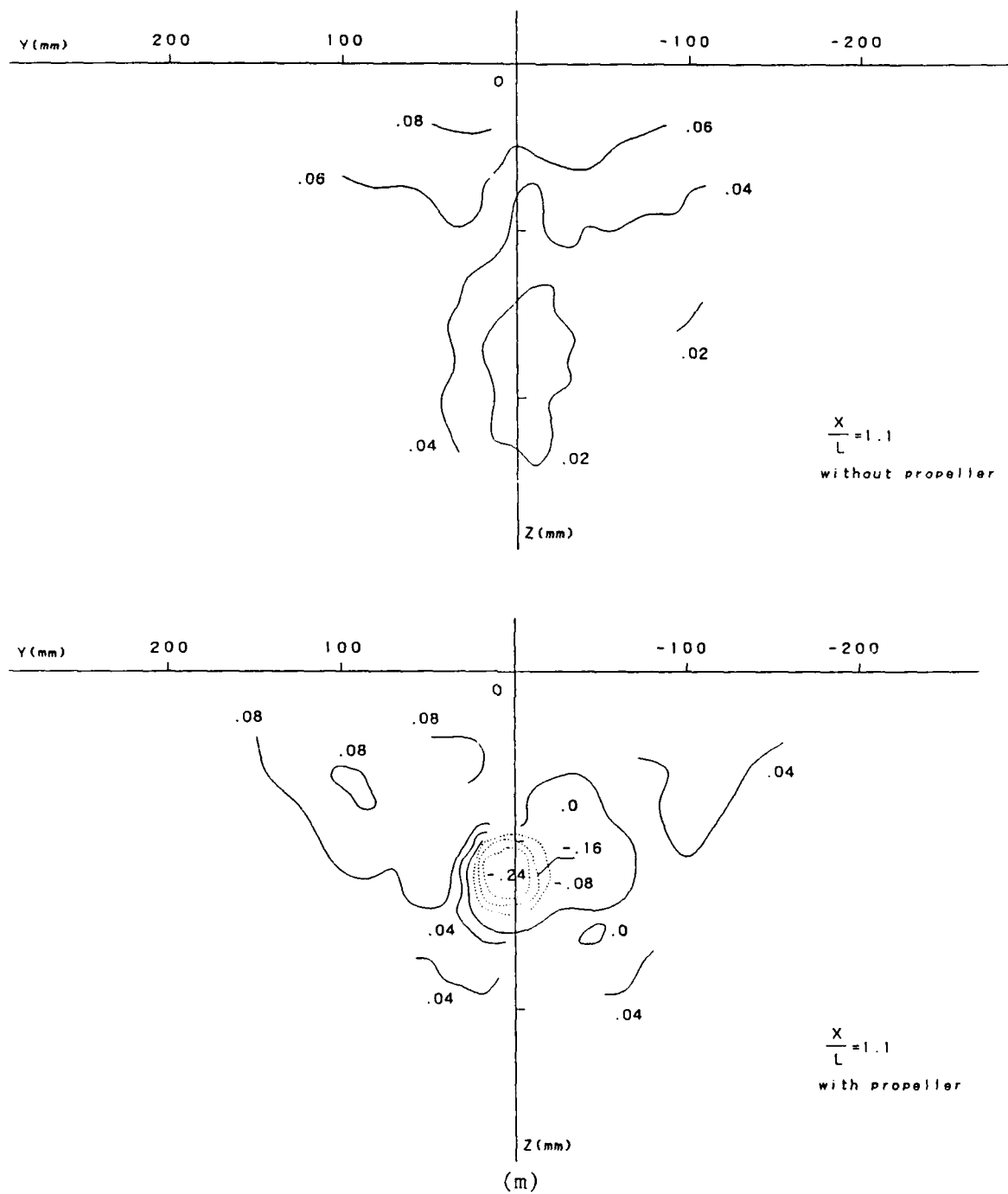


Figure 23. Pressure contours (concluded).

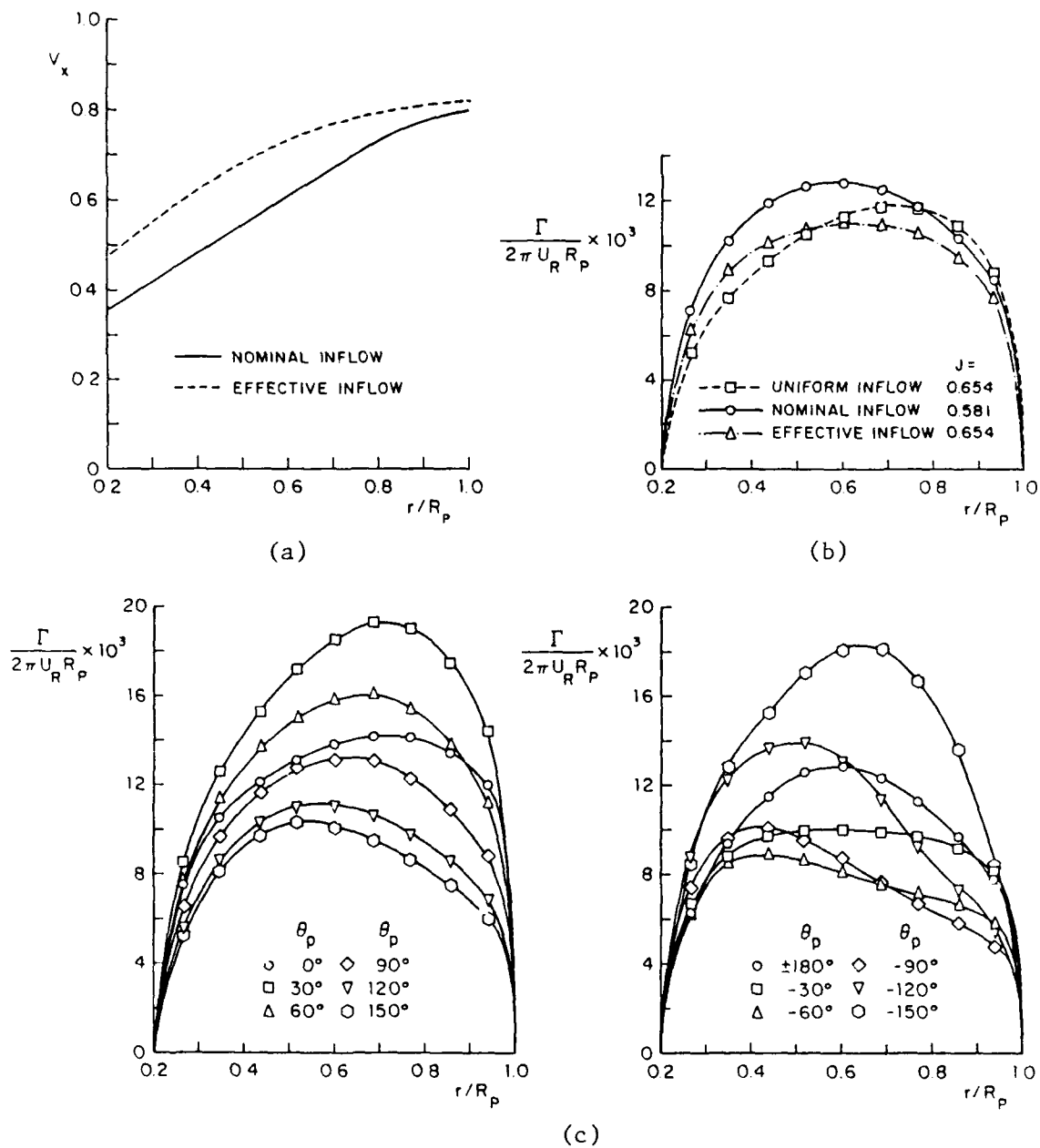


Figure 24. Circumferential-average axial velocity (a) (nominal and effective inflow) and spanwise circulation distributions; (b) circumferential average (uniform, nominal, and effective inflow); and (c) angular variation (nominal inflow).

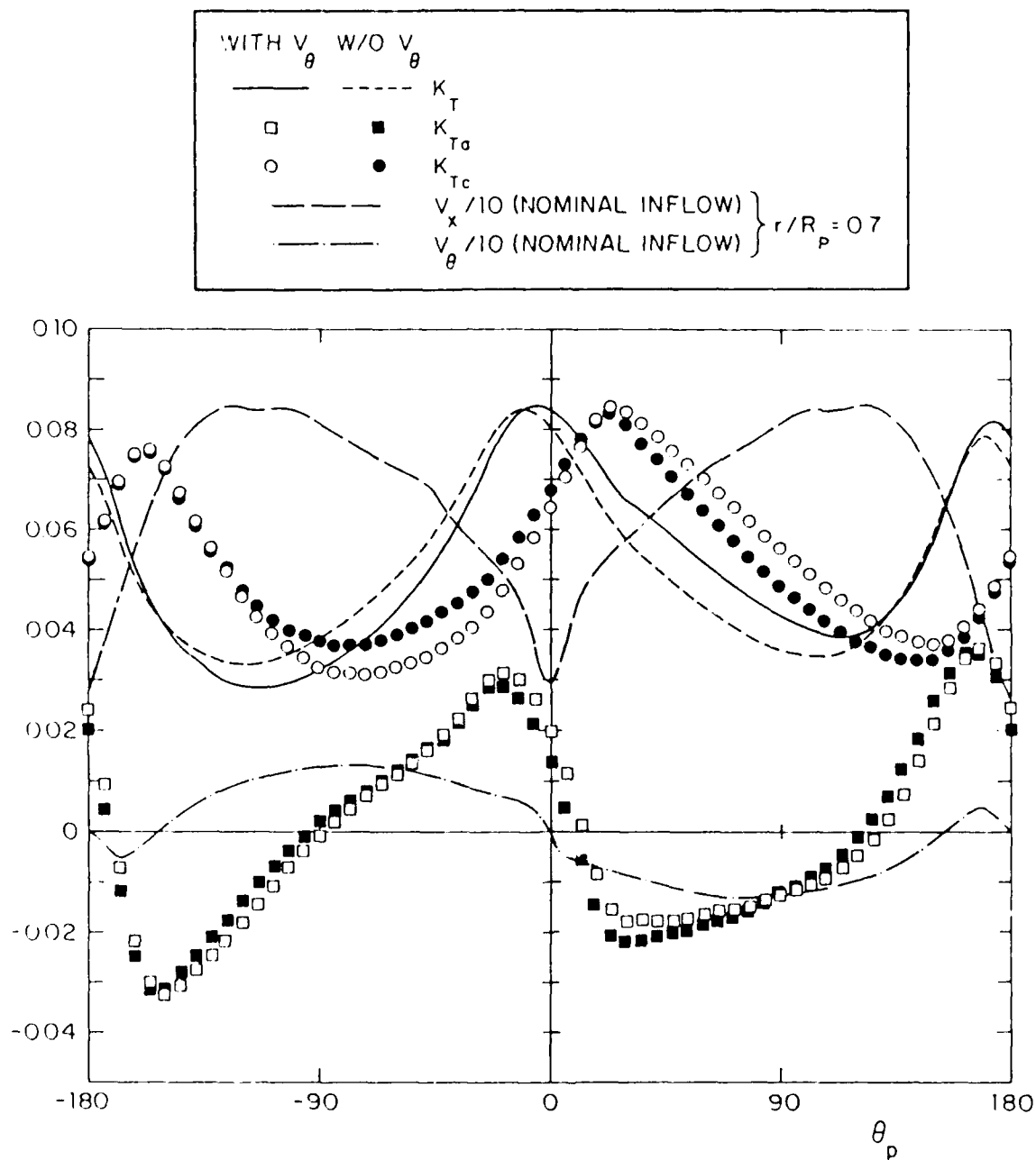
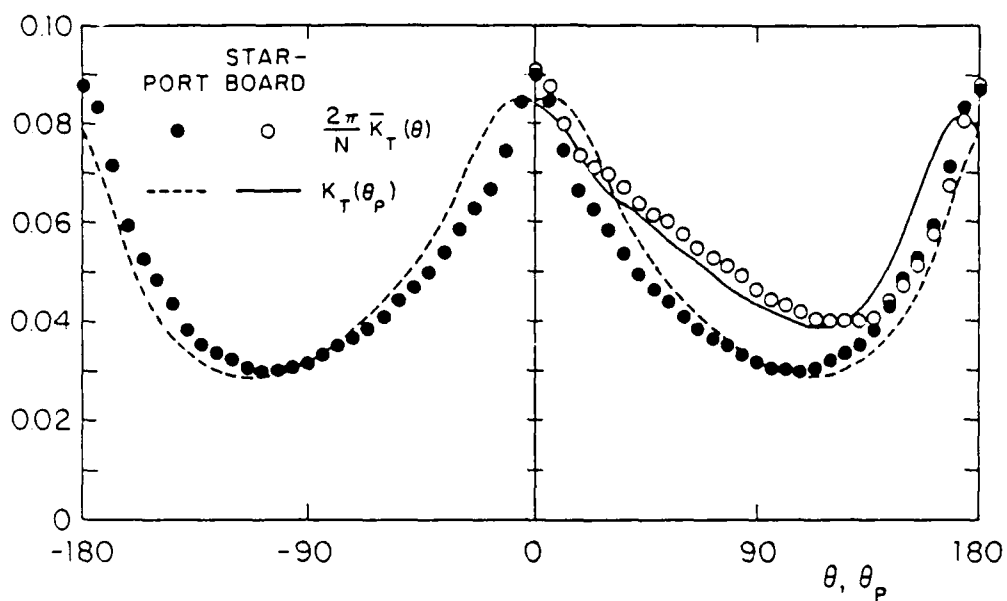
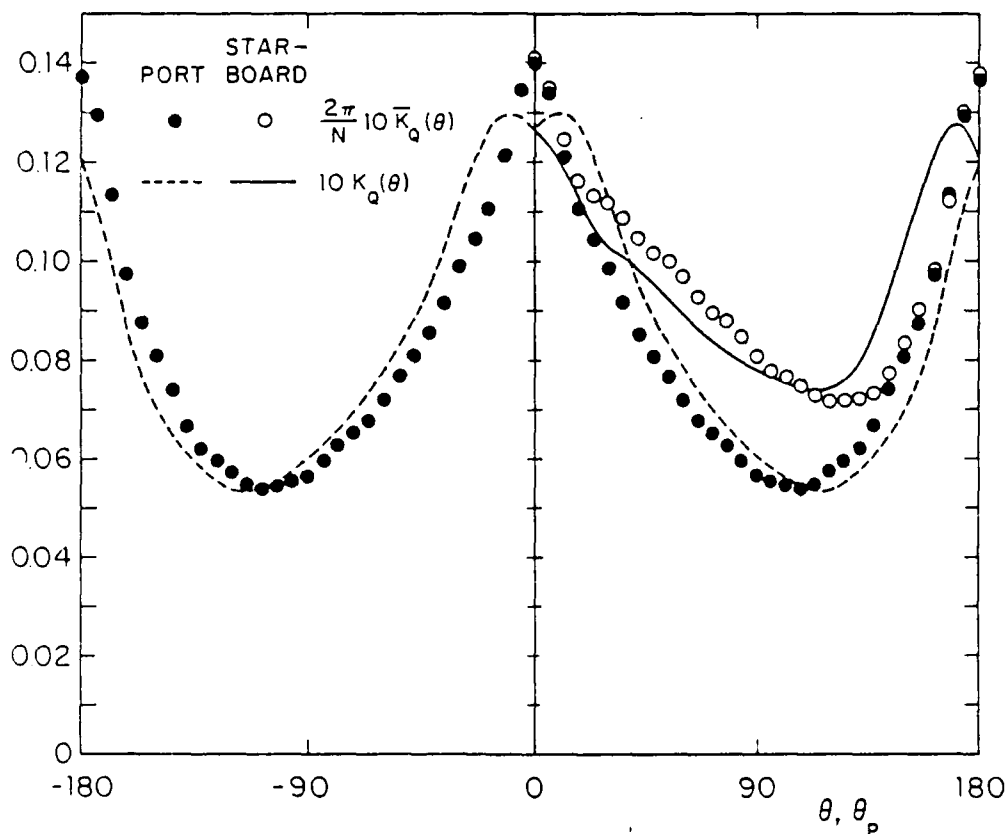


Figure 25. Unsteady blade thrust (nominal inflow).

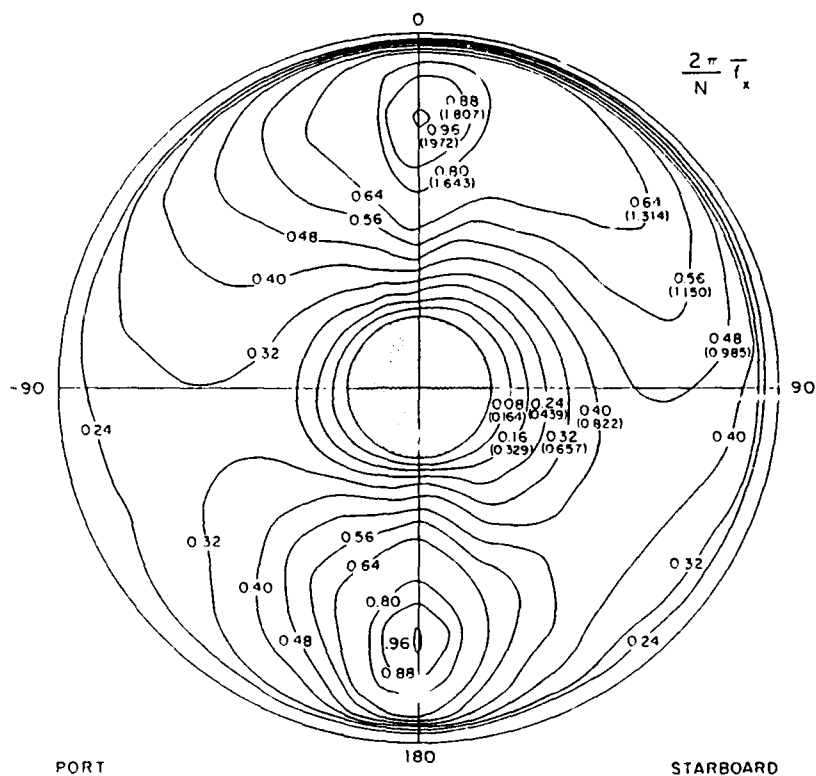


(a) thrust

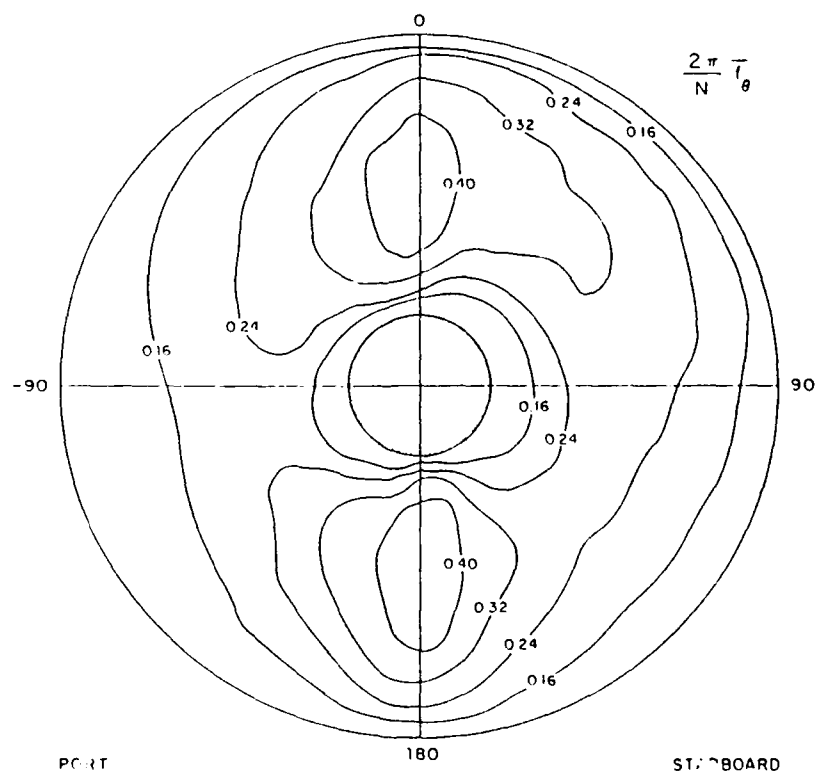


(b) torque

Figure 26. Comparison of unsteady and time-averaged angular variation of blade thrust and torque (nominal inflow).

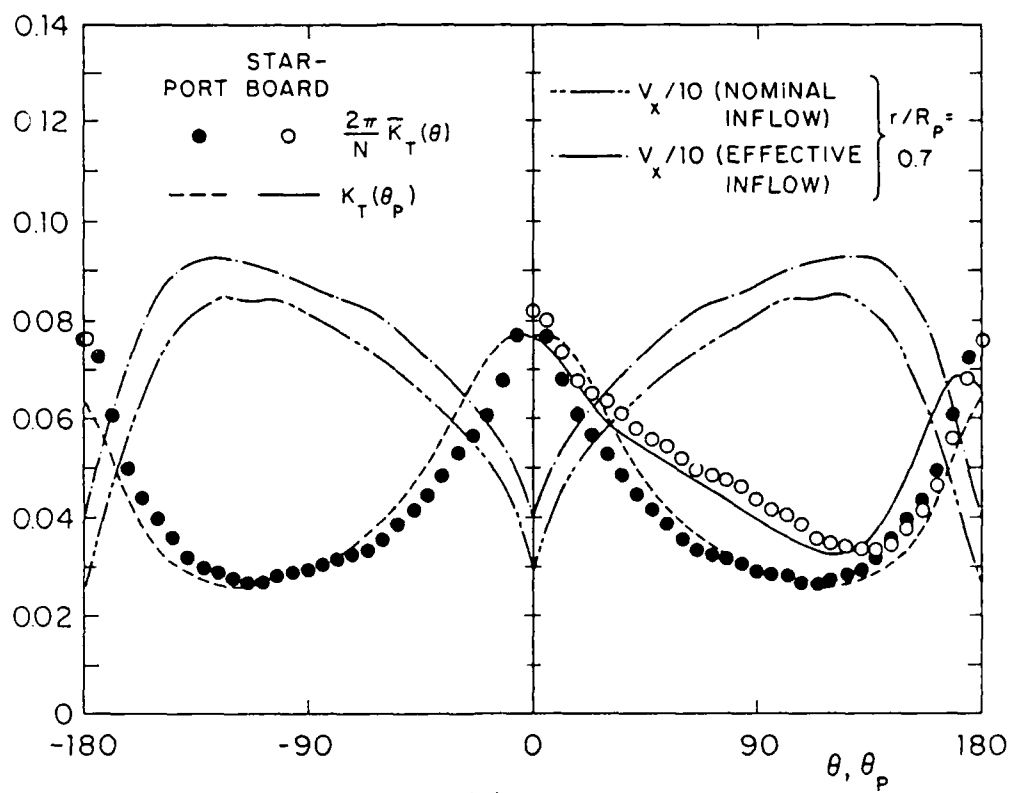


(a) thrust

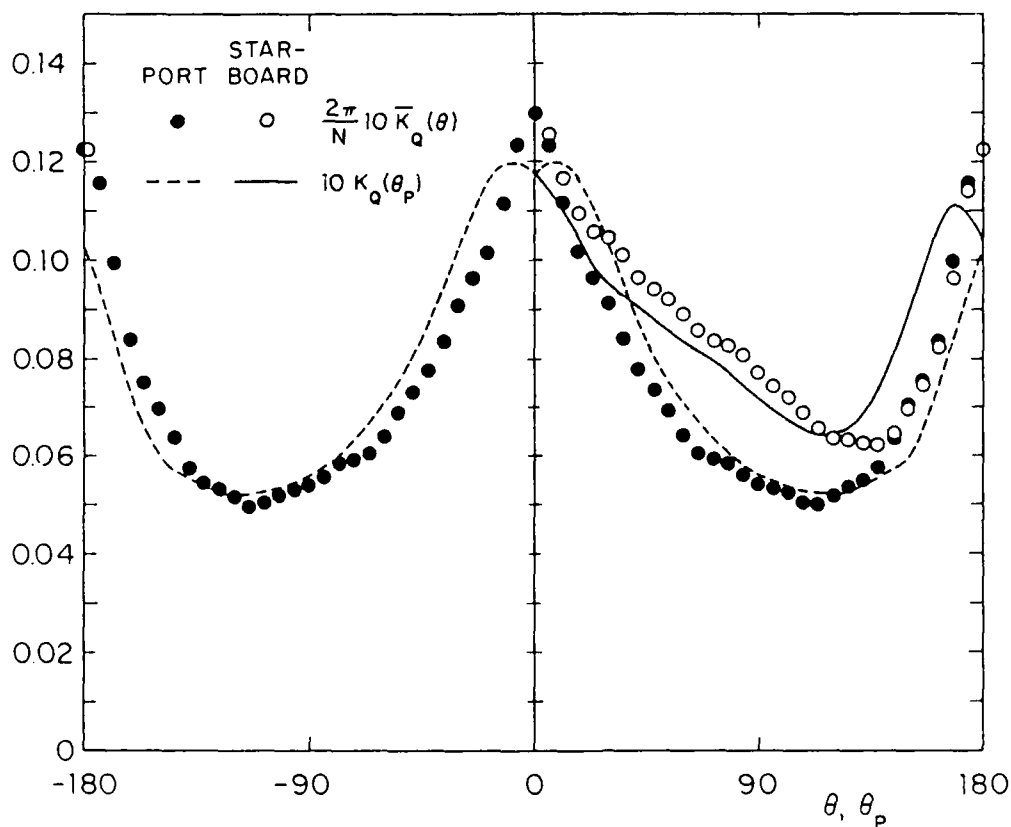


(b) torque

Figure 27. Time-averaged angular and radially varying thrust and torque contours (nominal inflow).

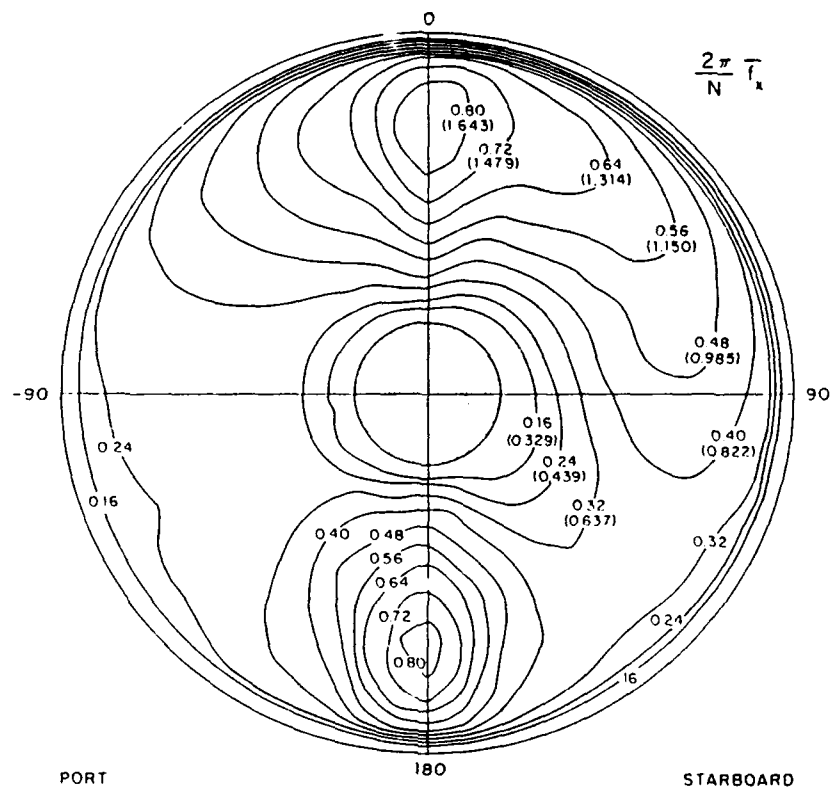


(a) thrust

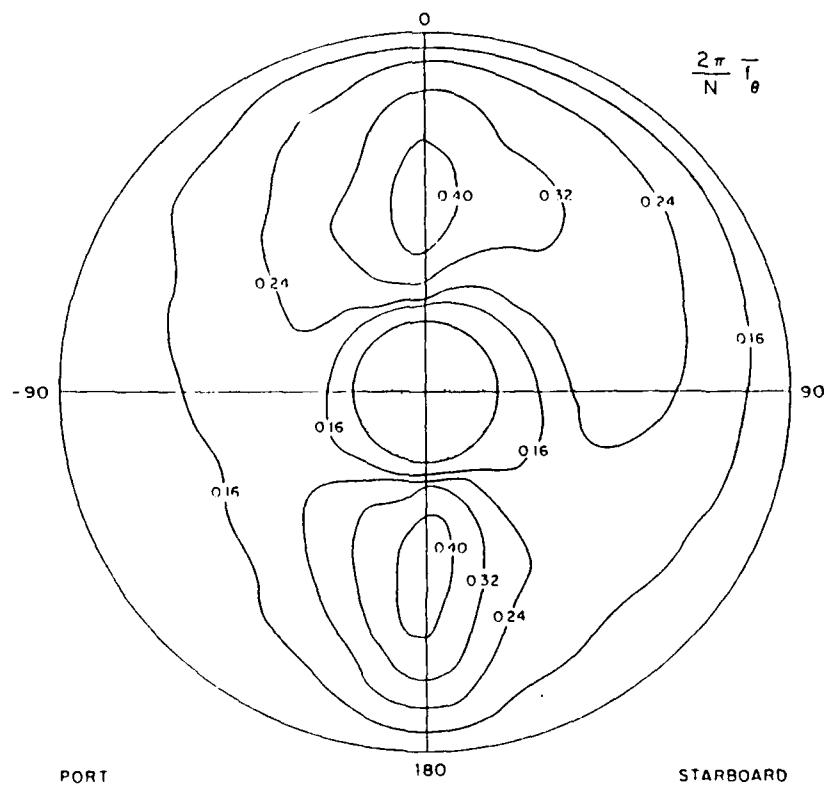


(b) torque

Figure 28. Comprison of unsteady and time-averaged angular variation of blade thrust and torque (effective inflow).



(a) thrust



(b) torque

Figure 29. Time-averaged angular and radially varying thrust and torque contours (effective inflow).

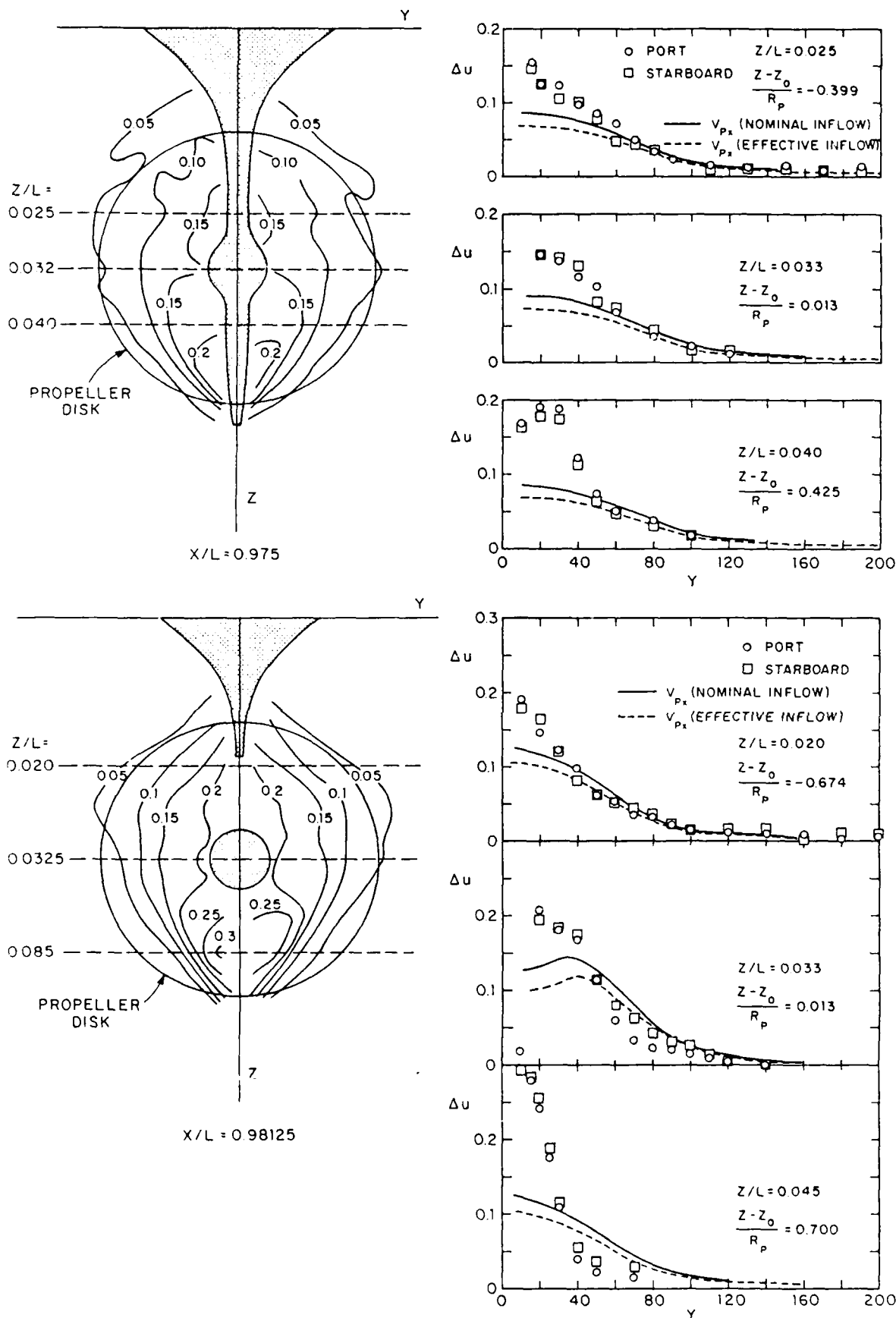


Figure 30. Difference in axial velocity contours between the with- and without-propeller conditions  $\Delta u$  for the region upstream of the propeller.



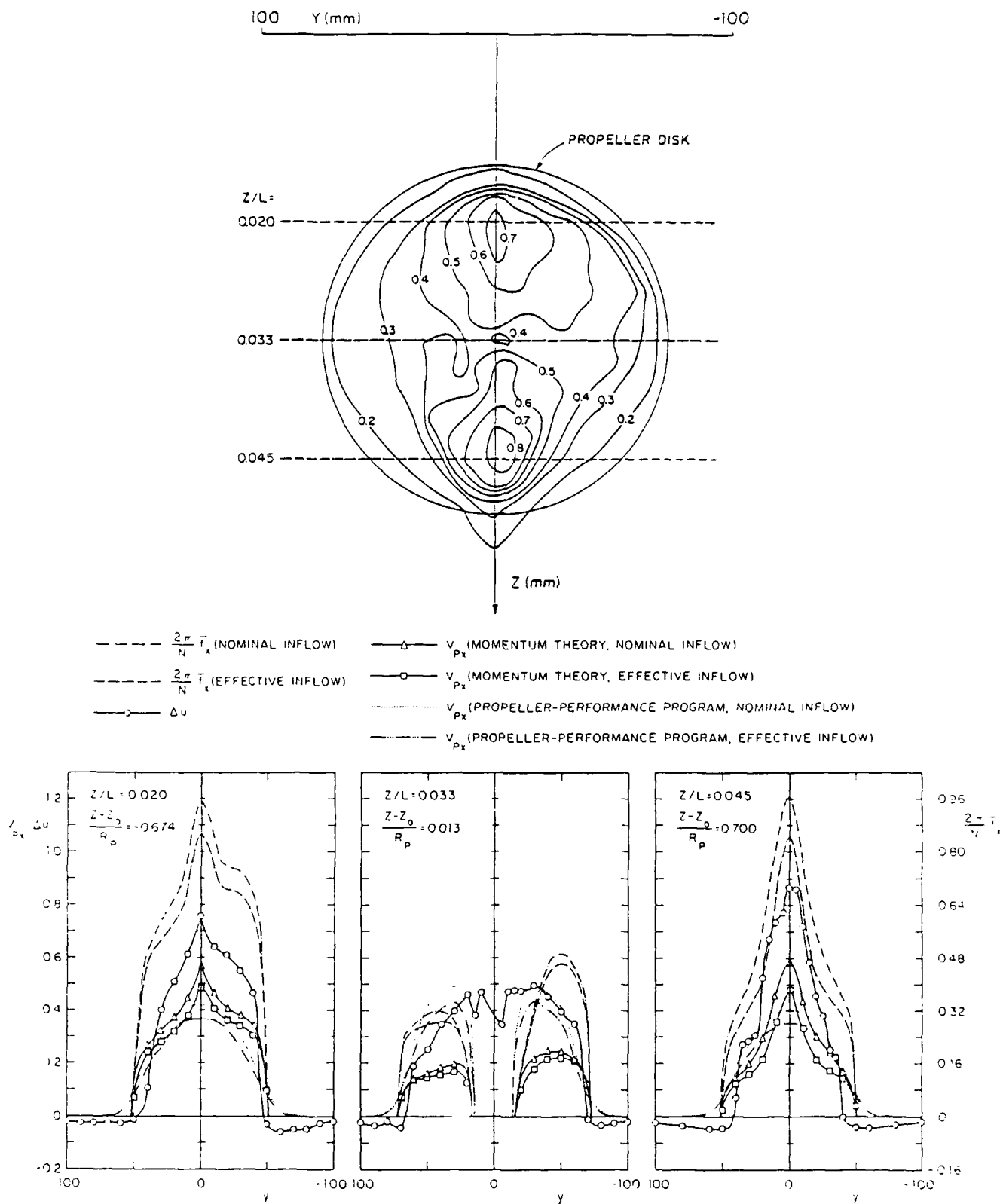


Figure 31. Difference in axial-velocity contours between the with- and without-propeller conditions  $\Delta u$  for the propeller slipstream.

## Appendix I. English Translation of Toda et al. (1987)

### "A Simple Prediction Method for Effective Wake Distribution"

by

Y. Toda<sup>1</sup>, Y. Kasahara<sup>2</sup>, and I. Tanaka<sup>1</sup>

#### Abstract

The interaction between a propeller and a flow field around a full form ship is investigated. A method is presented for the prediction of effective velocity field from measured nominal velocity field. The prediction is made two-dimensionally, with a three-dimensional correction, by use of a modified form of Huang et al.'s method under the assumption that the effects of the vorticity, whose axis is vertical, is dominantly responsible for the distortion of velocity distribution due to propeller suction. The agreement between measured and predicted total velocity distribution with propeller is comparatively good. Characteristics of the effective velocity field for a full form ship are discussed.

#### 1. Introduction

In the flow field around a ship stern where a propeller is operating, there exists an interaction between the viscous flow field and the propeller. The flow field where the propeller is operating cannot be understood as a superposition of propeller induced velocity field and nominal velocity field, which is the inflow velocity distribution at the propeller plane in the absence of the propeller. This is why the strength and the location of the vortices in boundary layer are changed due to propeller suction. At present, the calculation methods for propeller performance, propeller bearing forces, surface forces, and so on are considered to be mostly those taking the velocity distribution at the propeller plane as the input and satisfying the boundary condition by adding induced velocity. Therefore, it is considered that as the input for propeller calculation, effective velocity distribution should be used instead of nominal velocity distribution. Effective velocity field is considered to be the flow field induced by the distorted vorticity distribution in nominal flow field due to propeller suction.

Recently various works on effective velocity have been carried out. In particular, as for axisymmetric flow, a lot of works have been done (for example, [1],[2],[3],[4]) and investigations utilizing the Reynolds equations have also been performed (for example, [5],[6]). As for a simple three dimensional hull form, the authors [7], Sato et al. [8], and others calculated the effective velocity distribution by using an integral method for calculating the boundary layer. As for practical hull forms, Breslin et al. [9], Chen et

---

1 Osaka University

2 Tsu Research Laboratories, Nippon Kokan, K.K.

al. [10], Dyne [11], van Gent [12], and others have shown methods for predicting the effective wake distribution from the nominal velocity distribution by methods extended from the axisymmetric case.

This paper describes a simple method for calculating the effective velocity field from the nominal velocity field by use of a modified form of Huang et al.'s method [1]. The prediction is made two-dimensionally, with a three-dimensional correction under the assumption that the effects of the change of vorticity, whose axis is vertical, is dominantly responsible for the distortion of velocity distribution due to propeller suction. The calculation is made for a full form ship. The calculated velocity distribution with propeller in the region ahead of the propeller is compared with measured results. The effective velocity distribution at the propeller plane is calculated and the difference between the nominal and effective velocity distributions are investigated. The propeller thrust is also calculated using the effective velocity, as well as using the nominal velocity and they are compared with the measured thrust.

## 2. A prediction method for effective velocity distribution

As shown in Fig. 1, we adopt a right-handed Cartesian coordinate system. The x-axis coincides with the propeller axis of revolution and the direction of uniform flow, the y-axis is in the starboard direction, and the z-axis is in the upward direction. Let  $u$ ,  $v$  and  $w$  be the nondimensional velocity components (nondimensionalized by the uniform flow) in the direction of the x, y and z axes, respectively.

In this paper, it is assumed that the effect of the change of vorticity component  $\omega_z$ , whose axis is vertical, is dominantly responsible for the distortion of the velocity distribution due to propeller suction (from the measured flow fields around a full form ship both with and without propeller [13]). Therefore, the change of  $\omega_z$  is mainly considered two-dimensionally for the velocity distribution on a line where  $x$  and  $z$  are constant and, as for the three-dimensional effects, the flow contraction in the  $z$  direction in irrotational flow is taken into account in a similar manner as in a previous paper [7].

First, it is simply shown how Huang et al.'s method [1] for an axisymmetric case transforms for a two-dimensional case. It is assumed that fluid is inviscid but rotational similarly to Huang et al. In the case of axisymmetric flow,  $\omega_\theta/r$  is constant along streamlines, while in the case of two-dimensional flow,  $\omega_z$  is constant along streamlines. The nominal velocity without propeller and the total velocity with propeller are denoted by  $u_n$  and  $u_p$ , respectively. The total velocity is divided into the effective velocity  $u^e$  and the induced velocity  $u_i$  ( $u = u^e + u_i$ ; suffixes are used similarly for  $v$  and  $w$ ). Also, as for the coordinate  $y$ , suffixes  $p$  and  $n$  denote the conditions with and without propeller, respectively. Since  $\omega_z$  is constant on a streamline (see Fig. 2),

$$\frac{\partial u_n}{\partial y_n} - \frac{\partial v_n}{\partial x} = \frac{\partial u_p}{\partial y_p} - \frac{\partial v_p}{\partial x} = \frac{\partial u^e}{\partial y_p} - \frac{\partial v^e}{\partial x} + \frac{\partial u_i}{\partial y_p} - \frac{\partial v_i}{\partial x} \quad (1)$$

is obtained. The induced velocity field is assumed to be irrotational. The usual boundary-layer approximation  $\partial v / \partial x \ll \partial u / \partial y$  is assumed to be valid for both the nominal velocity and the effective velocity. Then Eq. (1) reduces to

$$\frac{\partial u_n}{\partial y_n} = \frac{\partial u_e}{\partial y_p} \quad (2)$$

The massflow condition is written as

$$u_n dy_n = u_p dy_p = (u_e + u_i) dy_p \quad (3)$$

From Eq. (1) and Eq. (3)

$$u_n du_n = (u_e + u_i) dy_p \quad (4)$$

is obtained. Eqs. (3) and (4) are the governing equations for the interaction between the propeller and the stern flow field. If the distributions  $u_n$  and  $u_i$  are given, the distributions of  $u_p$  and  $u_e$  can be determined. (The nominal velocity at the surface is taken to be the extrapolated value of the nominal velocities from near the surface.)

Next, the finite difference form of Eqs. (3) and (4) are discussed. As shown in Fig. 3, if the distribution of  $u_n$  on a cross section of  $x$ -constant is given by the measured one or others, the values at the  $n$  discrete points  $y_{n1}, y_{n2}, y_{n3}, \dots, y_{nn}$  are denoted by  $u_{n1}, u_{n2}, u_{n3}, \dots, u_{nn}$ , respectively. Also for other quantities, the values at discrete points are denoted similarly by second suffixes. Then Eqs. (3) and (4) can be written as

$$(u_{ni} + u_{ni+1})(u_{ni+1} - u_{ni}) = (u_{ei} + u_{ii} + u_{ei+1} + u_{ii+1})(u_{ei+1} - u_{ei}) \quad (5)$$

$$(u_{ni} + u_{ni+1})(y_{ni+1} - y_{ni}) = (u_{ei} + u_{ii} + u_{ei+1} + u_{ii+1})(y_{pi+1} - y_{pi}) \quad (6)$$

Since the boundary-layer approximations are assumed to be valid for the nominal and the effective velocity, the vorticity within the boundary layer does not affect the velocity field outside the boundary layer and it is considered that  $u_e = u_n$  outside the boundary layer. Therefore, if  $y_n$  is taken to be outside the boundary layer, the outside edge condition is written as

$$u_{en} = u_{nn} \quad (7)$$

Or, if the effect of the irrotational flow is taken into account, the outside edge condition is written as

$$u_{en}(y_{pn}) = u_{nn}(y_{nn}) - (u_{pot}(y_{nn}) - u_{pot}(y_{pn})) \quad (8)$$

where,  $u_{pot}$  is the value obtained by potential calculation. The body surface is a streamline. Therefore the inside edge condition is written as

$$y_{nl} = y_{pl} = y_B \quad (9)$$

where,  $y_B$  is the y-coordinate of the body surface or the center plane. By simply changing, Eq. (5) reduces to

$$u_{ni+1}^2 - u_{ni}^2 = (u_{ei+1} + \frac{u_{ii} + u_{ii+1}}{2})^2 - (u_{ei} + \frac{u_{ii} + u_{ii+1}}{2})^2 \quad (10)$$

$$u_{ei} = \sqrt{(u_{ei+1} + \frac{u_{ii} + u_{ii+1}}{2})^2 + (u_{ni}^2 - u_{ni+1}^2)} - \frac{u_{ii+1} + u_{ii}}{2} \quad (11)$$

Therefore, if the induced velocity field is given by some calculation and  $u_{en}$  is given by Eq. (7) or Eq. (8),  $u_{ei}$  can be solved step by step from  $u_{en}$  to  $u_{e1}$ . Eq. (6) is changed to

$$y_{pi+1} = y_{pi} + \frac{(u_{ni} + u_{ni+1})}{u_{ei} + u_{ii} + u_{ei+1} + u_{ii+1}} (y_{ni+1} - y_{ni}) \quad (12)$$

Therefore,  $y_{pi+1}$  can be solved step by step from  $y_{p1}$  to  $y_{pn}$ . Eqs. (11) and (12) are the equations to be solved. However,  $u_{ii}$  is the induced velocity at the position  $y_{pi}$  and  $y_{pi}$  is an unknown quantity till Eq. (12) is solved. Namely,  $y_{pi}$  is unknown when Eq. (11) is solved at first. This is the same about  $y_{pn}$  when Eq. (8) is used. Accordingly at first, induced velocity and others are calculated by assuming  $y_{pi} = y_{ni}$ . After solving Eqs. (11) and (12), the calculated  $y_{pi}$  is used for recalculating the induced velocity and others. The same operation is repeated until a convergence condition is satisfied. The results shown in section 3 are those for five iterations.

Next, the method of taking three-dimensional correction into account is shown. When the above mentioned equations in the two-dimensional case are reviewed, Eqs. (4), (5) and (11) are entirely the same as those of Huang et al.'s method for the axisymmetric case. This is the natural consequence, because Eqs. (4), (5) and (11) represent the condition that there is no pressure difference through vortex layers as shown in Eq. (10), if considering the flow field with discrete vortex layers. Only Eq. (12) which determines the location of a vortex layer from the massflow condition is different from that

of the axisymmetric case. Accordingly, as for the case that the effect of the flow contraction in the  $z$  direction is taken into account, it is sufficient to change Eq. (12) to

$$y_{pi+1} = y_{pi} + \left(\frac{h_{2n}}{h_{2p}}\right) \frac{(u_{ni} + u_{ni+1})}{(u_{ei} + u_{ii} + u_{ei+1} + u_{ii+1})} (y_{ni+1} - y_{ni}) \quad (13)$$

where,  $h_2$  is the streamline interval.  $h_{2p}$  and  $h_{2n}$  are those for a streamline passing through the same points in the region where the influence of the propeller does not exist. A vortex model in the discrete form is shown in Fig. 4. As shown in the figure, the velocity distribution on a line of  $z=\text{constant}$  is represented by the distribution of  $\omega_z$  and the movement in the  $z$  direction of vortex layers due to propeller suction is calculated by potential calculation. At this time,  $h_{2n}/h_{2p}$  corresponds to the change of the length of a vortex filament. Furthermore, precaution must be taken for the fact that the  $z$  coordinate of considering velocity distribution with propeller is different from that without propeller. Actually  $h_{2p}/h_{2n}$  is considered to be a function of  $y$ , but it is assumed to be constant on a line of  $z=\text{constant}$  for simplicity's sake in this discussion. The calculation of  $h_{2p}/h_{2n}$  is carried out in the uniform flow. The uniform flow velocity  $U$  is determined by thrust identity from the calculated thrust and the calculated propeller open-water characteristics similarly to the self propulsion test. That is, at the plane of  $y = D/4$ ,

$$\frac{dz}{dx} = \frac{w_i}{U+u_i} \quad (14)$$

is traced from 2D ahead of the propeller and the movement of the  $z$  coordinate is calculated, where  $D$  is the diameter of a propeller. This is not a streamline, but it is considered that the flow contraction in the  $z$  direction can be represented to some degree by Eq. (14), which is consistent with the fact that the present method is a simple prediction method.

### 3. Predicted results and discussion

#### 3.1. Flow field ahead of propeller

To examine the present method, the total velocity distribution with propeller is predicted from the nominal velocity distribution measured ahead of the propeller, and compared with the measured total velocity distribution with propeller. The experiment was carried out by one of the authors [13]. Principal particulars of the ship model and the propeller are shown in Table 1. The comparison is carried out corresponding to the ship point (ship velocity;  $V = 1.3\text{m/sec}$ , number of revolution;  $n=7.12\text{ rps.}$ ). Yamazaki's method (infinitely bladed theory [14]) is used for the propeller calculation. For the calculation of flow field ahead of propeller, induced velocity field is calculated by using uniform flow  $(1-w_T)V$  ( $w_T$  is the effective wake fraction by thrust identity method) as the input. Calculations are made for two stations S.S.3/8 ( $x=-275\text{mm}$ ) and S.S.1/4 ( $x=-125\text{mm}$ ), where velocity measurements were obtained for both the with- the without-propeller conditions.

First, the flow contraction in the  $z$  direction is not taken into account and the calculation is carried out by use of Eqs. (7), (11) and (12). The examples of the calculated results for station S.S. 3/8 are shown in Fig. 5. In the calculation, the dot-dash lines which smoothly connect the measured nominal velocity  $u_n$  plotted in circles are taken as the input. Then, broken lines of effective velocity  $u_e$  and solid lines of total velocity  $u_p$  are predicted.  $u_p - u_n$  shown with dotted lines represents the velocity increment due to propeller suction and the difference between  $u_p - u_n$  and the propeller induced velocity ( $u_e - u_n$ ) is considered to show the interaction between the propeller and the stern flow field. Since the induced velocity does not change a lot, it is considered that the interaction is large in the part of large  $u_p - u_n$ . In fig. 5, a fairly good agreement between measured and calculated total velocity distribution is obtained. It is found that the large effect of propeller suction is observed in the predicted results as well as in the measured results though the induced velocity is very small in the station S.S.3/8. In particular, the large  $u_p - u_n$  due to propeller suction is predicted well in the part of large velocity gradient on the outside of the plateau-like portion of the velocity. It is considered that the large velocity increment due to propeller which cannot be predicted well by an ordinary boundary layer calculation [13] is predicted well by Eqs. (7), (11) and (12). Fig. 7 shows how the effect of propeller suction appears due to velocity distribution in  $y$  direction. Fig. 7(a) shows the result for the velocity distribution around a fine ship like the Wigley model. It is found similarly to the previous paper [7] that the velocity increment becomes larger as the point gets near to the surface. Fig. (b) shows the case of larger velocity gradient (vorticity  $\omega_z$ ) as compared with (a). The velocity increment is larger than Fig (a) and the effective velocity distribution becomes close to the total velocity distribution. However, it is the same that the velocity increment becomes larger as the point gets near to the surface. Fig. (c) shows the results for the example of the velocity distribution around a full form ship. It is found that the velocity increment distribution is considerably different from the case of (a) and (b). The examples of the calculated results for the station S.S.1/4 are shown in Fig. 7. It is found that the part of large velocity gradient on the outside of the plateau-like portion of the velocity moves too inwardly and the influence of propeller suction is predicted to be too strong. However, it seems that the qualitative tendency of the velocity increment distribution agrees well with experimental results. In order to show clearly this feature, the comparison between measured and predicted velocity increment distribution is shown in Fig. 8 and Fig. 9. As shown in Fig. 8, the predicted result agrees well with measured ones such as in Fig. 5 in S.S. 3/8, where the induced velocity is small. As for the result in S.S.1/4 shown in Fig. 9, it seems that the predicted position of the region where the velocity increment is remarkable agrees well with measured one, though the magnitude of velocity increment is larger by about 0.1 than the measured one. Therefore, it is considered that even the simple method of using Eqs. (7), (11) and (12) can be used for judging whether the ratio  $(1-W_T)/(1-W_n)_{\text{mean}}$  is large or small owing to the characteristic of nominal velocity distribution ( $(1-W_n)_{\text{mean}} = (U_n)_{\text{mean}}$ ; the volume mean of nominal velocity in the propeller disk,  $W_T$ ; effective wake fraction).

Next, Fig. 10 shows the results for the station S.S.1/4 predicted by the present method using Eqs. (8), (11) and (12), in which the effect of the flow

contraction in  $z$  direction and the change in potential wake for the outside edge condition are taken into account. The potential velocity is calculated by the Hess-Smith method. As shown in Fig. 10, a fairly good agreement between measured and predicted total-velocity distribution near the propeller axis is obtained as a whole, though disagreement is somewhat large at some places near the plateau-like portion of the velocity. The velocity contour curves in S.S.1/4 are shown in Fig. 11. On the right side of the figure, the comparison between the measured and predicted total velocity distribution is shown. On the left side, the comparison between the measured nominal velocity distribution and the predicted effective velocity distribution is shown. From the figure of the total velocity, the measured and the predicted results agree fairly well with each other as a whole, although the predicted velocity is somewhat higher than the measured one near the upper and lower ends of the propeller disk. That the effect of the flow contraction in the  $z$  direction is calculated in the uniform flow of  $(1-w_T)V$  for simplicity's sake and the irrotational velocity component in the boundary layer is not taken into account in the similar form to that of the induced velocity when deriving Eqs. (1)-(4) is considered to be the reason for the discrepancy. It also seems that the neck-like portion of the nominal velocity distribution owing to the cross flow appears too strongly in the predicted total velocity distribution. Other methods seem to be necessary for the improvement in this part as the effect of the cross flow is not taken into account. However, it is considered that the effect of propeller suction for the flow field around a full form ship is predicted fairly well as a whole by present method, if considering that the results in Fig. 10 and Fig. 11 are predicted by the method assuming that the dominant effect of propeller suction on the stern flow field can be treated two-dimensionally. From the left figure of Fig. 11 and Fig. 10, the difference between the nominal and the calculated effective velocity distribution is investigated. It is observed that the contour curves of the effective velocity distribution are displaced toward the center plane as compared with those of the nominal velocity distribution as a whole and the velocity is increased from the nominal one to the effective one, but not uniformly. Namely, there are the regions where the nominal and the effective velocity are hardly different and the regions where the difference between them is large. Therefore, it is found that the effective velocity distribution by present method is considerably different from the distribution determined from the nominal velocity distribution being multiplied by  $(1-w_T)(1-w_n)_{\text{mean}}$ , which has been used frequently for propeller calculations.

Next, in order to investigate whether the information can be obtained or not about the change of velocity in a cross section  $(V_e - V_n, W_e - W_n)$ , the distortion of the longitudinal vorticity distribution due to propeller suction is predicted. The longitudinal vorticity with propeller is predicted from the measured one without propeller by the method taking into account only the decrease of the cross sectional area and the change of position of stream tubes, which are obtained as the results of prediction of the propeller effect for the velocity in  $x$  direction by present method. Namely, if the longitudinal vorticity  $\omega_{xn}$  without propeller is known, the longitudinal vorticity  $\omega_{xp}$  with propeller is predicted by

$$\omega_{xp} \left( \frac{y_{pi} + y_{pi+1}}{2} \right) = \frac{h_{2n}}{h_{2p}} \frac{y_{ni-1} - y_{ni}}{y_{pi+1} - y_{pi}} \cdot \omega_{xn} \left( \frac{y_{ni} + y_{ni+1}}{2} \right) \quad (15)$$



where the parenthesized terms show the position. The comparison of the predicted and measured longitudinal vorticity is shown in Fig. 12. The predicted results agree well with measured ones with propeller as a whole, except near the surface. Eq. (15) is able to predict the increase of the peak value, the movement of the peak position and the tendency that the width of vorticity distribution becomes narrow when the propeller is operating. But, it is found that the distribution is contracted somewhat excessively toward the surface on the outside of the peak. The contour curves of the predicted vorticity distribution with propeller is compared with the measured vorticity distributions with and without propeller in Fig. 13. It also seems that the prediction method is able to predict the peak value and position to some extent. Therefore, it is considered that the information regarding  $V_e - V_n$ ,  $W_e - W_n$  can be obtained to some degree by present method from the difference of the velocity induced by  $\omega_{xn}$  and  $\omega_{xp}$ .

### 3.2 Effective velocity distribution on propeller plane

The effective velocity distribution on the propeller plane is predicted from the measured nominal velocity distribution. In this calculation, iterative calculation is needed to calculate the strength of the bound vortex in the effective velocity. The induced velocity is calculated at the first iteration by using the nominal velocity distribution as the input and thereafter the predicted effective velocity distribution is used as the input to recalculate the induced velocity. The same operation is repeated until a convergence condition is satisfied. In this paper, four iterations were needed. Since  $y_B$  is taken as the center line in Eq. (9) and the calculation is carried out only for starboard side of the ship, the induced velocity at the position  $D/4$  ahead of the propeller is used. The comparison between the measured nominal and the predicted effective velocity distribution is shown in Fig. 14. The right side is the measured nominal velocity distribution used as the input. (Measurement was carried out for the same ship and same advance speed by Tanaka et al. [15], but the data analysis method for the five-hole pitot tube is somewhat different from that of Kasahara [13]). The left side is the predicted effective velocity distribution. It is found similarly to 3.1 that the contour curves of the effective velocity distribution are displaced toward the center plane as compared with those of the nominal velocity distribution as a whole and the velocity is increased from the nominal one to the effective one, but not uniformly. The velocity increment from the nominal to the effective velocity is large particularly on the outside of the plateau-like portion of the velocity. When focusing on the propeller disk, the part of large velocity gradient is hardly in it in the case of the nominal velocity distribution, while high velocity region enters into it in the case of the effective velocity distribution. For reference, the volume mean of effective velocity is compared with that of the nominal velocity and the mean inflow velocity from the self-propulsion test on the basis of the thrust-identity method in Table 2. The calculated thrust by using respective velocity distributions as the input are also shown in Table 1. It is found that the present method is able to predict the tendency in the change of the flow field due to propeller. But the velocity increment from the nominal velocity to effective one is considered to be predicted somewhat excessively. Since the predicted

total velocity is somewhat higher than the measured one at some places in the results shown in 3.1, the reason for the slightly excessive prediction in this section is considered to be similar to that discussed in 3.1. However, as the nominal velocity distribution was measured very much before the self propulsion test, further discussion is withheld. It is considered that the change from the nominal velocity to the effective one is predicted to some degree from the results in 3.1 and in Table 2. Therefore, in order to investigate the characteristics of the effective velocity distribution, the distributions of the circumferential mean nominal and effective velocity in the radial direction are shown in Fig. 15 and the distributions of nominal and effective velocity in circumferential direction at three  $r/R$  are shown in Fig. 16 ( $r$ ; distance from the propeller axis,  $R$ ; propeller radius). From Fig. 15, it is found that the circumferential mean of the nominal velocity varies gently in the radial direction, and the circumferential mean of the effective velocity is increased as a whole due to propeller suction from that of the nominal velocity, especially the velocity increment is large near the propeller hub and the blade tip. In particular, near the blade tip, the velocity increment is large by pulling the high velocity region into the propeller disk as mentioned about Fig. 14. Therefore, the predicted velocity increment distribution due to propeller for the full form ship is different from that for a body of revolution [4] and that for a simple Wigley model [7]. Though the propeller is relatively small in the ship model used in this paper and the high velocity region of nominal velocity distribution on the outside of the plateau-like portion hardly enters into the propeller disk, it is considered that the tendency of the large velocity increment being observed on the outside of the plateau-like portion is the same for the full form ship having a larger propeller. Therefore, it is considered that the tendency of change from the nominal velocity distribution to the effective velocity distribution for a full form ship is considerably different from that for a body of revolution or a fine ship. Also at  $r/R = 0.9813$  near the blade tip in Fig. 16, the effective velocity is remarkably large as compared with the nominal velocity in the region  $60 < \theta < 150$  and the unevenness of the effective velocity distribution in circumferential direction is increased from that of the nominal velocity. This phenomenon for the full form ship is different from that for a simple Wigley model, in which the velocity increment from the nominal velocity to the effective one becomes larger as the point gets near to the surface.

#### 4. Conclusion

The distortion of stern flow field around a full form ship due to propeller suction is investigated. The effect of propeller suction is predicted by a modified form of Huang et al.'s method under the assumption that the effect of the change of vorticity, whose axis is vertical, is dominantly responsible for the distortion of velocity distribution due to propeller suction. The conclusions are as follows.

- (1) The simple prediction method in this paper is able to properly represent the effects due to propeller suction observed in the measured results.
- (2) The change of longitudinal vorticity distribution can be predicted by taking into account the decrease of the cross-sectional area and the change of position of stream tubes, which appear in present prediction.
- (3) The effective velocity around a full form ship is remarkably increased in the region of large velocity gradients on the outside of the plateau-like

portion of the velocity from the nominal velocity. From this fact, the unevenness of the effective velocity distribution in circumferential direction is increased from that of the nominal velocity near the blade tip around a full form ship.

#### Acknowledgements

The authors wish to express their hearty appreciation to Prof. T. Suzuki and Dr. K. Matsumura, Osaka University, for their valuable discussions. Thanks are also extended to Mr. J.F. Perles, Osaka University, who carried out a part of the calculation. The authors also express appreciations to the members of Tsu Laboratories, Nippon Kokan K.K., for their cooperation. Some portion of this study was financed by the Grant-in-aid for Scientific Research of the Ministry of Education, Science and Culture. By remarking it here, the authors wish to express their appreciation.

#### References

- [1] T.T. Huang, H.T. Wang, N. Santelli and N.C. Groves: Propeller/Stern Boundary Layer Interaction on Axisymmetric Bodies: Theory and Experiment, DTNSRDC Report 76-0113 (1976).
- [2] T. Nagamatsu and K. Tokunaga: Prediction of Effective Wake Distribution for Body of Revolution, Journal of the Society of Naval Architects of Japan, Vol. 143 (1978).
- [3] G. Dyne: A Design Method for Wake Vorticity Adapted Propeller in a Frictional Wake, Publ. No. 91 of the Swedish State Shipbuilding Experimental Tank (1981).
- [4] Y. Toda, I. Tanaka and Y. Iwasaki: Distortion of Axisymmetric Boundary Layer due to Propeller Suction, J. Kansai Soc. Naval Arch. Japan, No. 185 (1982).
- [5] L.D. Zhou and J.L. Yuan: Calculation of the Turbulent Flow around the Stern and in the Wake of a Body of Revolution with the Propeller in Operation, 15th ONR Symp. Naval Hydrodynamics, Hamburg (1984).
- [6] F. Stern, V.C. Patel, H.C. Chen and H.T. Kim: The Interaction between Propeller and Ship-Stern Flow, Osaka Inter. Colloquium on Ship Viscous Flow, Osaka (1985).
- [7] Y. Toda, I. Tanaka, H. Sugioka and H. Mori: Distortion of Three-Dimensional Boundary Layer due to Propeller Suction, J. Kansai Soc. Naval Arch. Japan, No. 192 (1984).
- [8] T. Sato and T. Nagamatsu: Calculation of Effective Wake Distribution of a Simple Hull Form, Journal of the Society of Naval Architects of Japan, Vol. 160 (1986).
- [9] J.P. Breslin, R.J. van Houten, J.E. Kerwin and C.-A. Johnsson: Theroetical and Experimental Propeller Induced Hull Pressure Arising from Intermittent Blade Cavitation, Loading and Thickness, SNAME Transaction, Vol. 90 (1982).
- [10] H.-H. Chen and C.Y. Ng Raymond: A Computational Method for the Prediction of Nonaxisymmetric Effective Velocity Field, Inter. Symp. on Propeller and Cavitation, Wuxi (1986).
- [11] G. Dyne: On the Interaction between a Propeller and a Non-Symmetrical Wake, Inter. Symp. on Propeller and Cavitation, Wuxi (1986).
- [12] W. Van Gent: A method of Propeller-Ship Wake Interaction, Inter. Symp. on Propeller and Cavitation, Wuxi (1986).

- [13] Y. Kasahara: Experimental Investigation of the Influence on the Stern Flow Field due to the Operating Propeller, J. Kansai Soc. Naval Arch. Japan, No. 202 (1986).
- [14] R. Yamazaki: On the Propulsion Theory of Ships on Still Water-Improved Theoretical Method-, Memoirs of the Faculty of Engineering, Kyushu University, Vol. 37, No. 1 (1977).
- [15] I. Tanaka et al.: Investigation of Scale Effects on Wake Distribution Using Geosim Models, J. Kansai Soc. Naval Arch. Japan, No. 192 (1984).

Table. 1 Principal Dimension of model

SHIP	L <sub>pp</sub>	12 m
	B	2.182 m
	d	0.726 m
	C <sub>b</sub>	0.837
	R <sub>n</sub>	$1.64 \times 10^7$
PROPELLER	D	0.301 m
	Pitch ratio	0.6155
	EAR	0.6050
	Boss ratio	0.1606

Table 2 Comparison of thrusts and mean velocity (n=7.12 rps)

input velocity distribution	nominal velocity $U_n$	effective velocity $U_e$	uniform flow $(1-w_1)V$
thrust	8.67	7.77	8.05

	$[U_n]_V$	$[U_e]_V$	$1-w_1$	$[U_n]_{0.7R}$	$[U_e]_{0.7R}$
mean velocity	.393 (.382)*	.494	.461	.388	.459

[ ]<sub>V</sub> denotes volume mean of velocity distribution

[ ]<sub>0.7R</sub> denotes mean velocity of 0.7R

\* is the  $[U_n]_V$  calculated at NKK

$w_1$  denotes effective wake fraction by thrust identity

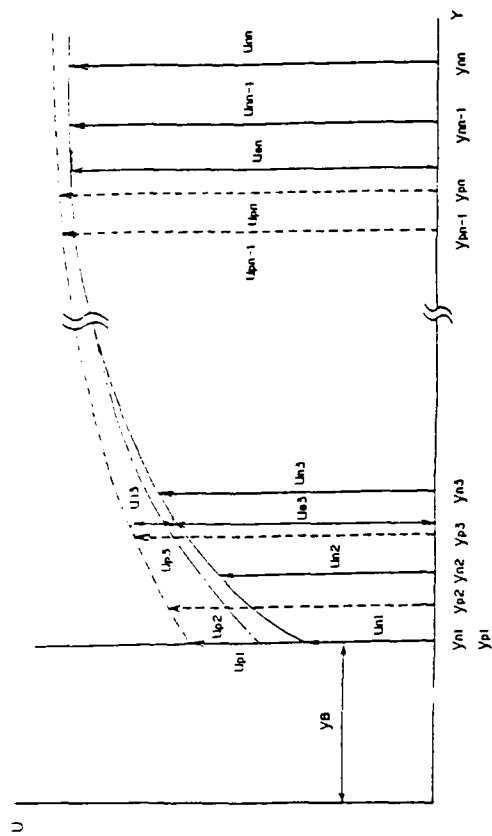


Fig. 3 Illustration of finite difference form

Fig. 1 Coordinate system

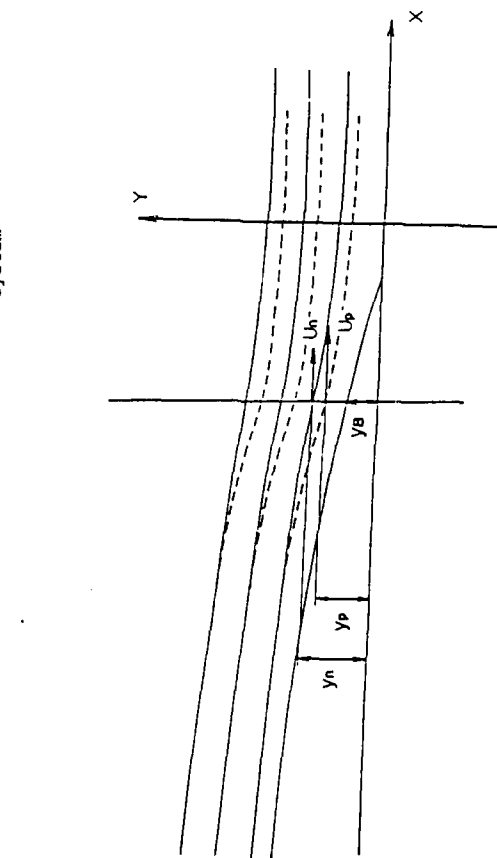
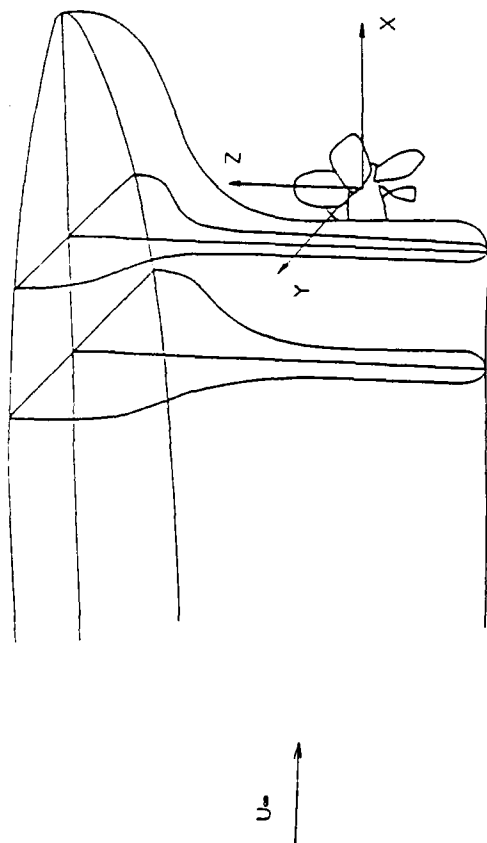


Fig. 2 Definition sketch for propeller stern boundary layer interaction

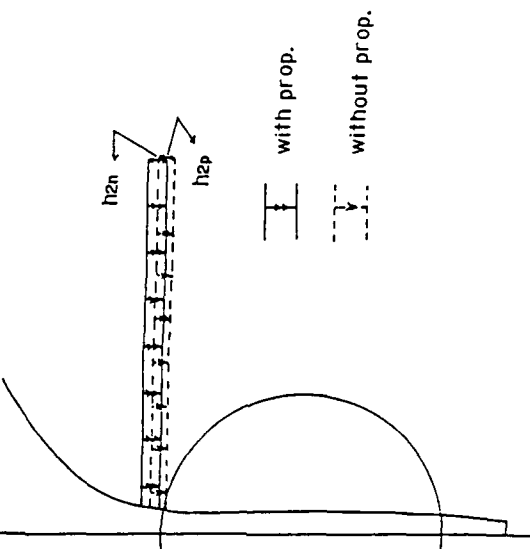


Fig. 4 Illustration of vortex model

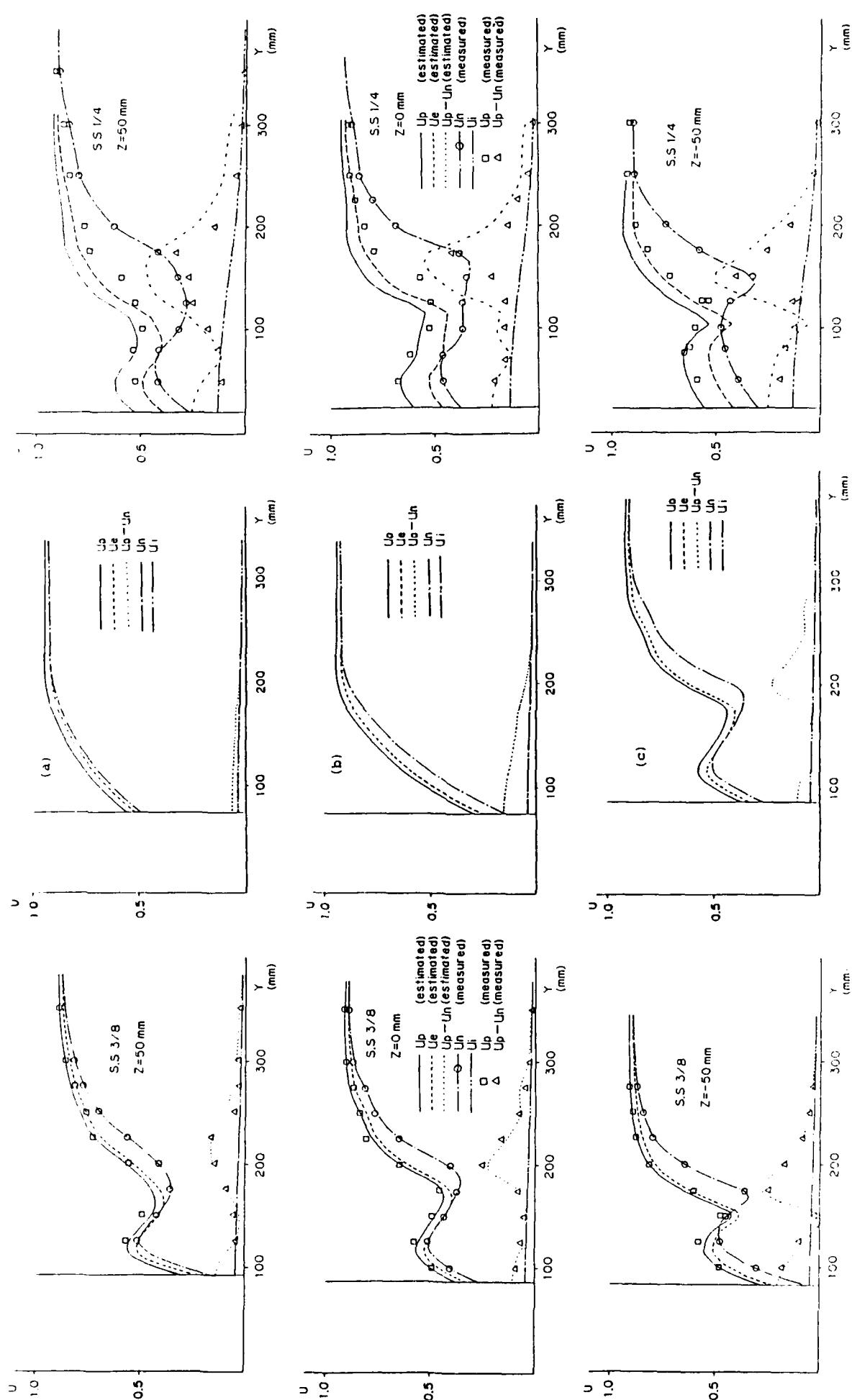


Fig. 8 Comparison of velocity distribution

Fig. 9 Comparison of velocity distribution

Fig. 10 Comparison of velocity distribution

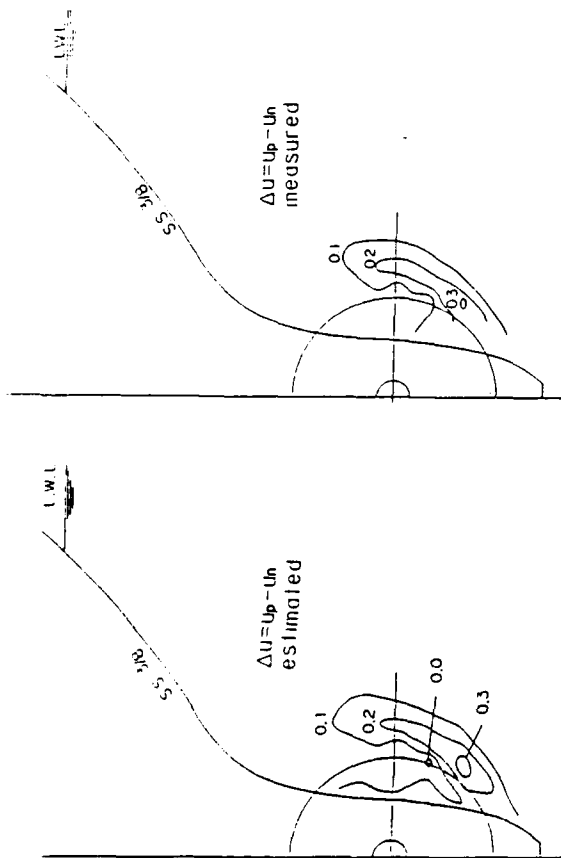


Fig. 8 The difference of magnitude between total and mean velocities

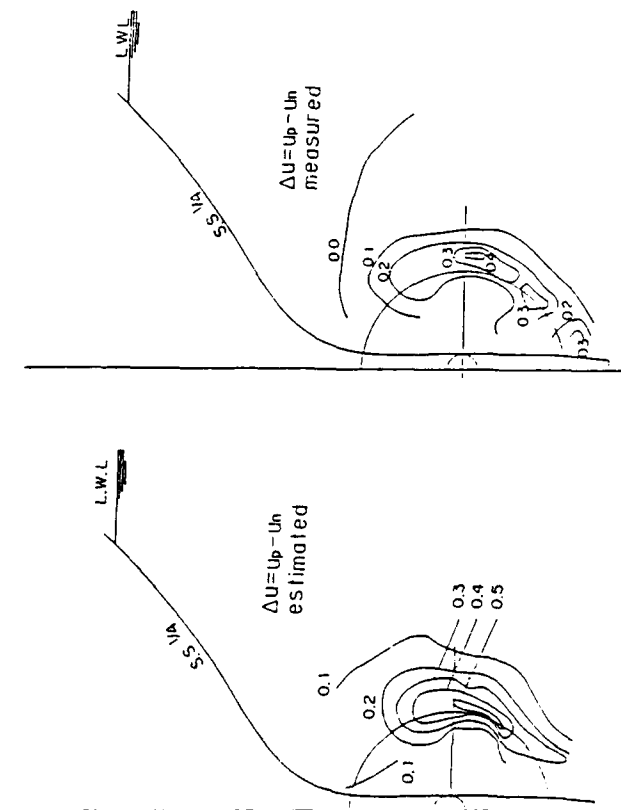


Fig. 9 The difference of magnitude between total and mean velocities

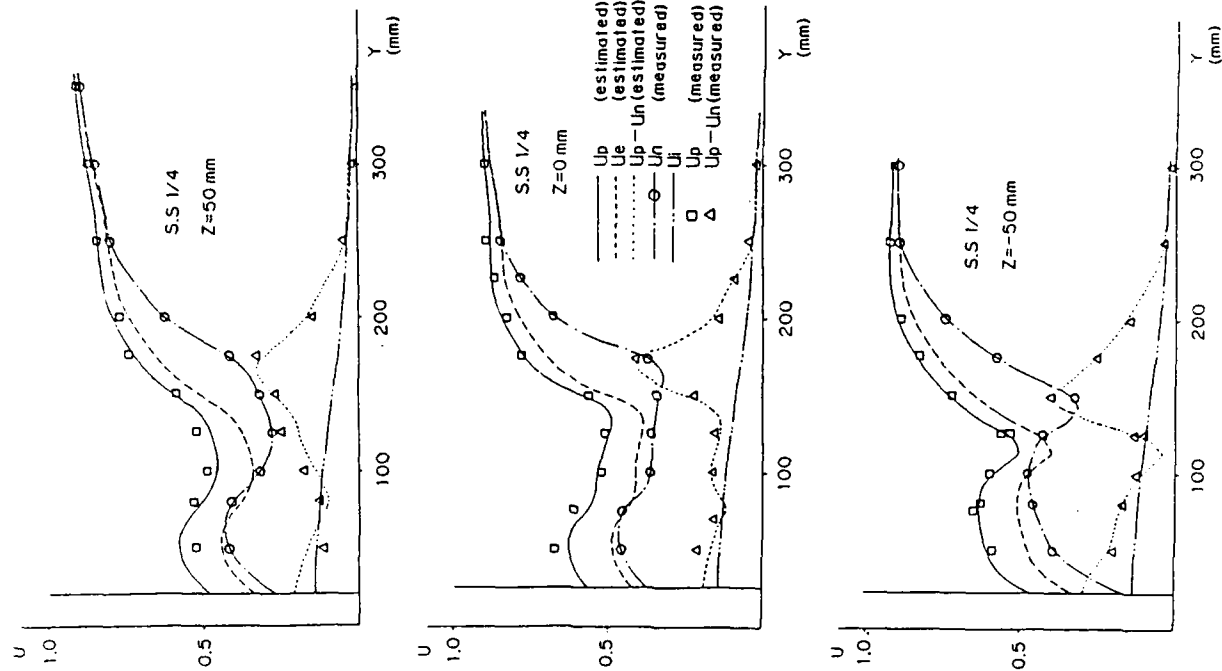


Fig. 10 Comparison of velocity distribution



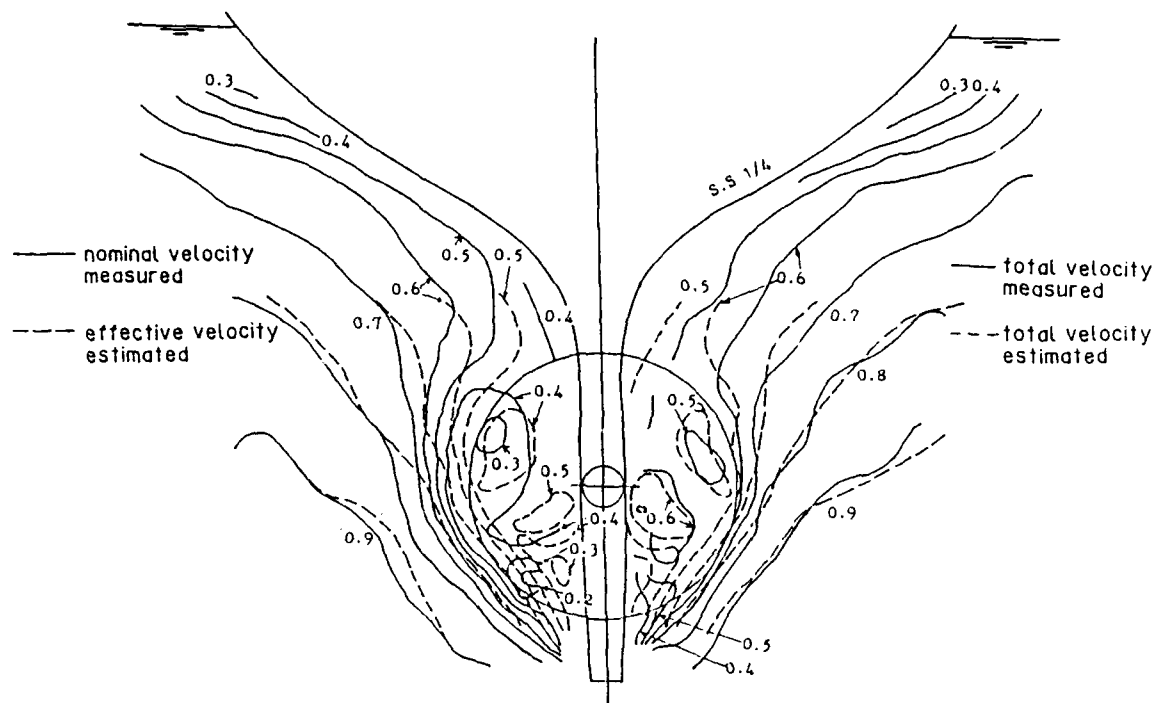


Fig. 11 Comparison of velocity distribution

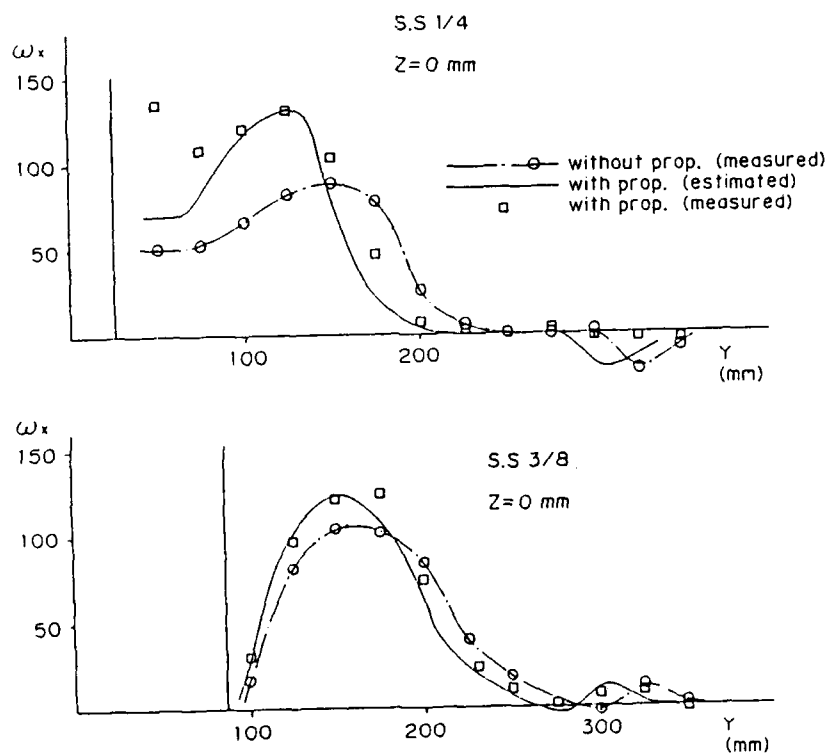


Fig. 12 Comparison of longitudinal vorticity distribution

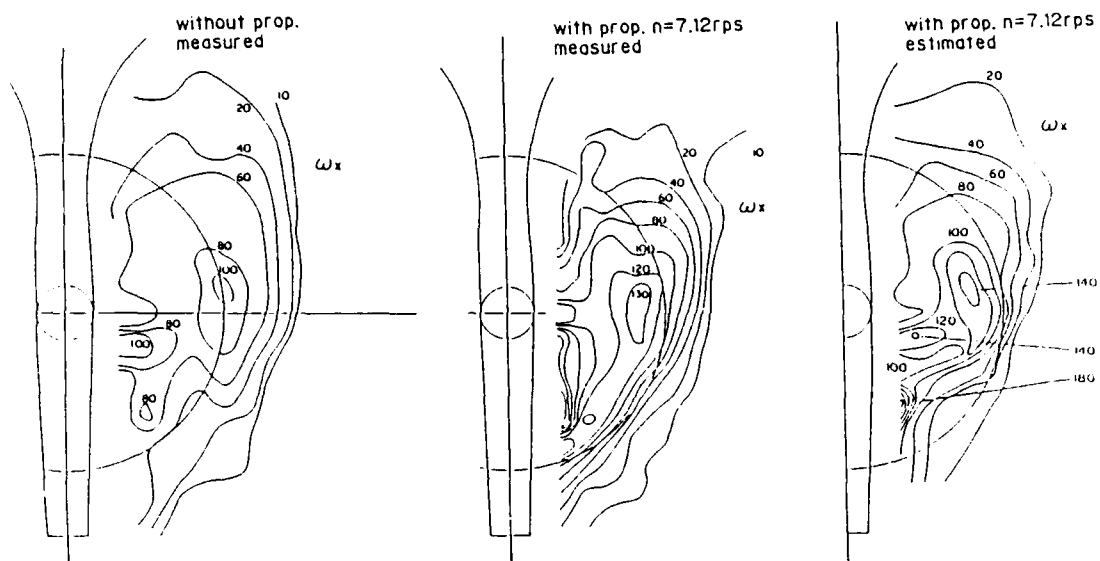


Fig. 13 Comparison of longitudinal vorticity distribution

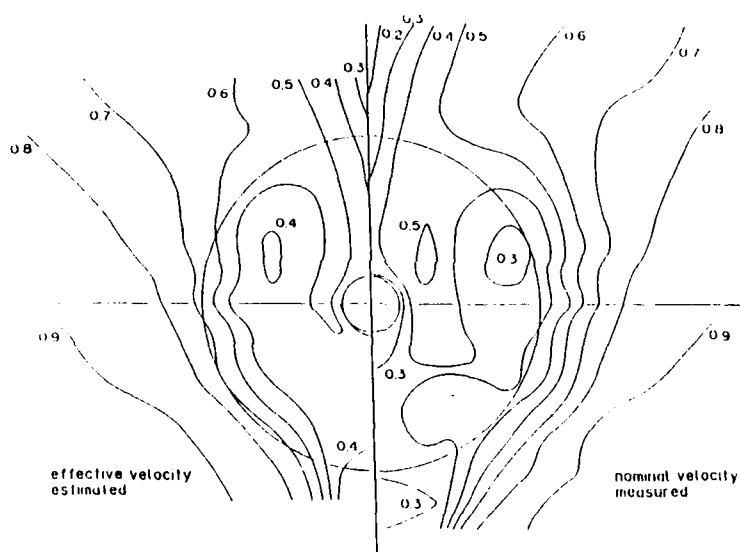


Fig. 14 Comparison of velocity distribution

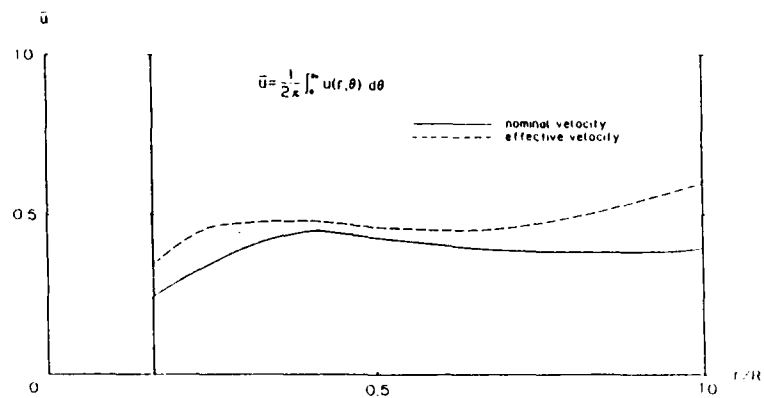


Fig. 15 Comparison of circumferential mean nominal and effective velocity profile

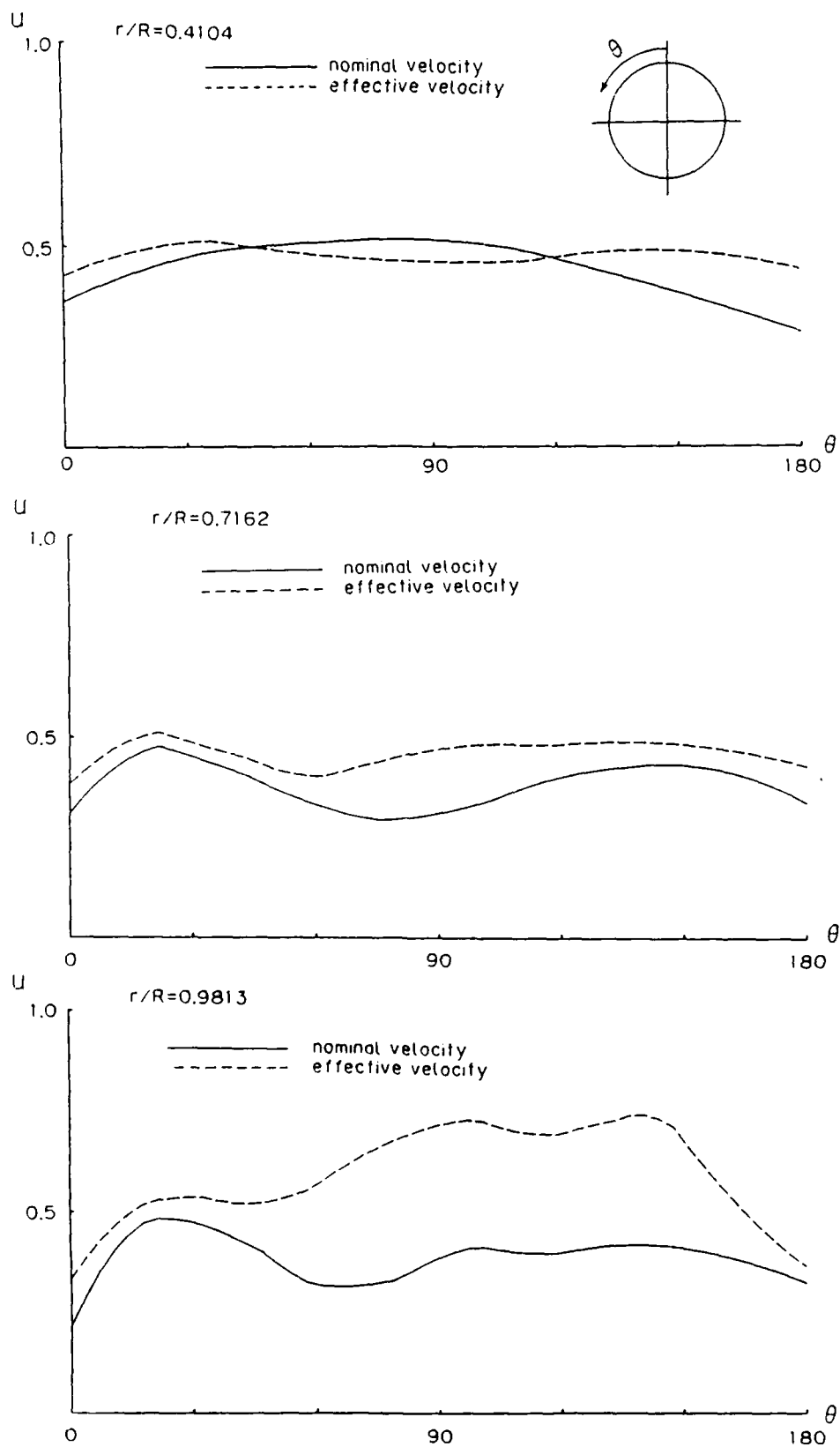


Fig. 16 Comparison of nominal and effective circumferential velocity distribution

## ONR Distribution List

Defense Technical Information Center  
Information Facility  
Alexandria, Virginia 22314

Technical Library  
Naval Coastal System Center  
Panama City, Florida 32401

Office of Naval Research  
Code 1132F  
800 North Quincy Street  
Arlington, Virginia 22217-5000

Office of Naval Research  
Code 1215  
800 North Quincy Street  
Arlington, Virginia 22217

Professor Bruce Johnson  
U.S. Navy Academy  
Hydromechanics Laboratory  
Annapolis, Maryland 21402

Library  
U.S. Naval Academy  
Annapolis, Maryland 21402

Technical Library  
Webb Institute of Naval Architecture  
Glen Cove, New York 11542

Library  
Stevens Institute of Technology  
Davison Laboratory  
Castle Point Station  
Hoboken, New Jersey 07030

R.E. Gibson Library  
The Johns Hopkins University  
Applied Physics Laboratory  
Johns Hopkins Road  
Laurel, Maryland 20810

NASA Scientific and Technical  
Information Facility  
P.O. Box 8757  
Baltimore/Washington Int'l Airport  
Maryland 21240

Librarian  
University of California  
Department of Naval Architecture  
and Offshore Engineering  
Berkeley, California 94720

Technical Information Center  
David Taylor Research Center  
Code 522.1  
Bethesda, Maryland 20084

The Society of Naval Architects  
and Marine Engineers  
601 Pavonia Avenue  
Jersey City, New Jersey 07306

Technical Library  
Naval Coastal System Center  
Philadelphia Division  
Philadelphia, Pennsylvania 19112

Editor  
Applied Mechanics Review  
Southwest Research Institute  
8500 Culebra Road  
San Antonio, Texas 78206

Technical Library  
Naval Ocean Systems Center  
San Diego, California 92152

Lorenz G. Straub Library  
University of Minnesota  
St. Anthony Falls Hydraulic Lab.  
Minneapolis, Minnesota 55414

Library  
Naval Postgraduate School  
Monterey, California 93940

Technical Library  
Naval Underwater Systems Center  
Newport, Rhode Island 02840

Engineering Societies Library  
345 East 47th Street  
New York, New York 10017

Librarian Station 5-2  
Coast Guard Headquarters  
NASSIF Building  
400 Seventh Street, SW  
Washington, D.C. 20540

Library of Congress  
Science and Technology Division  
Washington, D.C. 20540

Dr. A.L. Slafkosky  
Scientific Advisor  
Commandant of the Marine Corps  
Code AX  
Washington, D.C. 20380

Maritime Administration  
Office of Maritime Technology  
14th and E Streets, NW  
Washington, D.C. 20230

Naval Research Laboratory  
Code 2627 (Documents)  
Washington, D.C. 20375

Library  
Naval Sea Systems Command  
Code 09GS  
Washington, D.C. 20375

## ONR Distribution List

Librarian  
Naval Surface Weapons Center  
White Oak Laboratory  
Silver Spring, Maryland 20910

Library  
Department of Ocean Engineering  
Massachusetts Institute of Technology  
Cambridge, Massachusetts 01778

Library  
Department of Naval Architecture  
and Marine Engineering  
University of Michigan  
Ann Arbor, Michigan 48109

Library  
Applied Research Laboratory  
The Pennsylvania State University  
P.O. Box 30  
State College, Pennsylvania 16801

Library  
Marine Physical Laboratory  
Scripps Institution of Oceanography  
University of California at San Diego  
San Diego, California 92152

Library  
Applied Research Laboratories  
University of Texas at Austin  
Austin, Texas 78712

Library  
Woods Hole Oceanographic Institution  
Woods Hole, Massachusetts 02543

Mr. Dennis Bushnell  
NASA Langley Research Center  
Langley Station  
Hampton, Virginia 23365

Maritime Administration  
Division of Naval Architecture  
14th and E Streets, NW  
Washington, D.C. 20230

Library  
Southwest Research Institute  
8500 Culebra Road  
San Antonio, Texas 78228

Mr. E.N. Comstock  
Code 55W3  
Naval Sea Systems Command  
Washington, D.C. 20362

Dr. W.C. Lin  
Code 152  
David Taylor Research Center  
Bethesda, Maryland 20084

Mr. D.S. Cieslowski  
Code 156  
David Taylor Research Center  
Bethesda, Maryland 20084

Mr. S. Hawkins  
Code 1506  
David Taylor Research Center  
Bethesda, Maryland 20084

Mr. J.H. McCarthy  
Code 154  
David Taylor Research Center  
Bethesda, Maryland 20084

Mr. V.J. Moncella  
Code 1504  
David Taylor Research Center  
Bethesda, Maryland 20084